Stony Brook University

Nuclear matter Equation of State and Brown-Rho scaling

A Dissertation Presented

by

Huan Dong

to

The Graduate School

in Partial Fulfillment of the Requirements

for the Degree of

Doctor of Philosophy

in

Physics

Stony Brook University

May 2012

Stony Brook University

The Graduate School

Huan Dong

We, the dissertation committee for the above candidate for the Doctor of Philosophy degree, hereby recommend acceptance of this dissertation.

Thomas T.S. Kuo – Dissertation Advisor
Professor, Department of Physics and Astronomy

Jacobus Verbaarschot – Chairperson of Defense
Professor, Department of Physics and Astronymy

Dominik A. Schneble – Third Member
Associate Professor, Department of Physics and Astronomy

Roy A. Lacey – Fourth Member
Professor, Department of Chemistry

Yuefan Deng – Outside Member
Professor, Department of Applied Mathematics and Statistics

This dissertation is accepted by the Graduate School.

Charles Taber
Interim Dean of the Graduate School

Abstract of the Dissertation

Nuclear matter Equation of State and Brown-Rho scaling

by

Huan Dong

Doctor of Philosophy

in

Physics

Stony Brook University

2012

Nuclear matter equation of state (EoS) plays an important role in both nuclear physics and astrophysics. The first part of the present dissertation covers a microscopic derivation of a reliable nuclear matter EoS and its applications. To obtain a reliable nuclear matter EoS, we have employed in our derivations either a Brown-Rho (BR) scaled low-momentum nucleon-nucleon (NN) interaction V_{low-k} or a combined interaction given by the sum of an unscaled V_{low-k} and three-body forces. An all-order ring-diagram summation method is used in calculating the EoS so as to include the effect of the ground-state correlations, noting that such correlations are not included if the Hartree-Fock mean field method is employed.

Neutron stars are a nature's unique laboratory for testing nuclear

matter EoS. Their properties such as masses, radii and moments of inertia, can be calculated by solving the Tolman-Oppenheimer-Volkov equations using the nuclear matter EoS. We have tested our EoS in such calculations with and without including the effects from BR scalings. The neutron star masses, radii and moments of inertia given by the BR scaled EoS are in good agreement with empirical values, while those without such scalings are not acceptable.

The ${}^1S_0$ scattering length a_s of the neutron-neutron interaction is -18.97 fm^{-1}, which is quite large. What will happen when a_s goes to infinity, reaching the so called "unitary limit"? We have studied the pure neutron matter's EoS with a family of unitarity potentials all of which are constructed to have infinite ${}^1S_0$ scattering lengths. For such systems, a quantity of much interest is the universal ratio $\xi = E_0/E_0^{free}$ (where E_0 is the true ground-state energy of the system, and E_0^{free} is that for the non-interacting system). For all the unitarity potentials considered, we have numerically obtained $\xi \approx 0.44$ for the cold neutron matter, supporting the existence of such a universality.

The nuclear symmetry energy E_{sym} is an important quantity which can also be derived from the nuclear matter EoS. We have calculated E_{sym} up to densities of $4 \sim 5n_0$ with the effects from the BR and Brown-Rho-Ericson scalings included (n_0 represents the saturation density of symmetric nuclear matter). Our results indicate that E_{sym} is monotonically increasing with the nuclear density. We have compared our results with the constraints on E_{sym} deduced from heavy-ion collision experiments.

The last part of this dissertation describes a new method for the derivation of the shell-model effective NN interactions. We have performed calculations of the *sd* and *sdpf* shell-model effective interactions using the Krenciglowa-Kuo and the recently developed extended Krenciglowa-Kuo iteration methods. We have also stud-

ied the effects of three-body forces on such interactions using a density-dependent two-body interaction derived from the chiral leading-order N^2LO three-body forces.

Contents

List of Figures

List of Tables

Acknowledgements

It is such a pleasure to thank the many people who made this thesis possible.

Foremost, I would like to express my sincere gratitude to my advisor, Professor Thomas T.S. Kuo for his continuous support of my Ph.D. study and research, especially for his patience, motivation and enthusiasm. His hand-on-hand guidance and earnest instructions have helped me greatly. I could not have imagined having a better advisor and mentor for my Ph.D. study.

I would also like to sincerely thank the many people who have taught and guided me in graduate physics studies and in research projects: Prof. Gerald Brown, Prof. Ruprecht Machleidt, Prof. Edward Shuryak, Prof. Jacobus Verbaarschot, Prof. Ismail Zahed, Prof. Dominik Schneble and so on. I also wish to thank my friends Dr. Jeremy Holt, Dr. L.-W. Siu, Dr. Shu Lin, Dr. Ying Xu and so on for all their helps in physics as well as in personal matters during my years at Stony Brook.

Last but not least, I wish to thank my wife Zhu Zhu and my parents for their constant support, understanding, endless patience and encouragement.

Chapter 1

Introduction

1.1 Nuclear matter Equation of State

The nuclear matter is an idealized system composed of interacting neutrons and protons, and its equation of state (EoS) is a longstanding problem in both nuclear physics and astrophysics. The EoS of nuclear matter at high densities plays an essential role in understanding the physical mechanism of supernova formation and evolution, and the structure of neutron stars [1–5]. The possible confrontation of the observational data with the theoretical predictions gives a serious challenge to any theory of EoS. This is surely one of the most fruitful field of research, and we shall investigate the connection between the nuclear matter EoS and neutron star properties. The heavy-ion collision (HIC) experiments at intermediate energy give the possibility of compressing and heating pieces of nuclear matter. After decades of experiments [6–9], extensive data are providing some firm conclusions, or at least constraints, on the EoS up to relatively high densities. The interest in the nuclear matter EoS also appears as a theoretical challenge to the possibility of predicting the properties of nuclear matter in the density range of up to a few times the saturation density n_0 (central density of heavy nuclei). The famous semi-empirical mass formula (Bethe-Weizsäcker formula), obtained by fitting the smooth part of the binding energies of nuclei throughout the nuclear mass table, allows to extract some general properties of the EoS, such as the saturation binding

energy ($E_0/A \simeq -16$MeV). This formula reads

$$E_B = a_V A - a_S A^{2/3} - a_C \frac{Z(Z-1)}{A^{1/3}} - a_A \frac{(A-2Z)^2}{A} + \delta(A,Z), \qquad (1.1)$$

where the coefficients a's are fitted parameters. For instance, a_V is the volume term with value of -16MeV, which is a term of central importance in nuclear matter study. However, the uncertainty of nuclear matter EoS above saturation density is quite large. A reliable nuclear EoS is needed in both theoretical and experimental physics. In this dissertation, we are trying to derive such a reliable EoS microscopically starting from basic nucleon-nucleon (NN) interactions. Applications of the EoS to neutron stars and nuclear symmetry energy will be made.

1.2 Brown-Rho scaling and Three-body forces

In 1935, Hideki Yukawa published his theory of mesons, which explained the interaction between nucleons (protons and neutrons) shortly after the discovery of the neutron by Chadwick. Ever since then, meson-exchange mechanisms have been continuing to serve as the best working model for a quantitative NN potential even in light of Quantum Chromodynamics. There are many highly accurate modern meson-exchange NN potential models, such as CDBonn[10], Nijmegen [11], Argonne V18 [12] and BonnA [13], all of which fit very well to nucleon-nucleon scattering phase shifts and the deuteron binding energy in free space. With these high-precision NN potentials, it is still impossible to reproduce the empirical saturation properties of symmetric nuclear matter ($E_0/A \simeq -16$MeV and $n_0 \simeq 0.16\text{fm}^{-3}$) in many-body theory. Usually, either the saturation density is correct and the binding energy is too weak or the binding energy is correct and the saturation density is too high. In finite nuclei, a well-known similar problem is that one cannot satisfactorily obtain the binding energy of the nucleus and its rms charge radius simultaneously. These inconsistencies suggest that there is something missing in the fundamental NN interactions.

Addressing this shortcoming, a popular approach is to develop a formalism

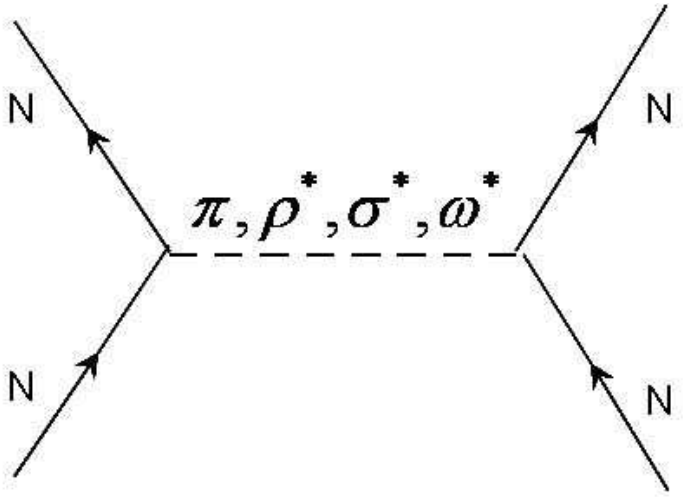

Figure 1.1: One-boson exchange model of V_{NN}.

where the difference between the properties of nucleons and mesons in nuclear medium and those in free space is taken into account. Since hadrons are composed of quarks, one should expect that nucleons, as well as the exchanged mesons, inside a nuclear medium may have very different properties than in free space. In fact, the European Muon Collaboration [14] made the surprising discovery that nucleon structure functions are modified inside of a nucleus. Furthermore, polarization transfer experiments at Jlab [15] have shown that the electromagnetic form factors of a proton are altered in a dense medium compared to free space.

Modifications to meson properties inside a nuclear medium can give rise to density-dependent two-body interactions. The NN interactions we are using are mostly meson-exchange potentials, as illustrated by the one-boson exchange model for V_{NN} of Figure 1.1. If the properties of the exchanged mesons are density dependent, so is V_{NN}. Experimental efforts to determine the properties of hadrons in the nuclear media have been continued for decades. The direct evidence for a dropping ρ-meson mass seems to be provided by the enhanced production of dileptons with invariant mass around $400 - 500$ MeV above known sources of dileptons in the CERES experiment of HIC at CERN SPS [16, 17]. Theoretically, studies of the in-medium hadronic masses is generally based on the notion of chiral symmetry restoration in dense matter. There

are a number of models that connect the order parameter for chiral symmetry restoration with dynamical mass generation, such as the Nambu-Jona-Lasinio model[18], Gell-Mann-Oakes-Renner model [19] and so on. At the beginning of 1990's, Gerald Brown and Manque Rho [20] suggested the scaling

$$\sqrt{\frac{g_A}{g_A^*}}\frac{m_N^*}{m_N} = \frac{m_\sigma^*}{m_\sigma} = \frac{m_\rho^*}{m_\rho} = \frac{m_\omega^*}{m_\omega} = \frac{f_\pi^*}{f_\pi} = \Phi(n), \tag{1.2}$$

where g_A is the axial coupling constant, Φ is a function of the nuclear density n, and the star indicates in-medium values of the corresponding quantities. In this dissertation, we shall mainly apply the above scaling rule to the light vector mesons (ρ and ω) and scalar meson (σ), and investigate their effects on NN interaction in medium.

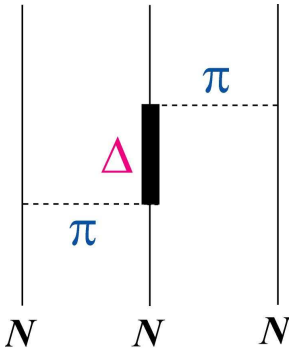

Figure 1.2: Feynman diagram associated with Fujita-Miyazawa three-body forces due to the two-pion-exchange among three nucleons.

An alternative approach for including the effect of the nuclear medium is by way of the three-body forces. In fact, as early as 1939 [21] the three-body forces was introduced in nuclear structure calculations. In 1957 Fujita and Miyazawa [22] proposed the three-nucleon forces model based on a two-pion exchange mechanism, as shown in Figure 1.2, which is the beginning of quantitative studies of three-body forces. Since then a lot of efforts have been made theoretically as well as experimentally to establish the three-nucleon forces. Three-body forces have been a key element to explain phenomena such as the properties of light nuclei (A $<$ 12). Recently, the inclusion of the three-body forces [23] gives satisfactory results for the binding energy and

rms charge radius for nuclei with A = 10 − 13. Also three-body forces are successfully applied in dense nuclear matter [24–29]. There is also progress on the origin of three-body forces. In the past, the three-body forces were mostly included empirically, but now it is possible to derive the three-body forces from the chiral effective theory [30]. In this dissertation, we shall study the effects of the Brown-Rho (BR) scaling, the empirical Skyrme three-body forces and the chiral leading-order N^2LO three-body forces in nuclear matter and finite nuclei.

1.3 Low-momentum interaction V_{low-k}

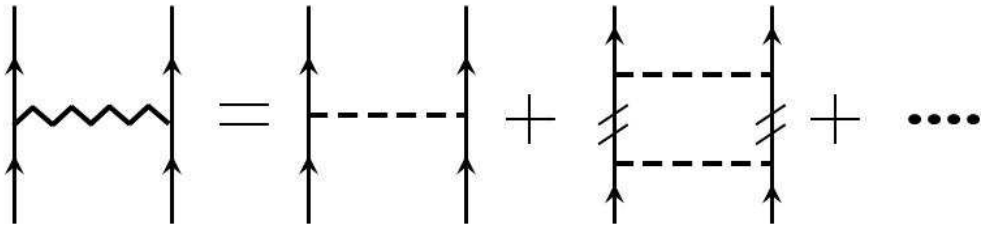

Figure 1.3: Diagrammatic representation of the G-matrix effective interaction. Double hashed lines represent Pauli-blocked intermediate states.

In all of our following calculations, we shall employ a nuclear EoS derived microscopically from realistic NN potentials V_{NN}. Such microscopic calculations would provide a test if it is possible to predict outcomes of experiments starting from an underlying NN interaction. As we know, the strong short-range repulsion contained in V_{NN} usually requires a special renormalization treatment before using this interaction in many-body calculations. A familiar such treatment is the Brueckner-Hartree-Fock (BHF) G-matrix method. For many years, the BHF[13, 31–34] and the DBHF methods [35] (DBHF is a relativistic generalization of BHF) were the primary framework for nuclear matter calculations. In both BHF and DBHF the G-matrix interaction is obtained by summing the particle-particle ladder diagrams to all orders, as shown in Figure 1.3. This G-matrix interaction is energy dependent, and this energy dependence adds complications to calculations. In the past several years, there has

been much progress in the renormalization group (RG) approach for the NN interaction. A central idea here is that to describe the low-energy properties of a physical system it should be adequate to employ only a low-momentum effective interaction confined within a momentum decimation scale Λ. It is generally believed that the low-energy properties of physical systems can be satisfactorily described by an effective theory confined within a low-energy (or low-momentum) model space [36]. In addition, the high-momentum (short range) parts of various V_{NN} models are model dependent and rather uncertain. In this section, we shall describe the newly developed methods for deriving an energy independent effective low-momentum interaction V_{low-k} by way of a RG procedure, the details of which have been described in [36–42]. Here we shall just briefly outline its main steps.

Motivated by the above considerations, the following low-momentum renormalization (or model-space) approach has been introduced [36]. Namely one employs a low-momentum model space where all particles have momentum less than a decimation scale Λ. The corresponding renormalized effective NN interaction is V_{low-k}, obtained by integrating out the $k > \Lambda$ momentum components of V_{NN}. This "integrating-out" procedure is carried out by way of a T-matrix equivalence approach. We start from the full-space T-matrix equation

$$T(p', p, p^2) \quad = \quad V_{NN}(p', p) \quad + \quad \mathcal{P} \int_0^\infty q^2 dq \frac{V_{NN}(p', q) T(q, p, p^2)}{p^2 - q^2}, \quad (1.3)$$

where $\mathcal{P}$ denotes the principal-value integration. Notice that in the above equation the intermediate state momentum q is integrated from 0 to ∞ covering the whole space. We then define an effective low-momentum T-matrix by

$$T_{low-k}(p', p, p^2) = V_{low-k}(p', p) + \mathcal{P} \int_0^\Lambda q^2 dq \frac{V_{low-k}(p', q) T_{low-k}(q, p, p^2)}{p^2 - q^2}, \quad (1.4)$$

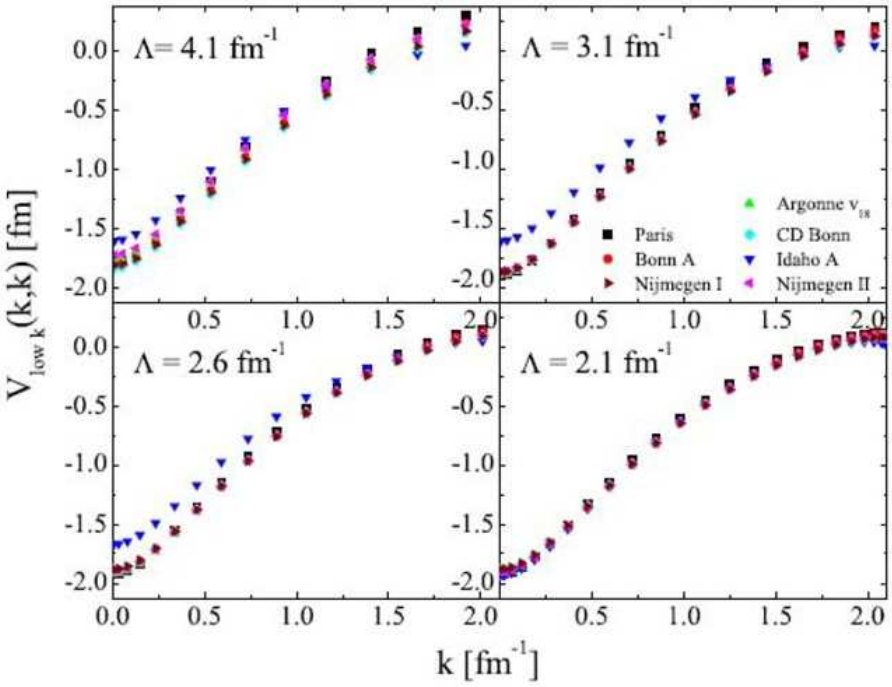

Figure 1.4: Diagonal matrix elements of V_{low-k} for different high-precision modern potentials in the $^1S_0$ partial wave with various cutoffs Λ.

where the intermediate state momentum is integrated from 0 to Λ, the momentum space cutoff. The low momentum interaction V_{low-k} is then obtained from the above equations by requiring the T-matrix equivalence condition

$$T(p', p, p^2) = T_{low-k}(p', p, p^2); \ (p', p) \leq \Lambda. \tag{1.5}$$

Note that T and T_{low-k} are both half on energy shell, and they are equivalent within Λ. The low-energy ($< \Lambda^2$) phase shifts of V_{NN} are preserved by V_{low-k} and so is the deuteron binding energy. As we shall discuss later, the scattering length a_s of V_{NN} is also preserved.

There are several advantages to use the V_{low-k} as the effective NN interaction in nuclear matter calculations, one of which is the uniqueness of V_{low-k}. It is well known that the absence of a unique NN interaction has bothered nuclear physicists for a long time. Under the above RG procedure, all of the high precision V_{NN}'s flow, as $\Lambda \to 2.1\text{fm}^{-1}$, to a nearly unique interaction V_{low-k},

as illustrated in Figure 1.4. The resulting V_{low-k} is well-behaved at short distances and moreover it is energy-independent (in contrast to G-matrix). It is convenient to apply V_{low-k} in both nuclear matter and finite nuclei calculations.

High-precision NN potentials [10–13] are fitted to NN scattering data up to laboratory energy $E_{lab} \approx 350$MeV, which corresponds to our decimation scale of $\Lambda \approx 2.1\text{fm}^{-1}$. Thus we can view the construction of low-momentum interactions as integrating out the experimentally unconstrained (or model-dependent) components of the NN interaction, which is shown in Figure 1.4.

1.4 Ring-diagram Summation

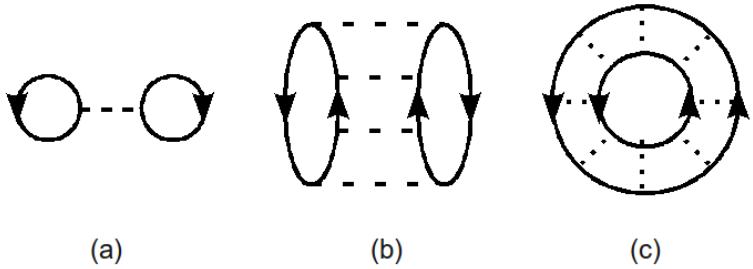

Figure 1.5: Diagrams included in the all-order *pphh* ring-diagram summation for the ground state energy shift of nuclear matter. Each dashed line represents a V_{low-k} vertex.

In physics and chemistry, the Hartree-Fock (HF) method is widely used for the determination of the ground-state energy of a quantum many-body system. According to the linked-diagram expansion, the HF method includes only the lowest-order diagram (a) in Figure 1.5. In this dissertation, we are going beyond HF and shall include the ring diagrams of the type shown in Figure 1.5 to all orders. There (a), (b) and (c) are respectively 1st-, 4th- and 8th-order such diagrams. In this so called all-order *pphh* ring-diagram summation [43, 44], the ground-state energy shift ΔE_0 (defined as $E_0 - E_0^{free}$, where the E_0 is the true ground state energy and E_0^{free} is that for non-interacting system)

is given by [44]

$$\Delta E_0(n,\alpha) \quad = \quad \int_0^1 d\lambda \sum_m \sum_{ijkl<\Lambda} Y_m(ij,\lambda) \ \times \ Y_m^*(kl,\lambda)\langle ij|V_{low-k}|kl\rangle, \quad (1.6)$$

where the amplitudes Y represent the overlap matrix elements

$$Y_m^*(kl,\lambda) = \langle \Psi_m(\lambda, A-2)|a_l a_k|\Psi_0(\lambda, A)\rangle. \quad (1.7)$$

$\Psi_0(\lambda, A)$ denotes the true ground state of nuclear matter which has A particles while $\Psi_m(\lambda, A-2)$ the mth true eigenstate of the (A-2) system. If there is no ground-state correlations (i.e. Ψ_0 is a closed Fermi sea), we have $Y_m^*(kl,\lambda) = f_k f_l$ and Equation (1.6) reduces to the HF result. The Y amplitudes are obtained by solving the Random Phase Approximation (RPA) equations

$$\begin{aligned} BX + CY &= \omega X \\ B^*Y + C^*X &= -\omega Y, \end{aligned} \quad (1.8)$$

where X is Y's RPA partner [45]. ω is the excitation energy corresponding to either $(E_m(A-2) - E_0(A))$ or $(E_m(A+2) - E_0(A))$. B and C matrices are calculated from V_{low-k} as indicated by Equation (1.9). It is readily recognized that the above RPA equation is of the same form as the well-known quasi-boson RPA equations [46], resulting from treating the many-body system approximately as a collection of quasi bosons (each composed of a pair of interacting fermions). Thus our all-order ring-diagram calculation is in fact a quasi-boson approximation for nuclear matter, treating it as a system of quasi bosons.

In our nuclear matter calculations, we use the V_{low-k} interaction and the RPA reads

$$\sum_{kl}[(\epsilon_i + \epsilon_j)\delta_{ij,kl} + \lambda(\bar{f}_i\bar{f}_j - f_i f_j)\langle ij|V_{low-k}|kl\rangle] \times Y_n(kl,\lambda) = \omega_n Y_n(ij,\lambda); \quad (i,j,k,l) \leq \Lambda. \quad (1.9)$$

In the above, the single particle (s.p.) indices $(i, j, ...k, l)$ denote both protons and neutrons. The s.p. energies ϵ are the HF energies given by

$$\epsilon_k = \hbar^2 k^2/2m + \sum_{h<k_F(h)} \langle kh|V_{low-k}|kh\rangle, \tag{1.10}$$

where $k_F(h) = k_{Fn}$ if h is neutron and $= k_{Fp}$ if it is proton. The occupation factors f_i and f_j of Equation (1.9) are given by $f_a = 1$ for $k \leq k_F(a)$ and $f_a = 0$ for $k > k_F(a)$; also $\bar{f}_a = (1 - f_a)$. Again $k_F(a) = k_{Fn}$ if a is a neutron and $= k_{Fp}$ if it is a proton. Note that the normalization condition for Y_n in Equation (1.9) is $\langle Y_n|\frac{1}{Q}|Y_n\rangle = -1$ and $Q(\boldsymbol{k}_i, \boldsymbol{k}_j) = (\bar{f}_i\bar{f}_j - f_i f_j)$ [47]. In addition, $\sum_m$ in Equation (1.6) means we sum over only those solutions of the RPA (Equation (1.9)) which are dominated by hole-hole components as indicated by the normalization condition. Note that there is a strength parameter λ in the above, and it is integrated from 0 to 1. Clearly our EoS includes effect of ground-state correlations generated by the all-order sum of *pphh* ring diagrams.

1.5 Dissertation Outline

In the present dissertation, we mainly focus on the derivation of a reliable nuclear matter EoS up to high density region ($4 \sim 5n_0$). Since the neutron star is the only dense nuclear matter system in nature, we shall test our EoS on neutron stars in Chapter 2. We first present our EoS calculations for symmetric nuclear matter. Then we shall present the importance of BR scaling and/or three-body forces in high density nuclear matter. Finally, we apply the derived EoS to neutron stars, calculating the neutron star's properties, such as their masses and radii. To be reported later, the maximum mass of neutron stars obtained is $1.2M_\odot$ (where $M_\odot$ is the solar mass) without BR scaling or three-body forces, and it increases to $1.8M_\odot$ by including BR scaling or three-body forces, which is close to the new two-solar-mass [48] neutron star observation $(1.97 \pm 0.04M_\odot)$.

In Chapter 3, we shall study the ground state properties of cold neutron

matter at the unitary limit, where the $^1S_0$ scattering length approaches infinity. The unitary limit has been realized for trapped cold alkali-atom experiments [49, 50], while it has not been experimentally realized for neutron matter. In this chapter, we applied a family of unitary hard-core square-well potentials as the NN interactions and studied the ground energy of neutron matter. The so called universal ratio ξ obtained is close to 0.44, in agreement with the best accepted values [51–56].

The nuclear symmetry energy is closely related to the nuclear matter EoS, and plays an important role in nuclear physics. In Chapter 4, we shall study the density dependence of nuclear symmetry energy. Both the linear BR scaling and nonlinear Brown-Rho-Ericson scaling to the light mesons have been employed in our calculations. Calculations of the nuclear symmetry energy have also been carried out with three-body forces. We have found that the nuclear symmetry energy is monotonically increasing with nuclear density up to several times the saturation density n_0, consistent with the empirical formulae [8, 9] deduced from HIC experiments.

In Chapter 5, we report a new method for the derivation of the shell-model effective interactions for both degenerate and non-degenerate model spaces using the Krenciglowa-Kuo (KK) and the recently developed extended KK iteration (EKKO) [57] methods. The starting point is the low-momentum NN interaction V_{low-k} obtained from the N^{3}LO chiral NN interaction. The model spaces spanned by the *sd* and *sdpf* shells are both considered, and applied to mass A = 18 nuclei. The new vertex function $\hat{Z}$-box of EKKO is compared with the $\hat{Q}$-box of KK. For certain choices of the model-space partitions, the $\hat{Q}$-box of the KK method may have singularity difficulties. As we shall discuss later, such difficulties are avoided in the EKKO method. In the second part, the chiral leading-order N^{2}LO three-body forces are included in the derivation of the shell-model effective interaction and the results are discussed.

Parts of the results of this dissertation have been published [58–60], and a summary is contained in Chapter 6.

Chapter 2

Nuclear matter Equation of State and Neutron Stars

2.1 Introduction

Neutron stars are very interesting physical systems and their properties, such as masses and radii, can be derived from the equation of state (EoS) of the nuclear medium contained in them. In carrying out such derivation, there is, however, a well-known difficulty, namely that the EoS is not fully known. Determination of the EoS for neutron stars is an important yet challenging undertaking. As reviewed in [1–5], this topic has been extensively studied and much progress has been made. Generally speaking, there are two complementary approaches to determine the EoS. One is to deduce it from HIC experiments, and crucial information about the EoS has already been obtained [5–9]. Another approach is to calculate the EoS microscopically from a many-body theory. (See, e.g. [61, 62] and references quoted therein.) As is well-known, there are a number of difficulties in this approach. Before discussing them, let us first briefly outline the derivation of neutron-star properties from its EoS.

One starts from the Tolman-Oppenheimer-Volkov (TOV) equations

$$\begin{aligned} \frac{dp(r)}{dr} &= -\frac{GM(r)\epsilon(r)}{c^2 r^2}\frac{[1+\frac{p(r)}{\epsilon(r)}][1+\frac{4\pi r^3 p(r)}{M(r)c^2}]}{[1-\frac{2GM(r)}{rc^2}]}, \\ \frac{dM(r)}{dr} &= 4\pi r^2 \epsilon(r). \end{aligned} \tag{2.1}$$

where $p(r)$ is the pressure at radius r and $M(r)$ is the gravitational mass inside r. G is the gravitational constant and $\epsilon(r)$ is the energy density inclusive of the rest mass density. The solutions of these equations are obtained by integrating them out from the neutron-star center till its edge where p is zero. (Excellent pedagogical reviews on neutron stars and TOV equations can be found in [63].) In solving the above equations, an indispensable ingredient is clearly the nuclear matter EoS for the energy density $\epsilon(n)$, n being the medium density. As the density at the neutron star center is typically very high (several times higher than normal nuclear saturation density of $n_0 \simeq 0.16\text{fm}^{-3}$), we need to have the above EoS over a wide range of densities, from very low to very high.

In this chapter we shall calculate the nuclear EoS directly from a fundamental NN interaction V_{NN} and then use it to calculate neutron star properties by way of the TOV equations. There have been neutron-star calculations using a number of EoS's, most of which empirically determined, and the mass-radius trajectories given by them are widely different from each other (see, e.g. Fig. 2 of [5]). To determine the EoS with less uncertainty would certainly be desirable. There are a number of different NN potential models [10–13], all of which possess strong short-range repulsions and to use them in many-body calculations one needs first take care of their short-range correlations by way of some renormalization methods. We shall use the recently developed RG method, as discussed in section 1.3, to convert V_{NN} into an effective low-momentum NN interaction V_{low-k} [36–42]. This V_{low-k} will then be used to calculate the nuclear matter EoS using the low-momentum ring-diagram approach discussed in section 1.4, where the *pphh* ring diagrams of the EoS are summed to all orders.

We shall also study the effects of BR scaling [20, 64–66] on neutron star properties. As discussed in [44], low-momentum ring diagram calculations us-

ing two-body NN interactions alone are not able to reproduce the empirical properties for symmetric nuclear matter; the calculated energy per particle (E_0/A) and saturation density (n_0) are both too high compared with the empirical values of $E_0/A \simeq -16$MeV and $n_0 \simeq 0.16\text{fm}^{-3}$. As discussed in section 1.2, the main idea of the BR scaling is that the masses of in-medium mesons are generally suppressed, because of their interactions with the background medium, compared with their masses in free space. As a result, the NN interaction in the nuclear medium can be significantly different from that in free space, particularly at high density. Effects from such medium modifications have been found to be very helpful in reproducing the empirical properties of symmetric nuclear matter [44]. Dirac-Brueckner-Hartree-Fock (DBHF) nuclear matter calculations have been conducted with and without BR scaling [67–69]. In addition, BR scaling has played an essential role in explaining the extremely long life time of ^{14}C β-decay [70]. As mentioned earlier, the central density of neutron stars is typically rather high, $\sim 5n_0$ or higher. At such high density, the effect of BR scaling should be especially significant. Neutron stars may provide an important test for BR scaling.

2.2 In-medium NN interactions based on Brown-Rho scaling

As discussed in Chapter 1, we shall use the low-momentum ring-diagram scheme to calculate the nuclear matter EoS with BR scaling. We considered asymmetric nuclear matter of total density n and asymmetric parameter α defined as

$$n = n_n + n_p; \quad \alpha = \frac{n_n - n_p}{n_n + n_p}, \tag{2.2}$$

where n_n and n_p denote respectively the neutron and proton density and they are related to the respective Fermi momenta by $k_{Fn}^3/(3\pi^2)$ and $k_{Fp}^3/(3\pi^2)$. The proton fraction is $\chi = (1-\alpha)/2$.

A main purpose of this chapter is to study whether neutron star proper-

ties can be satisfactorily described by EoS microscopically derived from NN interactions. Before proceeding, it is important to first check if such EoS can satisfactorily describe the saturation properties of symmetric nuclear matter. As discussed in [44], many-body calculations for symmetric nuclear matter using two-body NN interactions alone are generally not capable of reproducing empirical nuclear matter saturation properties. To remedy this shortcoming one needs to consider NN interactions with in-medium modifications or three-body forces.

A central result of the BR scaling is that the masses of mesons in the nuclear medium are suppressed (dropped) compared to those in free space [20, 64–66]. NN interactions are mediated by mesons, and clearly in-medium modifications of meson masses can significantly alter the NN interactions. These modifications could arise from the partial restoration of chiral symmetry at finite density/temperature or from traditional many-body effects. Particularly important are the light mesons, for which there is now evidence from both theory [72–74] and experiments [75, 76] that the masses may decrease by approximately $10-15\%$ at normal nuclear matter density and zero temperature. For low densities ($n \lesssim n_0$), a linear approximation for the in-medium mass decrease has been suggested [72], namely

$$\frac{m^*}{m} = 1 - C\frac{n}{n_0}. \tag{2.3}$$

where m^* is the in-medium meson mass, n is the local nuclear matter density and n_0 the nuclear matter saturation density. C is a constant of value $0.10 \sim 0.15$. The above scaling is commonly referred to as the BR scaling, and it has been found to be very important for nuclear matter saturation properties in the ring-diagram calculation of symmetric nuclear matter [44].

It is of interest that the effect of BR scaling in nuclear matter can be well represented by an empirical Skyrme three-body force [44]. The Skyrme force has been a widely used effective interaction in nuclear physics and it has been very successful in describing the properties of both finite nuclei and nuclear

matter[77]. It has both two-body and three-body terms, namely

$$V_{Skyrme} = \sum_{i<j} V(i,j) + \sum_{i<j<k} V_{3b}(i,j,k). \tag{2.4}$$

Here $V(i,j)$ is a momentum dependent zero-range interaction. Its three-body term is a zero-range interaction

$$V_{3b}(i,j,k) = t_3 \delta(\boldsymbol{r}_i - \boldsymbol{r}_j)\delta(\boldsymbol{r}_j - \boldsymbol{r}_k), \tag{2.5}$$

which is usually expressed as a density-dependent two-body interaction of the form

$$V_n(1,2) = \frac{1}{6}(1 + x_3 P_\sigma) t_3 \delta(\boldsymbol{r}_1 - \boldsymbol{r}_2) n(\boldsymbol{r}_{av}). \tag{2.6}$$

where P_σ is the spin-exchange operator and $\boldsymbol{r}_{av} = \frac{1}{2}(\boldsymbol{r}_1 + \boldsymbol{r}_2)$. t_3 and x_3 are parameters determined by fitting certain experimental data. The general structure of V_{Skyrme} is rather similar to the effective interactions based on effective field theories (EFT) [71], with $V(i,j)$ corresponding to V_{low-k} and $V(i,j,k)$ to the EFT three-body forces. The Skyrme three-body forces, however, are much simpler than that in EFT.

2.3 Symmetric Nuclear Matter

When an EoS is used to calculate neutron-star properties, it is important and perhaps necessary to first test if the EoS can satisfactorily describe the properties of symmetric nuclear matter such as its saturation energy E_0/A and density n_0. In principle, only those EoS's which have done well in this test are suitable for being used in neutron star calculation. In this section, we shall calculate properties of symmetric nuclear matter using the low-momentum ring-diagram EoS which we will use in our neutron star calculations, to test if it can meet the above requirements. As described above, we first calculate the V_{low-k} interaction for a chosen decimation scale Λ. Then we calculate the ground state energy per particle E_0/A with the *pphh* ring diagrams summed to all orders.

In the above calculation, the choice of Λ plays an important role. As discussed in [44], the tensor force is important for nuclear saturation and therefore one should use a sufficiently large Λ so that the tensor force is not integrated out during the derivation of V_{low-k}. Since the main momentum components of the tensor force has $k \sim 2\text{fm}^{-1}$, one needs to use $\Lambda \sim 3\text{fm}^{-1}$ or larger. There is another consideration concerning the choice of Λ. The density of the neutron star interior is very high, several times larger than n_0. To accommodate such high density, it is necessary to use sufficiently large Λ, suggesting a choice of Λ larger than $\sim 3\text{fm}^{-1}$. As discussed in section 1.3, a nice feature of V_{low-k} is its near uniqueness. The V_{low-k}'s derived from various different realistic NN potentials are practically identical to each other for $\Lambda \lesssim 2.1\text{fm}^{-1}$, while for larger Λ's the resulting V_{low-k}'s begin to have noticeable differences but are still similar to each other for Λ up to about 3.5fm^{-1}. This and the above considerations have led us to choose Λ between 3.0 and 3.5fm^{-1} for our present study. The dependence of our results on the choice on Λ will be discussed later on.

We have carried out V_{low-k} ring-diagram calculations for symmetric nuclear matter using several NN potentials (CDBonn [10], Nijmegen [11], Argonne V18 [12] and BonnA [13]) with several values of Λ ranging from 3.0 to 3.5fm^{-1}. In Figure 2.1 we present some representative results using CDBonn and BonnA potentials, the results for other potentials and Λ's being very similar. As shown, the results for small densities are nearly independent of Λ within the range considered. But for larger densities, the results have significant variations with Λ and potentials, this being possibly a reflection of the different short-range repulsions contained in the potential models. A common feature of our results is, as displayed in the figure, that the calculated E_0/A and saturation Fermi momentum k_F^0 are both too high compared with the empirical values ($E_0 \simeq -16\text{MeV}$ and $k_F^0 \simeq 1.33\text{fm}^{-1}$ or $n_0 \simeq 0.16\text{fm}^{-3}$).

As discussed in section 2.2, the above situation can be largely improved by way of using a V_{NN} with the BR scaling. In [67], DBHF calculations for symmetric matter with a BR-scaled BonnB NN potential have been carried out, and their results are in good agreement with the empirical values, largely improved over those from the unscaled potential. In [44], ring-diagram

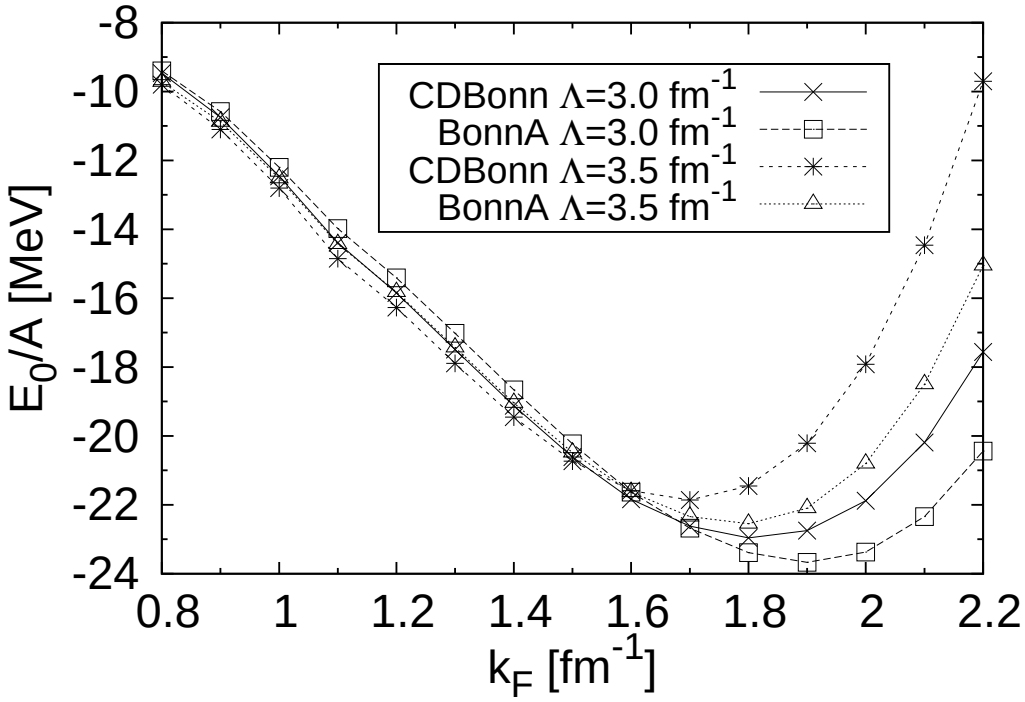

Figure 2.1: Ring-diagram EoSs for symmetric nuclear matter with V_{low-k}s derived from CDBonn and BonnA potentials. Different decimation decimation Λ (3.0 and 3.5fm^{-1}) are used.

EoS calculations for symmetric nuclear matter have been performed using the Nijmegen potential with and without BR scaling, the former giving highly improved results for nuclear matter saturation. It should be useful if the above effect on nuclear saturation from BR scaling also holds for other NN potentials. To study this, we use a different potential, the BonnA potential [13], for investigating the effect of BR scaling on ring-diagram calculations for symmetric nuclear matter. In Figure 2.2, results of such ring-diagram calculations for symmetric nuclear matter with and without BR scaling are presented. For the scaled calculation, the mesons (ρ, ω, σ) of the BonnA potential are slightly scaled according to Equation (2.3) with the choice of $C_\rho = 0.113$, $C_\omega = 0.128$ and $C_\sigma = 0.102$. These values are chosen so that the calculated E_0/A and k_F^0 are in satisfactory agreement with the empirical values. The EoS given by the above BR-scaled potential is shown by the top curve of Figure 2.2 (la-

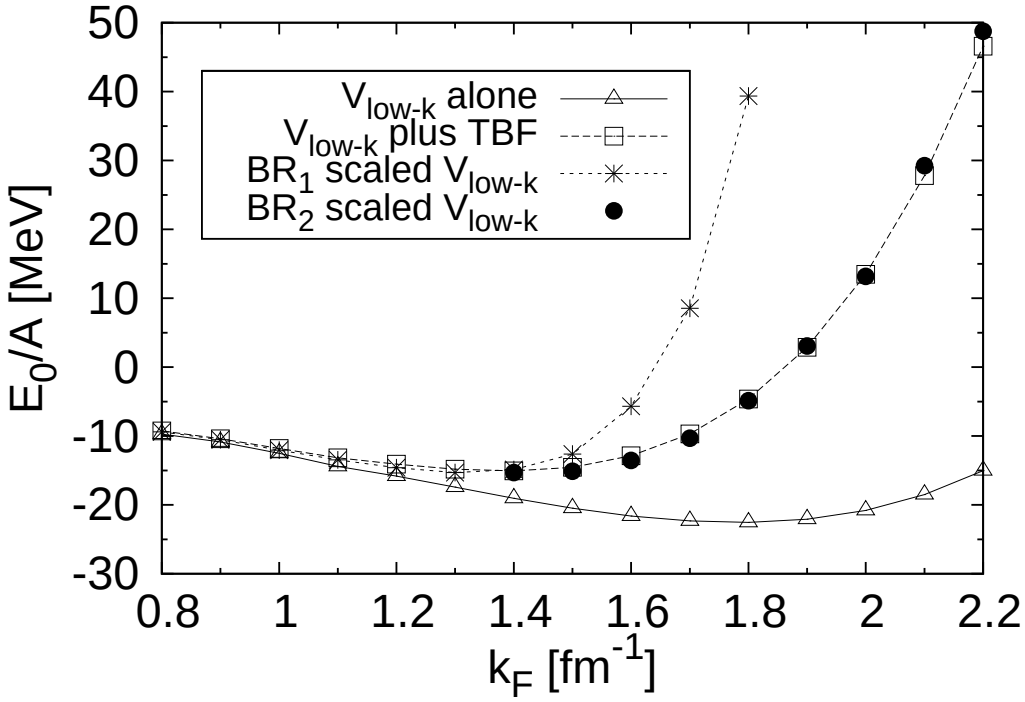

Figure 2.2: Ring-diagram EoSs for symmetric nuclear matter given by V_{low-k} alone, V_{low-k} with linear (BR_1) and nonlinear (BR_2) scalings, and V_{low-k} plus the three-body force (TBF) V_{3b} of Equation (2.5). Λ=3.5fm^{-1} used for all cases. See text for other explanations.

belled as 'BR_1'), and it has $E_0/A \simeq -15.3$MeV and $k_F^0 \simeq 1.33$fm^{-1}, in good agreement with the empirical values. In addition, it has compression modulus $\kappa \simeq 225$MeV. The result using V_{low-k} alone is also shown in Figure 2.2 (bottom curve). Clearly BR scaling is also important and helpful for the BonnA potential in reproducing empirical nuclear matter saturation properties.

We shall now discuss if the above effect of BR scaling can be simulated by an empirical three-body force of the Skyrme type. It is generally agreed that the use of two-body force alone cannot satisfactorily describe nuclear saturation, and that certain three-body forces are needed to ensure nuclear saturation [71]. There are basic similarities between three-body forces and BR scaling. To see this, let us consider a meson exchanged between two interacting forces. When this meson interacts with a third spectator nucleon,

this process contributes to BR scaling or equivalently it generates the three-body interaction. In [44], it was already found the ring-diagram results of BR-scaled V_{low-k} derived from the Nijmegen potential can be well reproduced by the same calculation except for the use of the interaction given by the sum of the V_{low-k} plus the empirical three-body force V_{3b} of Equation (2.5). (Note that V_{3b} is calculated using Equation (2.6) with n being the local nuclear matter density.) Here we repeat this calculation using a different potential, namely the BonnA potential. The strength parameter t_3 is adjusted so that the low-density ($\lesssim n_0$) EoS given by the (V_{low-k}+V_{3b}) calculation is in good agreement with that from the BR-scaled V_{low-k}. (We fix the parameter x_3 of Equation (2.6) as zero, corresponding to treating the ${}^1S_0$ and ${}^3S_1$ channels on the same footing.) Results for such a calculation, with t_3 chosen as 2000 MeV $\cdot$ fm^6 are presented as the middle curve of Figure 2.2 (labelled as 'V_{low-k} plus TBF'). As shown, for $k_F \lesssim 1.4\text{fm}^{-1}$ they agree very well with the results from the BR-scaled V_{low-k}. The above (V_{low-k}+V_{3b}) calculation gives $E_0/A \simeq -14.7$MeV and $k_F^0 \simeq 1.40\text{fm}^{-1}$ in satisfactory agreement with the BR-scaled results given earlier, while its compression modulus is κ=140 MeV.

It should be noticed, however, that for $k_F \gtrsim 1.4\text{fm}^{-1}$ the curve for 'BR_1 scaled V_{low-k}' rises much more rapidly (more repulsive) than the 'V_{low-k} plus TBF' one. The compression modulus given by them is also quite different, 225 versus 140 MeV. These differences may be related to the linear BR scaling adopted in Equation (2.3). This scaling is to be used for density less than n_0. For density significantly larger than n_0, such as in the interior of neutron star, this linear scaling is clearly not suitable.

To our knowledge, how to scale the mesons at high densities is still an open question [20, 64–66, 72]. In the present work, we have considered two schemes for extending the BR scaling to higher densities: One is the above Skyrme-type extrapolation; the other is an empirical modification where in the high density region a nonlinear scaling is assumed, namely $m^*/m = (1-C(n/n_0)^B)$ with B chosen empirically. The exponent B is 1 in the linear BR scaling of Equation (2.3). As seen in Figure 2.2, the linear BR-scaled EoS agrees well with the 'V_{low-k} plus TBF' EoS only in the low-density ($\lesssim n_0$) region, but not for densities beyond. Can a different choice of B give better agreement for the

high-density region? As seen in Figure 2.2, to obtain such better agreements we need to use a scaling with weaker density dependence than BR_1. Thus we have considered $B < 1$, and have found that the EoSs with B near 1/3 has much improved agreements with the Skyrme EoS in the high density region. To illustrate this, we have repeated the 'BR_1' EoS of Figure 2.2 with only one change, namely changing B from 1 to 0.3. (The scaling parameters C's are not changed, for convenience of comparison.) The new results, labeled as 'BR_2', are also presented in Figure 2.2. As seen, 'BR_2' and 'V_{low-k} plus TBF' are nearly identical in a wide range of densities beyond n_0. This is an interesting result, indicating that below n_0 the 'V_{low-k} plus TBF' EoS corresponds to the linear BR_1 scaled EoS while beyond n_0 the nonlinear BR_2 one. The BR_1 and BR_2 EoS's have a small discontinuity (in slope) at n_0, and the above EoS with three-body forces is practically a continuous EoS with good fitting to both. As we shall discuss later, the above three-body force is also important and desirable for neutron-star calculations involving much higher densities. Possible microscopic connections between the Skyrme three-body force and BR scalings need further studies.

The ring-diagram nuclear matter EoS's using the 'V_{low-k} plus TBF' interaction are in fact rather insensitive to the choice of Λ. As discussed earlier, a suitable range for Λ is from 3.0 to 3.5fm^{-1}. So in carrying out the above calculations, one first chooses a Λ within the above range. Then t_3 is determined by the requirement that the low-density ($\lesssim n_0$) ring-diagram EoS given by BR_1-scaled V_{low-k} is reproduced by that from (V_{low-k}+V_{3b}). In Figure 2.3 we present some sample results for $\Lambda = 3.0$ and 3.5 fm^{-1} with CDBonn and BonnA potentials, all using $t_3 = 2000\text{MeV} \cdot \text{fm}^6$. Note that this t_3 value is for Λ=3.5 fm^{-1} and BonnA potential; for convenience in comparison it is here used also for the other three cases. It is encouraging to see that within the above Λ range our results are remarkably stable with regard to the choice of both Λ and t_3. The four curves of Figure 2.3 are nearly overlapping, and their $(E_0/A, k_F^0, \kappa)$ values are all close to (-15 MeV, 1.40fm^{-1}, 150 MeV). We have repeated the above calculations for the Nijmegen and Argonne V18 potentials, and have obtained highly similar results. As we shall discuss in the next section, the inclusion of V_{3b} is also important in giving a satisfactory neutron-

matter ring-diagram EoS. Calculations of neutron star properties using the above ($V_{low-k} + V_{3b}$) interaction will also be presented there. Unless otherwise specified, we shall use from now on Λ=3.5 fm^{-1} for the decimation scale and $t_3 = 2000\text{MeV} \cdot \text{fm}^6$ for the three-body force V_{3b}.

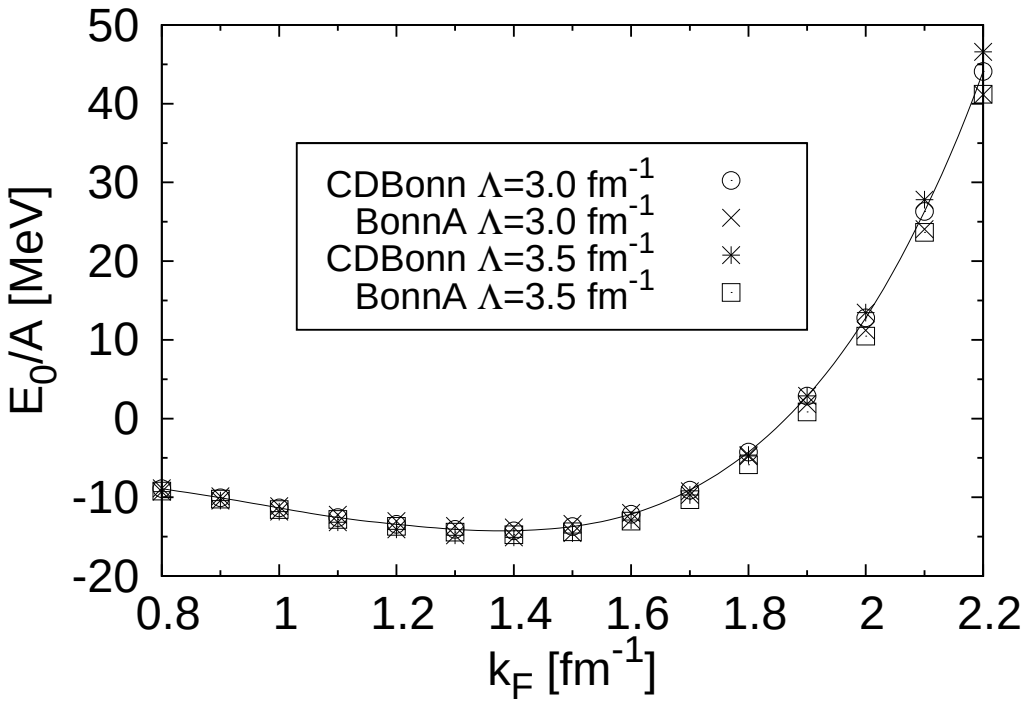

Figure 2.3: Ring-diagram EoS for symmetric nuclear matter with the interaction being the sum of V_{low-k} and the three-body force (TBF) of Equation (2.5). Four sets of results are shown for CDBonn and BonnA potentials with Λ=3.0 and 3.5 fm^{-1}. A common three-body force of $t_3 = 2000\text{MeV} \cdot \text{fm}^6$ is employed.

2.4 Neutron stars

2.4.1 Neutron star with neutrons only

As a preliminary test of our ring-diagram EoS, in this subsection we shall consider neutron stars as composed of pure neutron matter only. This simplified structure is convenient for us to describe our methods of calculation. In

addition, this also enables us to check how well the properties of neutron stars can be described under the pure-neutron matter assumption. Realistic neutron stars have of course more complicated compositions; they have nuclei crusts and their interior is composed of neutrons as well as other elementary particles [5, 61]. We shall study the effects of using β-stable and nuclei-crust EoS's in our neutron star calculations in the next subsection. In this subsection we consider neutron stars at zero temperature.

Using the methods outlined before, we first calculate the ground-state energy per particle E_0/A for neutron matter. Then the energy density ε, inclusive of the rest-mass energy, is obtained as

$$\varepsilon(n) = n(\frac{E_0}{A} + m_n c^2), \tag{2.7}$$

where c is the speed of light and m_n the nucleon mass. By differentiating E_0/A with density, we obtain the pressure-density relation

$$p(n) = n^2 \frac{d(E_0/A)}{dn}. \tag{2.8}$$

From the above two results, the $\varepsilon(p)$ EoS is obtained. It is the $\varepsilon(p)$ EoS which is used in the solution of the TOV equations.

To accommodate the high densities in the interior of neutron stars, we have chosen Λ=3.5 fm^{-1} for our present neutron star calculation. Our ring-diagram EoS for neutron matter is then calculated using the interaction (V_{low-k} $+V_{3b}$) with the parameter $t_3 = 2000\text{MeV} \cdot \text{fm}^6$. Note that this value was determined for symmetric nuclear matter, as discussed in section 2.3. Is this t_3 also appropriate for the neutron matter EoS? We shall address this question here. In Figure 2.4 we present results from the above neutron matter EoS calculations for four interactions (CDBonn, Nijmegen, Argonne V18, BonnA). It is seen that the EoSs given by them are quite close to each other, giving a nearly unique neutron-matter EoS. Friedman and Pandharipande (FP) [78] have carried out variational many-body calculations for neutron matter EoS using the two- and three-body interactions; their EoS results are also shown in Figure 2.4. Brown [79] has carried out extensive studies of neutron matter

EoS, and has found that the FP EoS can be reproduced by the EoS given by certain empirical Skyrme effective interactions (with both two- and three-body parts). As seen in Figure 2.4, our results agree with the FP EoS impressively well. For comparison, we present in Figure 2.4 also the CDBonn EoS without the inclusion of V_{3b} (i.e. t_3=0). It is represented by the dotted-line, and is much lower than the FP EoS, particularly at high densities. For $n \lesssim n_0/2$ the effect of V_{3b} is rather small, and in this density range one may calculate the EoS using V_{low-k} alone. Clearly the inclusion of V_{3b} with $t_3 = 2000\text{MeV} \cdot \text{fm}^6$ is essential for attaining the above good agreement between our EoS's and the FP one. It is of interest that the t_3 value determined for symmetric nuclear matter turns out to be also appropriate for neutron matter.

In Figure 2.5, our results for the $\varepsilon(p)$ EoS are presented, where the EoS's given by various potentials are remarkably close to each other. The inclusion of V_{3b} is found to be also important here. As also shown in Figure 2.5, the EoS given by V_{low-k} alone (without V_{3b}) lies considerably higher than those with V_{3b}. It is of interest that for a given pressure, the inclusion of V_{3b} has a large effect in reducing the energy density. We have chosen to use Λ= 3.5 fm^{-1}, and this limits the highest pressure p_Λ which can be provided by our ring-diagram EoS calculation. As shown in the figure, the highest pressure there is about 650 MeV/fm^3. But in neutron star calculations we need EoS at higher pressure such as 1000 MeV/fm^3 (or $\sim 4 \times 10^{-4} \text{M}_\odot \text{c}^2/\text{km}^3$). The EoS at such high pressure is indeed uncertain, and some model EoS has to be employed. We shall adopt a polytrope approach, namely we fit a section of the calculated EoS near the maximum-pressure end by a polytrope $\varepsilon(p) = \alpha p^\gamma$ and use this polytrope to determine the energy density for pressure beyond p_Λ. (In our fitting the section is chosen as (0.8 to 1)p_Λ.) The polytrope EoS has been widely and successfully used in neutron star calculations [63, 80]. In fact we have found that our calculated EoS, especially the section near its high-pressure end, can be very accurately fitted by a polytrope. In Table 2.1 we list the polytropes obtained from the above fitting for four NN interactions. It is seen that the four polytropes are close to each other. The exponent γ plays an important role in determining the neutron-star maximum mass.

In obtaining the neutron star properties, we numerically solve the TOV

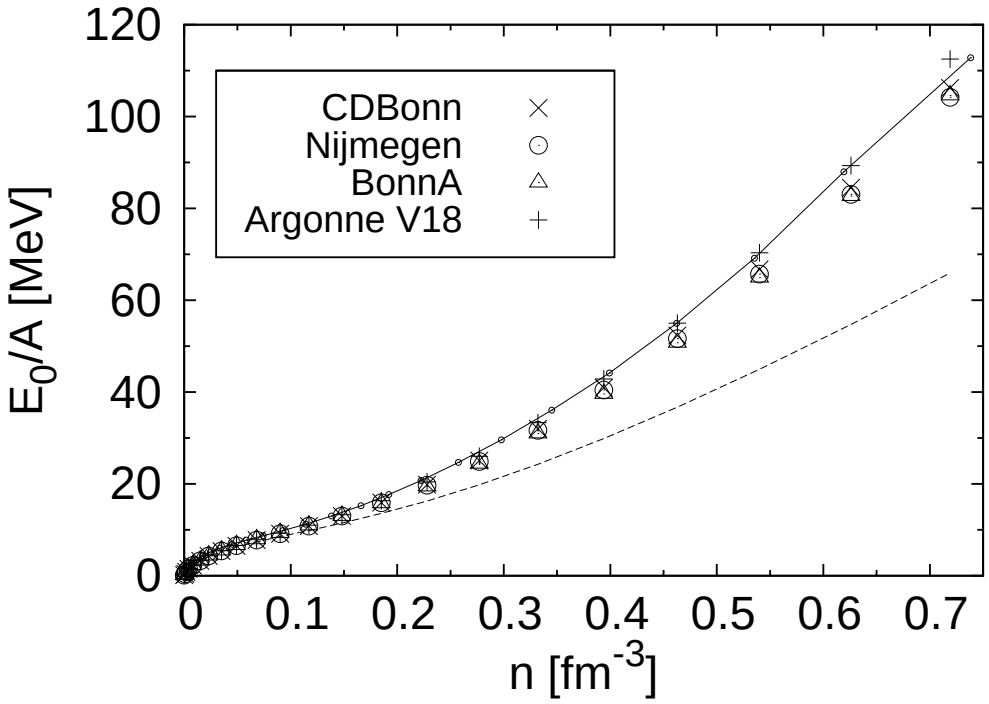

Figure 2.4: Ring-diagram neutron matter EoS obtained from four realistic NN potentials. The interaction 'V_{low-k} plus TBF' is used. The solid line with filled small circles represents the results from the variational many-body calculation of Friedman-Pandharipande. The dotted line denotes the EoS using CDBonn-V_{low-k} only.

Equation (2.1) by successive integrations. In so doing, we need to have the pressure P_c at the center of the neutron star to begin the integration. As we shall see soon, different P_c's will give, e.g. different masses for neutron stars. We also need the $\varepsilon(p)$ EoS for a wide range of pressure. As discussed above, we shall use the ring-diagram EoS for pressure less than p_Λ and the fitted polytrope EoS for larger pressure. In Table 2.2, we list some typical results for the neutron star mass M and its corresponding radius R and static moment of inertia I. (The calculation of I will be discussed later.) They were obtained with four different center pressures P_c, and as seen these properties of the neutron star vary significantly with P_c.

We present some of our calculated results for the mass-radius trajectories

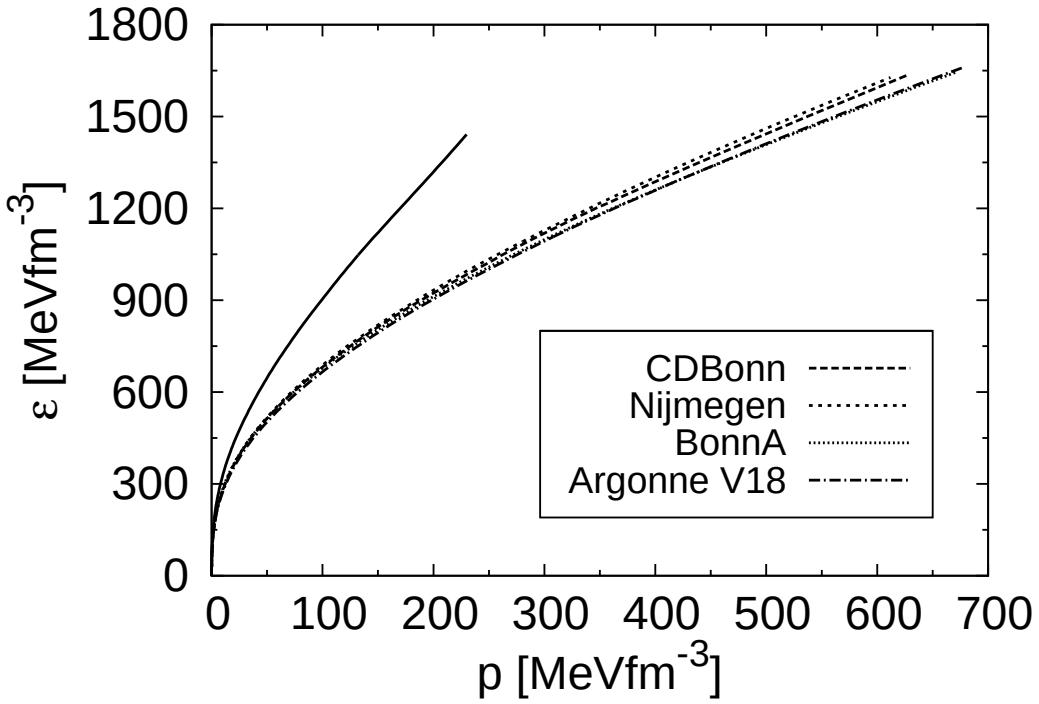

Figure 2.5: Neutron matter $\varepsilon(p)$ obtained from four realistic NN potentials. The upper-left thin line denotes the $\varepsilon(p)$ from CDBonn-V_{low-k} only.

of neutron stars in Figure 2.6. They were obtained using the CDBonn V_{low-k} (Λ=3.5 fm^{-1}) with and without the three-body force V_{3b} ($t_3 = 2000\text{MeV}\cdot\text{fm}^6$) discussed earlier. As seen, the inclusion of V_{3b} significantly increases both the maximum neutron star mass M and its corresponding radius R; the former increased from 1.2 to 1.8M$_\odot$ and the latter from 7 to 9km. The above results are understandable, because V_{3b} makes the EoS stiffer and consequently enhances both M and R. Note that our results are within the causality limit. We have repeated the above calculations using the Nijmegen, Argonne and BonnA potentials, with results quite similar to the CDBonn ones. In Figure 2.7, we present the density profiles corresponding to the maximum-mass neutron stars of Figure 2.6. It is clearly seen that the inclusion of the three-body forces have important effects in neutron-star's density distribution, reducing the central density and enhancing the outer one.

We have also performed calculations using the BR_1-scaled V_{low-k} inter-

Table 2.1: Fitted polytrope αp^{γ} for high pressure region. See text for other explanations.

Potentials	α^*	γ
CDBonn	69.69 ± 1.01	0.4876 ± 0.0022
Nijmegen	69.99 ±1.01	0.4885 ± 0.0021
BonnA	72.30 ± 1.01	0.4779 ± 0.0021
Argonne V18	67.71 ± 1.01	0.4887 ± 0.0021

$*$ unit of α is $(\mathrm{MeV/fm^3})^{1-\gamma}$.

Table 2.2: Neutron stars with different center pressures.

$P_c[\mathrm{M_\odot c^2/km^3}]$	$M[\mathrm{M_\odot}]$	$R[\mathrm{km}]$	$I[\mathrm{M_\odot km^2}]$
8.07×10^{-7}	0.101	11.58	3.78
7.18×10^{-6}	0.347	10.12	13.51
5.38×10^{-5}	1.037	10.10	50.02
2.33×10^{-4}	1.597	10.00	70.69

action (BonnA and Λ=3.5 fm^{-1}) without V_{3b}. The resulting maximum mass and its radius given are respectively $3.2\mathrm{M_\odot}$ and 12km, both considerably larger than the values of Figure 2.6. This is also reasonable, because, as was shown in Figure 2.2 the BR_1-scaled EoS is much stiffer than the 'V_{low-k} plus TBF' one. It may be mentioned that if the neutron-matter EoS given by the BR-scaled interaction is plotted in Figure 2.5, it would be very much higher, especially in the high density region, than the FP EoS shown there. We feel that the above comparison is a further indication that the linear BR_1 scaling of Equation (2.3) is not suitable for high density. It is suitable only for density up to n_0.

The moment of inertia is an important property of neutron stars [81, 82]. Here we would like to calculate this quantity using our V_{low-k} ring diagram formalism. Recall that we have used the TOV Equation (2.1) to calculate the neutron star's mass and radius, and in so doing we also obtain the density distribution inside the star. From this distribution, the moment of inertia I of neutron stars is readily calculated. It may be noted that the TOV equations are for spherical and static (non-rotating) neutron stars, and the I so obtained is the static one for spherical neutron stars. The moment of inertia for rotating stars are more complicated to calculate, but for low rotational frequencies (less

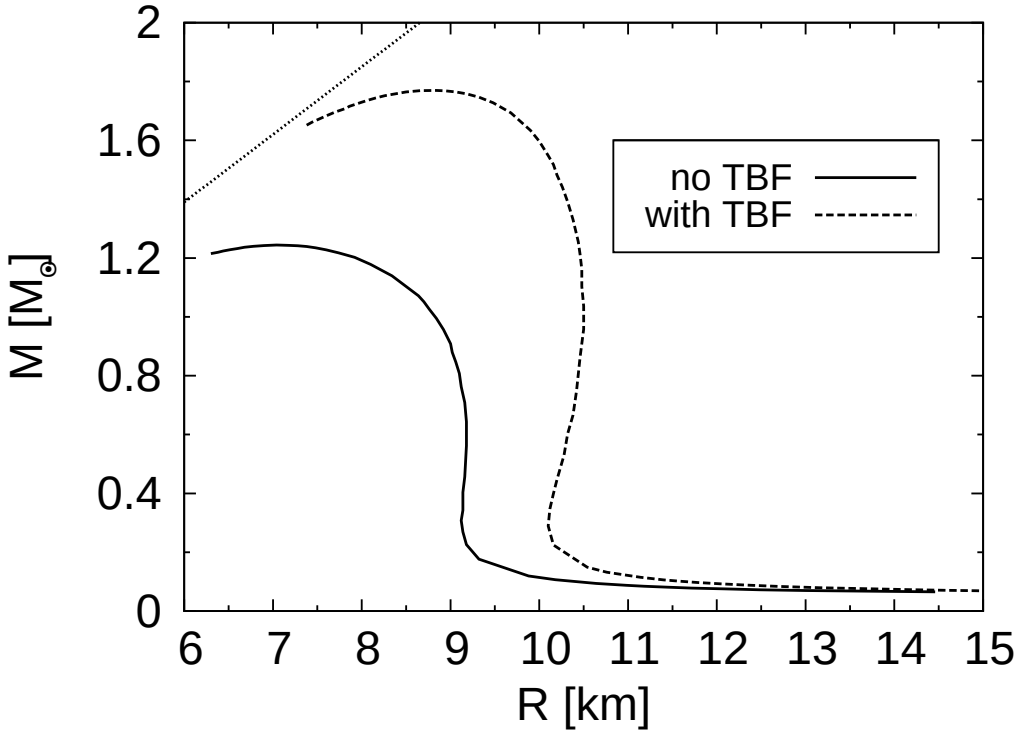

Figure 2.6: Mass-radius trajectories of pure neutron stars from ring-diagram EoSs given by the CD-Bonn V_{low-k} interaction with and without the three-body force (TBF) V_{3b}. Only stars to the right of maximum mass are stable against gravitational collapse. Causality limit is indicated by the straight line in the upper left corner.

than 300Hz) they are rather close to the static ones [82]. In Figure 2.8, we present our results for two calculations, the interactions used being the same as in Figure 2.6. It is seen that the inclusion of our three-body forces V_{3b} largely enhances the moment of inertia of maximum-mass neutron star.

The measurement of neutron-star moments of inertia is still rather uncertain, and the best determined value so far is that of the Crab pulsar ($97\pm$ 38 $M_\odot km^2$) [83]. For $M \gtrsim 1.0 M_\odot$, Lattimer and Schutz [81] have determined an empirical formula relating the moment of inertia I of neutron stars to their mass M and radius R, namely

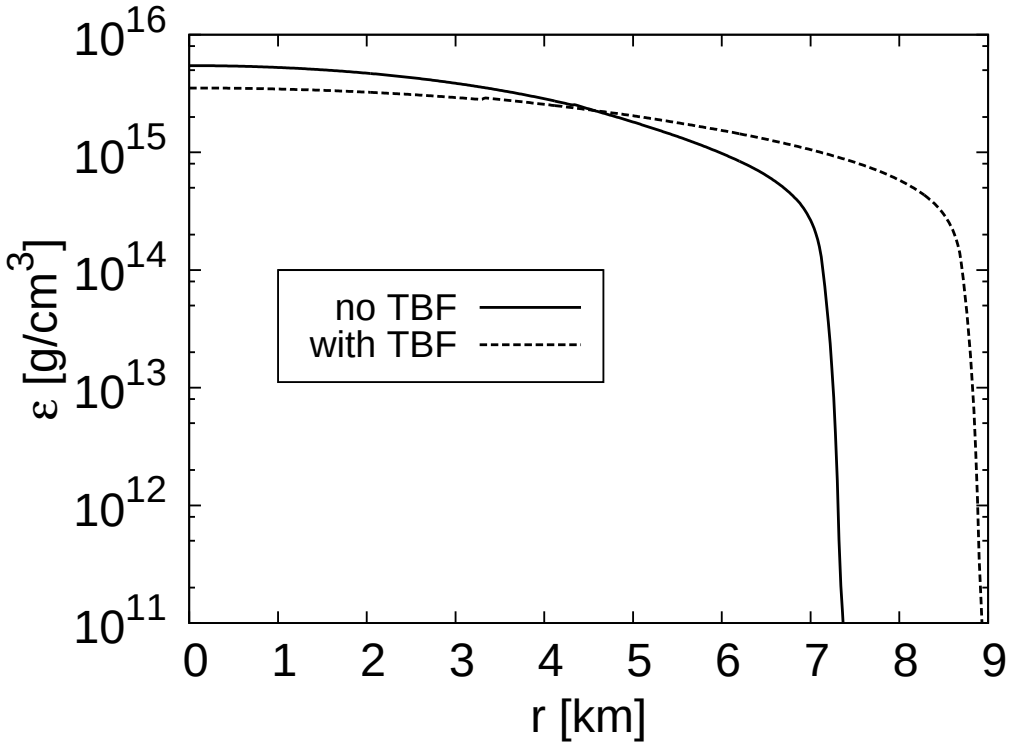

Figure 2.7: Neutron density profiles of the maximum-mass pure neutron stars obtained in Figure 2.6.

$$I \approx (0.237 \pm 0.008) M R^2 \times (1 + 4.2 \frac{M}{M_\odot} \frac{km}{R} + 90 (\frac{M}{M_\odot} \frac{km}{R})^4). \tag{2.9}$$

To check if our calculated (M, R, I) are consistent with this empirical relation, we have computed I using our calculated M and R values as inputs to Equation (2.9). Results of this computation are also shown in Figure 2.8. As shown, they are in good general agreement with the empirical formula. Especially our moment of inertia at maximum mass agrees remarkably well with the corresponding empirical value. We have also repeated the above computation with other potentials and obtained similar results.

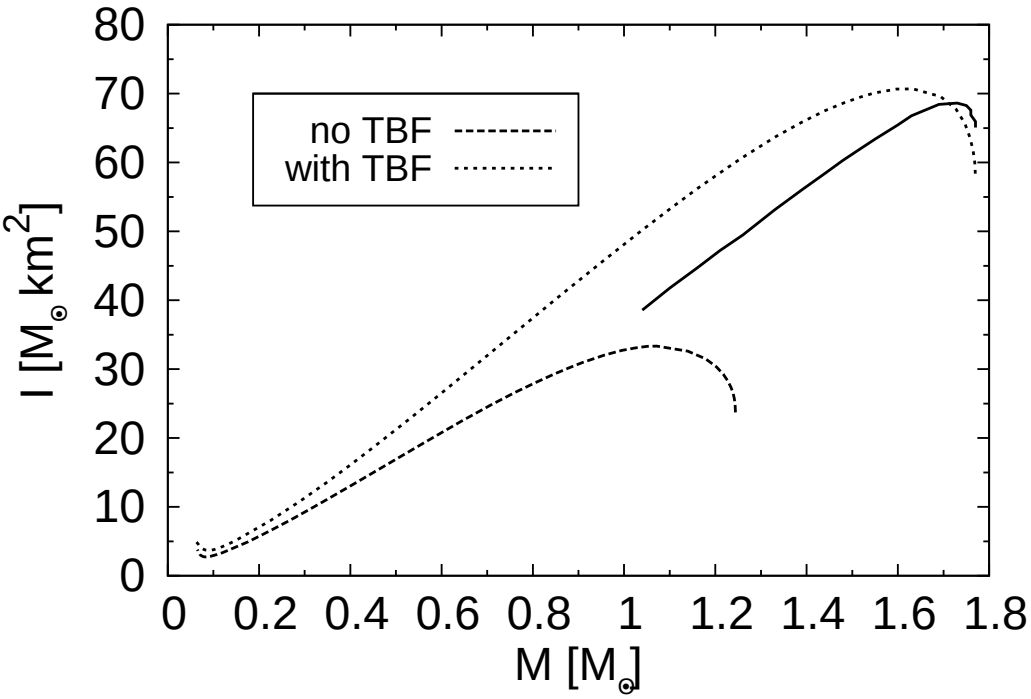

Figure 2.8: Pure neutron stars' moments of inertia calculated from CDBonn potential with and without three-body force (TBF). Results from the empirical formula 2.9 for $M \geq 1.0 M_{\odot}$ with TBF are denoted by the solid line.

2.4.2 Effects from β-stable and nuclei-crust EoSs

In the preceding subsection, we considered neutron star as composed of neutrons only, and we have obtained rather satisfactory results. Would the quality of them be significantly changed when we use a more realistic composition? As a small-step improvement, in this subsection we shall first carry out calculations using the ring-diagram β-stable EoS composed of neutrons, protons, electrons and muons only. The results of them will be briefly compared with those obtained with neutrons only. Calculations using a combination of the Baym-Pethick-Sutherland (BPS) EoS [84] inside the nuclei crust and our β-stable EoS for the interior will also be carried out. The crust of the neutron star is composed of two parts, the outer and inner crust [84–88]. The choice of the density regions defining these crusts and how to match the EoS's at the boundaries between different regions will be discussed.

Let us first discuss our β-stable EoS, where the composition fractions of its constituents are determined by the chemical equilibrium equations

$$\mu_n = \mu_p + \mu_e, \tag{2.10}$$

$$\mu_e = \mu_\mu, \tag{2.11}$$

together with the charge and mass conservation conditions

$$n_p = n_e + n_\mu, \tag{2.12}$$

$$n = n_n + n_p + n_e + n_\mu. \tag{2.13}$$

In the above, μ_n, μ_p, μ_e and μ_μ are the chemical potentials for neutron, proton, electron and muon respectively, and their densities are respectively n_n, n_p, n_e and n_μ. The total density is n. For a given n, the composition fractions of these constituents are determined by the above equations. Note that these equations are solved self-consistently, since the chemical potentials and densities are inter-dependent. We have used iteration methods for this solution. Clearly the composition fractions are not uniform inside the β-stable neutron star; they depend on the local density. For example, the proton fractions $\chi \equiv n_p/n$ in different density regions of β-stable neutron star are generally different. In solving the above equations, we have calculated the chemical potentials μ_n and μ_p using the HF approximations. Since the interactions involving electrons and muons are much weaker than the strong nucleon ones, we have treated them as free Fermi gases and in this way their chemical potentials are readily obtained.

Results for the proton fractions χ calculated from the above equations are displayed in Figure 2.9; they were obtained using four $V_{low-k}(\Lambda{=}3.5\ \mathrm{fm}^{-1})$ interactions, all with the same three-body forces $V_{3b}(t_3 = 2000\mathrm{MeV}\cdot\mathrm{fm}^6)$. We note that our calculated proton fractions are all quite small, the maximum proton fraction given by BonnA potential being $\sim$ 7% and that from both Argonne V18 and Nijmegen potentials being $\sim$ 2%. Also they exhibit a saturation behavior, which reaches a maximum at density between $\sim$0.6 and $\sim$0.8 fm^{-3} and diminishes to near zero on both sides. Our results suggest that a β-stable neutron star has small proton admixtures only within an intermediate

layer. Proton fractions in β-stable neutron stars are an important topic and have been extensively studied [7, 89]. They are closely related to the density dependence of symmetry energy, which is being determined in several laboratories [7]. There have been a number of calculations for these fractions using different many-body methods and different interactions; their results are, however, widely different from each other (see Fig. 1 of [89]), with some of them being close to ours. Further studies of the proton fractions would certainly be in need and of interest.

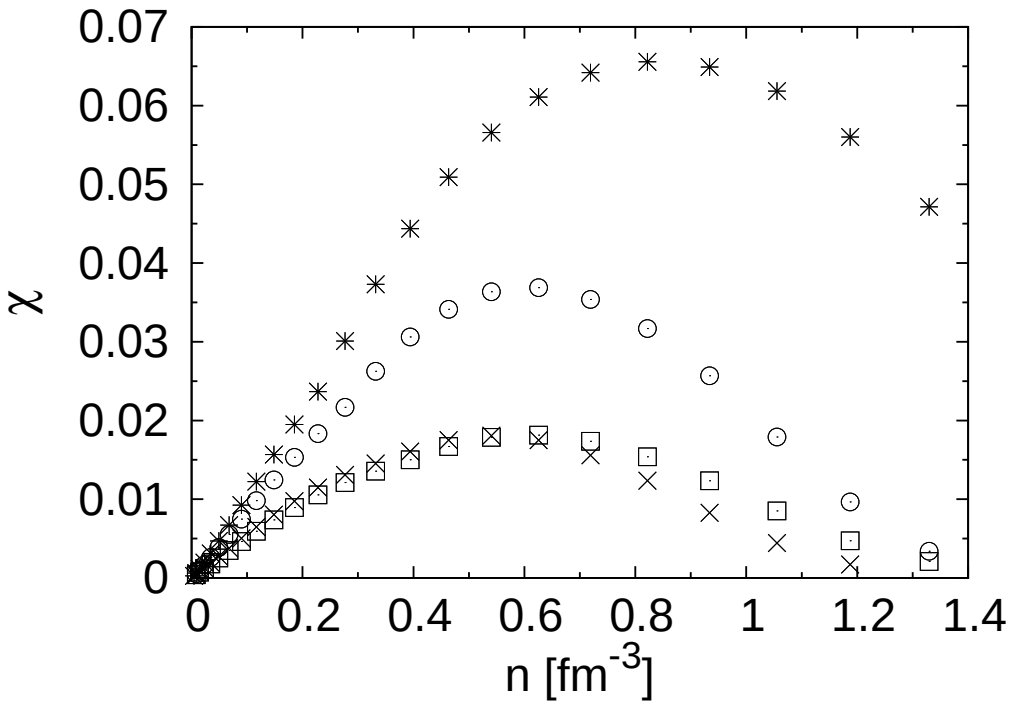

Figure 2.9: Proton fraction of β-stable neutron star from realistic NN potentials. Symbols are BonnA($*$), CDBonn($\circ$), Argonne V18 ($\Box$) and Nijemgen ($\times$). The interaction 'V_{low-k} plus TBF' is used.

With our calculated proton fractions, we proceed to calculate the properties of β-stable neutron stars whose energy-density EoS is $\varepsilon(n) = \varepsilon_{np}+\varepsilon_e+\varepsilon_\mu$, where n is the total density of Equation 2.13. Electrons and muons are treated as free Fermi gases and their energy densities are readily obtained. ε_{np} is the neutron-proton energy density to be evaluated using the ring-diagram method. This

energy density is in fact $\varepsilon_{np}(n_{np}, \alpha)$ where $n_{np} = n_n + n_p$, the combined nucleon density, and α is the asymmetry parameter of Equation (2.2). Calculations for β-stable neutron stars are more complicated than the pure neutron matter case of the previous subsection, for which $\alpha = 1$ independent of the total density n. In contrast, here we need to calculate ε_{np} for many (n_{np}, α) values since they are dependent on n (see Equations (2.11 - 2.13). Then the $\varepsilon_{np}(p)$ EoS, which expresses energy density in terms of pressure p, is obtained by density differentiations of $\varepsilon_{np}(n_{np}, \alpha)$, similar to what we did in the previous subsection. By solving the TOV equations, the various properties of β-stable neutron stars are obtained.

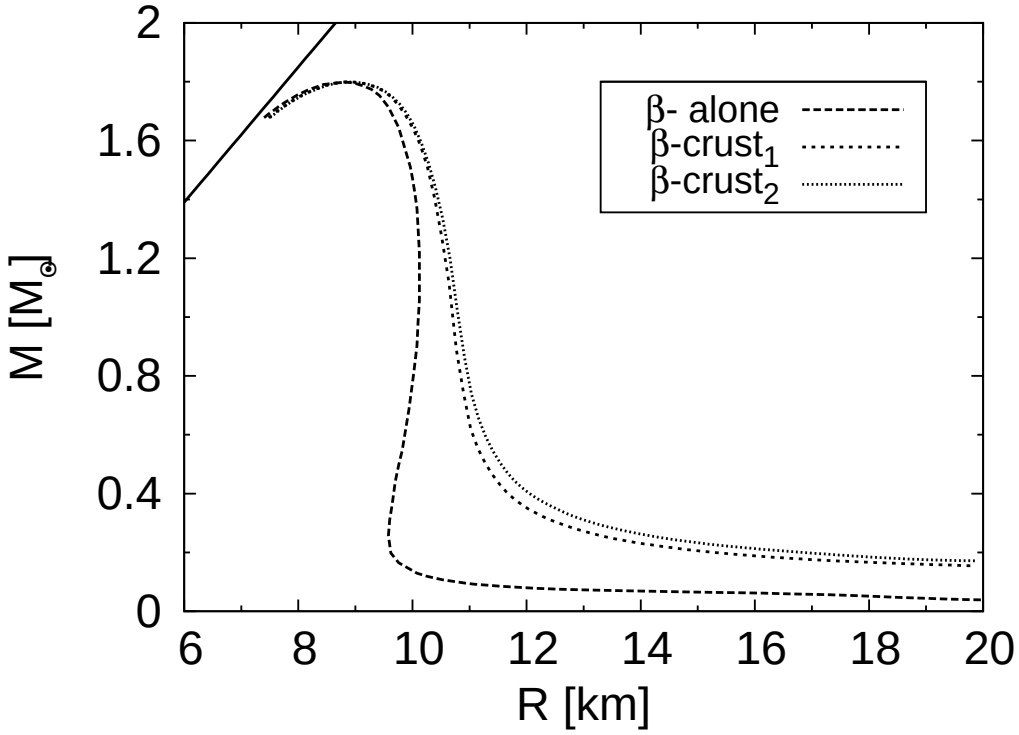

Figure 2.10: Mass-radius trajectories of neutrons stars obtained using only the ring-diagram β-stable EoS (β-alone) and a combination of the ring and nuclei-crust EoSs with inner-crust boundary n_t= 0.04 (β-crust$_1$) and 0.05 fm^{-3} (β-crust$_2$). The 'CDBonn-V_{low-k} plus TBF' potential is used for the ring EoS. See the caption of Figure 2.6 for other explanations.

To illustrate our results for the mass-radius trajectories for the β-stable

neutron stars, we have performed such a calculation for the CDBonn potential and present its results in Figure 2.10 (labelled 'β-alone'). As seen it is quite similar to the corresponding one of Figure 2.6 for the pure neutron EoS. The trajectories using the same method but with other NN potentials (Nijmegen, Argonne V18 and BonnA) have also been calculated, and are also very similar to the corresponding pure-neutron ones. This close similarity indicates that the effect from the admixture of (p, e, μ) is not important as based on our present calculation, this being largely due to the smallness of the proton fractions discussed earlier.

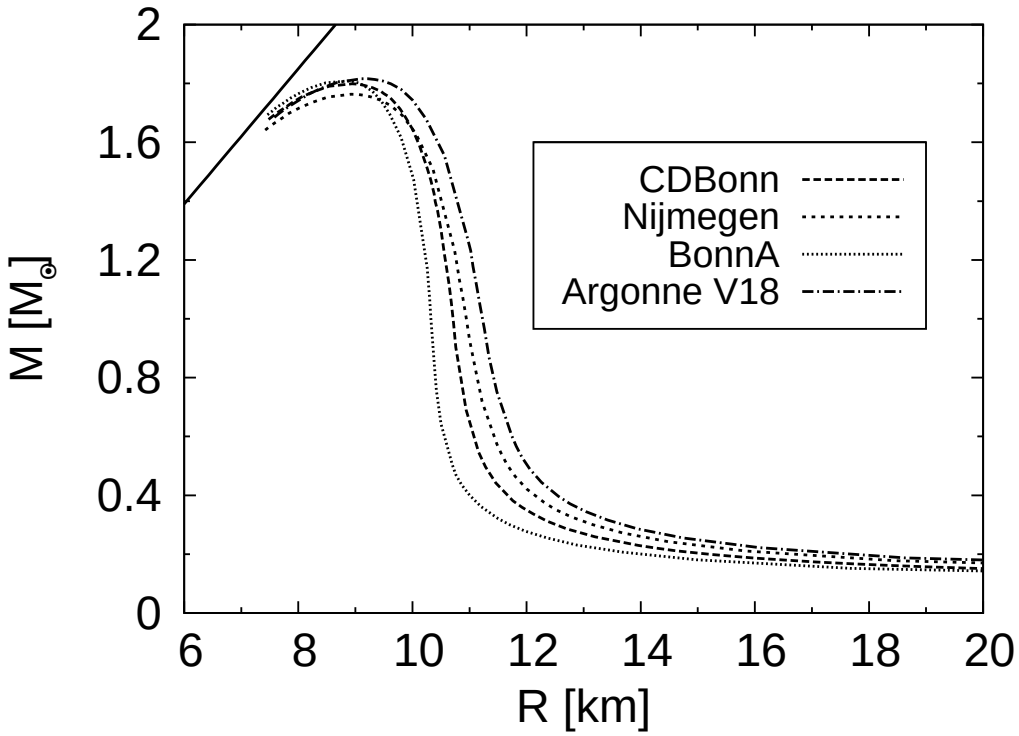

Figure 2.11: Mass-radius trajectories of neutron stars calculated with a combination of β-stable ring-diagram EoS for the core and the nuclei-crust EoSs for the crusts. Ring-diagram EoSs given by four NN potentials, all with the V_{3b} three-body force, Λ=3.5fm^{-1} and $t_3 = 2000\text{MeV} \cdot \text{fm}^6$ are used. n_t=0.04 fm^{-3} is used for the inner crust boundary. See the caption of Figure 2.10 for other explanations.

So far we have carried out microscopic calculations of neutron stars with the assumption that they are made of a homogeneous medium composed of

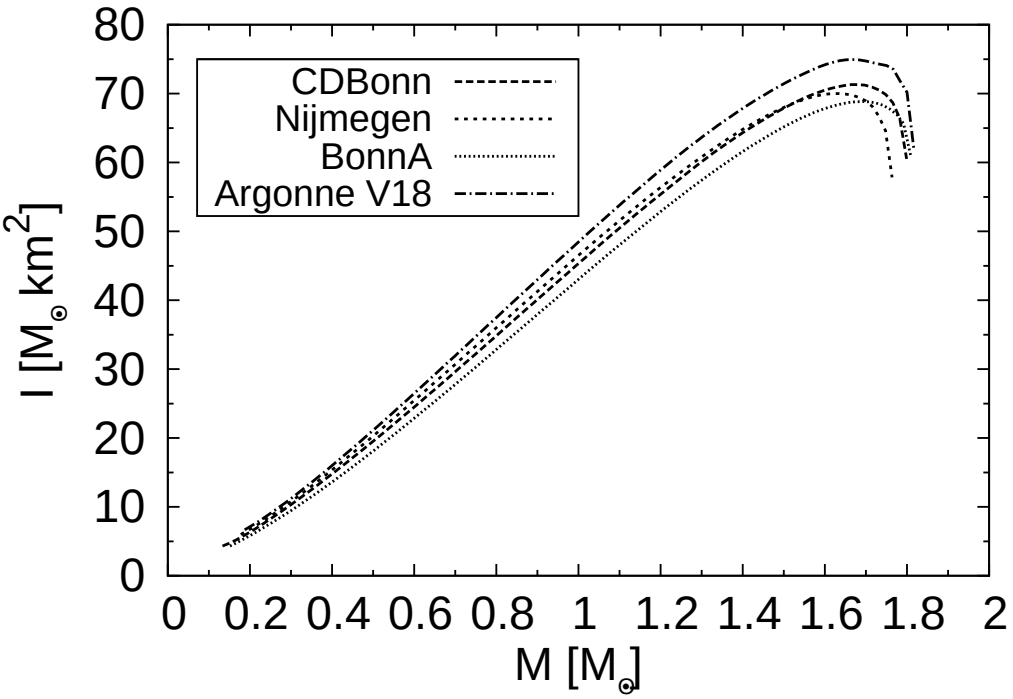

Figure 2.12: Moments of inertia for β-stable neutron stars in Figure 2.11.

neutrons, protons, electrons and muons. It is believed that the crust of neutron stars does not consist of such a homogeneous medium; it is "nuclei crust" where nucleons are clustering into nuclei [84, 85]. Here we would like to make some estimates on the nuclei-crust corrections to our calculations. In our estimates, we employ three different EoSs for the outer-, inner-crust and core regions. These regions refer to the density regions $n < n_{out}$, $n_{out} < n < n_t$ and $n > n_t$ respectively, with $n_{out} = 2.57 \times 10^{-4}\text{fm}^{-3}$ [85, 87]. n_t is the transition density separating the inner crust and the homogeneous core, and several models have been employed to determine its value [85, 86]. For the outer-crust region we use the well-known BPS nuclei-EoS [84]. For the core region, our β-stable ring-diagram EoS will be employed. The EoS in the inner-crust region is somewhat uncertain, and so is the transition density separating the inner crust and core. We shall use in our calculations $n_t = 0.04$ and 0.05fm^{-3} [85, 86] to illustrate the effect of the nuclei crust. Following [85, 88], we use in the inner-crust region a polytropic EoS, namely $p = a + b\varepsilon^{4/3}$ with the constants a and b

Table 2.3: Maximum mass and the corresponding radius and moment of inertia of β-stable neutron stars with nuclei-crust boundary n_t=0.04 fm^{-3}. The three-body force V_{3b} is included for the results in the first four rows, but is not in the last.

Potentials	$M[M_\odot]$	$R[km]$	$I[M_\odot km^2]$
CDBonn	1.80	8.94	60.51
Nijmegen	1.76	8.92	57.84
BonnA	1.81	8.86	61.09
Argonne V18	1.82	9.10	62.10
CDBonn(no BRS)	1.24	7.26	24.30

determined by requiring a continuous matching of the three EoS's at n_{out} and n_t.

In Figure 2.10, our results for the mass-radius trajectories using the above three EoS's with n_t=0.04 and 0.05 fm^{-3}, labeled β-crust$_1$ and β-crust$_2$ respectively, are compared with the trajectory given by the β-stable alone (namely n_t=0). As seen, the effect from the nuclei-crust EoS on the maximum neutron-star mass and its radius is rather small, merely increasing the maximum mass by $\sim 0.02M_\odot$ and its radius $\sim$ 0.1km as compared to the β-alone ones. However, its effect is important in the low-mass large-radius region, significantly enhancing the neutron-star mass there. That the maximum mass is not significantly changed by the inclusion nuclei-crust EoS is consistent with Figure 2.7 which indicates that the mass of maximum-mass neutron stars is confined predominantly in the core region. It may be mentioned that our ring-diagram EoS is microscopically calculated from realistic NN interactions, while the crust EoSs are not. So there are disparities between them. It would be useful and of much interest if the crust EoSs can also be derived from realistic NN interactions using similar microscopic methods. Further studies in this direction are needed.

In. Figure 2.11 we present our mass-radius results using the above three EoSs with n_t=0.04 fm^{-3}. Four NN potentials are employed, and they give similar trajectories, especially in the high- and low-mass regions. A corresponding comparison for the moment of inertia is presented in Figure 2.12; again the results from the four potentials are similar. In Table 2.3, our results for the

maximum neutron mass and its radius and moment of inertia using the above combined EoSs are presented, and as seen the results for the maximum-mass neutron star given by the four potentials are indeed close to each other. It is also seen that the effect of the three-body force is quite important for M, R and I, as illustrated by the CDBonn case.

2.5 Conclusion

We have performed neutron-star calculations based on two types of EoS's: the pure-neutron ring-diagram, the β-stable (n, p, e, μ) ring-diagram EoS's. The ring-diagram EoS, where the *pphh* ring diagrams are summed to all orders, are microscopically derived using the low-momentum interaction V_{low-k} obtained from four realistic NN potentials (CDBonn, Nijmegen, Argonne V18, BonnA). We require that the EoS used for neutron stars should give satisfactory saturation properties for symmetric nuclear matter, but this requirement is not met by our calculations using the above potentials as they are. Satisfactory nuclear matter saturation properties can be attained by using the above potentials with the commonly used linear BR scaling (BR_1) where the the masses of in-medium mesons are slightly suppressed compared with their masses in vacuum. However, this linear scaling is not suitable for neutron stars; the maximum mass of neutron star given by our BR_1 ring-diagram calculation is $\sim 3.2 M_\odot$ which is not satisfactory. BR_1 is suitable only for low densities; it needs some extension so that it can be applied to the high densities inside the neutron star. We have used an extrapolation method for this extension, namely we add an empirical Skyrme-type three-body force V_{3b} to V_{low-k}. We have found that the EoS given by this extrapolation agrees well with the EoS obtained from linear BR_1 scaling for low densities, but for high densities it agrees well with that from a nonlinear BR_2 scaling. The EoS using the above extrapolation gives satisfactory saturation properties for symmetric nuclear matter, and for neutron matter it agrees well with the FP EoS for neutron matter.

The effects from V_{3b} have been found to be both important and desirable. Compared with the results given by the unscaled V_{low-k}, it increases the max-

imum mass of the neutron star and its radius and moment of inertia by $\sim 40\%$, $\sim 20\%$ and $\sim 150\%$ respectively. The proton fractions are found to be generally small ($< 7\%$), making our neutron-star results using the pure-neutron EoS and those using the β-stable EoS nearly the same. We have estimated the effect from the nuclei-crust EoS's by using a combination of three EoSs: the BPS EoS for the outer crust, a fitted polytropic EoS for the inner crust and our β-stable ring-diagram EoS for the core region. The effect from the nuclei-crust EoS's on the maximum neutron-star mass and its radius is found to be rather small, as compared with those given by the calculation where the β-stable EoS is used throughout. However, its effect is important in the low-mass large-radius region, significantly enhancing the neutron-star mass there. Using the above combined three EoSs, our results for neutron star's maximum mass and its radius and moment of inertia are, respectively, $\sim 1.8 M_\odot$, ~ 9km and $\sim 60 M_\odot \mathrm{km}^2$, all in good agreement with accepted values.

How to extend the BR scaling to high densities is still an open question. Although we have obtained satisfactory results by using a nonlinear scaling for the high-density region, or equivalently a Skyrme-type three-body force, for the extension, it would still be certainly useful and interesting to explore other ways for doing so. Further studies in this direction would be very helpful in determining the medium dependent modifications to the NN potentials in the high-density region.

Chapter 3

Neutron matter at unitary limit

3.1 Introduction

The 'unitary limit' of an ultracold Fermi gas refers to the special scenario where the inter-atomic interaction is tuned to have its scattering length a_s approaching infinity ($a_s >> k_F^{-1}$), leaving the Fermi momentum k_F as the only relevant length scale in the many-body system. This limit was discussed as early as 1999 by Bertsch [90], who challenged many-body theorists with the question "What are the ground state properties of neutron matter, interacting with an infinite scattering length?". Under such condition the Fermions are strongly interacting, thus the determination of the ground state is highly non-trivial. However, the EoS at this limit is expected to be an universal expression $E_0 = \xi E_0^{free}$ where ξ is an universal constant for any underlying Fermion systems. It is of much interest to determine ξ experimentally or derive it theoretically, many such attempts having been made [43, 51–56, 91–109]. By far, the best numerical estimate on ξ is considered to be $\xi = 0.44(1)$ [54], 0.42(1) [55] and 0.40(1) [56] according to quantum Monte Carlo methods. The scattering length of trapped ultracold Fermi gases can in fact be magnetically tuned [49, 50] by way of a Feshbach resonance. This is indeed a very important achievement, and it is based on this that the above constant ξ for trapped ultracold Fermi gases can be experimentally measured. Several recently reported experimental values for ξ are 0.46 ± 0.05 [51], $0.46^{+0.12}_{-0.05}$ [52]

and 0.39(2) to 0.435(15) [53].

Previous work [43] has calculated the constant ξ for neutron matter using a tuned CDBonn realistic NN potential [10]. Unlike the case of trapped Fermion gases, here the scattering length of NN interactions still cannot be tuned experimentally. Thus we have chosen to tune the NN interaction by adjusting its meson parameters, in line with the BR scaling [20] that the meson masses in a nuclear medium as suppressed compared with their in-vacuum values. The $^1S_0$ scattering length of the original CDBonn potential is $a_s = -18.9$ fm, which is already fairly large. We have found that to have a very large scattering length (such as -12070fm) the meson parameters of the CDBonn potential need to be adjusted only slightly (about 2%) [43]. This tuned CDBonn potential actually has given ξ quite close to 0.44 for a wide range of densities(~ 0.02 to ~ 0.09 fm^{-3}) [43].

In this chapter, we investigate mainly the following question: Is the constant ξ given by other unitarity potentials, defined as those with infinite scattering lengths, also close to 0.44? This constant is supposed to be a universal constant, and then its value should be independent of the detailed structure of the potentials as long as they have infinite scattering length. In other words, ξ given by all other unitarity potentials should in principle be the same. It may be difficult to prove this analytically. Before one can do so, it should be useful and of interest to first check this universality property numerically as we shall do in this chapter. As it is rather involved to tune the various realistic NN potentials [10–13] to infinite scattering length, we have chosen to calculate ξ from a family of simple hard-core square-well (HCSW) potentials

$$\begin{aligned} V(r) &= V_c; \quad r < r_c \\ & \quad V_b; \quad r_c < r < r_b \\ & \quad 0; \quad r > r_b. \end{aligned} \tag{3.1}$$

An advantage of this type of potentials is that their scattering lengths can be given analytically and thus exact unitarity potentials can be readily obtained. The above HCSW potentials are clearly very different from the realistic NN potentials, yet as we shall discuss later the constant given by various HCSW

potentials are all amazingly close to 0.44, as is also given by the tuned CDBonn potential.

3.2 Hard-core square-well unitarity potentials

There are several realistic NN potentials (CDBonn[10], Nijmegen[11], Argonne V18 [12] and BonnA [13]) which all describe the two-nucleon low-energy experimental data very accurately. It would be of interest to obtain unitarity potentials from them by tuning their interaction parameters slightly. But technically this is not easy to carry out. So far only the CDBonn potential has been tuned to attain this limit (a_s=-12070 fm)[43]. In this chapter, we choose HCSW potentials as given by Equation (3.1) for further studying the properties of neutron matter at the unitary limit. An advantage of using them is that their scattering length a_s can be analytically obtained, allowing us to study the properties of neutron matter using many HCSW potentials with any chosen scattering lengths (including infinity).

As indicated in Equation (3.1), the HCSW potential is characterized by the height V_c of the repulsive core, the depth V_b of its attractive well, and the respective ranges r_c and r_b. In this chapter, we consider neutron matter with interactions only in the $^1S_0$ channel, whose phase shift δ is readily obtained from Equations (3.3 - 3.3). Namely

$$\tan(\delta + K_3 r_b) = \frac{K_3}{K_2}\tan(K_2 r_b + \alpha), \tag{3.2}$$

$$\tan(\alpha + K_2 r_c) = \frac{K_2}{K_1}\tanh(K_1 r_c), \tag{3.3}$$

with

$$K_1 = \sqrt{(V_c - E)\frac{m}{\hbar^2}},$$

$$K_2 = \sqrt{(E - V_b)\frac{m}{\hbar^2}},$$

$$K_3 = \sqrt{E\frac{m}{\hbar^2}},$$

where E is the scattering energy in the center-of-mass frame. From the above results, the scattering length a_s is obtained from a low energy expansion of $kcot\delta$ as

$$a_s = -\frac{B}{A} \tag{3.4}$$

with

$$\begin{aligned} A &= K_{10}K_{20} - K_{20}^2 \tanh(K_{10}r_c)\tan[K_{20}(r_b - r_c)], \\ B &= K_{20}\tanh(K_{10}r_c) + K_{10}\tan[K_{20}(r_b - r_c)] - r_b K_{10}K_{20} \\ &\quad + r_b K_{20}^2 \tanh(K_{10}r_c)\tan[K_{20}(r_b - r_c)], \end{aligned} \tag{3.5}$$

where

$$K_{10} = \sqrt{V_c \frac{m}{\hbar^2}}, \quad K_{20} = \sqrt{-V_b \frac{m}{\hbar^2}}.$$

The effective range r_e for this potential can also be derived analytically; the result is not presented here because it is fairly lengthy.

Equation (3.4) implies that the condition for being a unitarity potential (infinite scattering length) is A=0, namely

$$r_b - r_c = \frac{1}{K_{20}} \tan^{-1}\left[\frac{K_{10}}{K_{20}\tanh(K_{10}r_c)}\right]. \tag{3.6}$$

It is well known that when the potential is tunned to the unitary limit (the Feshbach resonance), it has a bound state with its energy approaching to zero. It is readily checked that the condition for having such a bound state is the same as the A=0 one given above.

Table 3.1: Three different unitarity HCSW potentials.

Potentials	V_c[MeV]	r_c[fm]	V_b[MeV]	r_b[fm]	$a_s[\times 10^6$fm]	r_e [fm]
HCSW01	3000	0.15	-20	2.31	15.2	2.36
HCSW02	3000	0.30	-30	2.03	3.38	2.21
HCSW03	3000	0.50	-50	1.81	-4.58	2.20

The above condition enables us to construct any number of unitarity potentials by varying any three of the four parameters V_c, V_b, r_c and r_b. Some examples for such potentials are listed in Table 3.1. As seen, they all have

very large (infinite) scattering lengths while the potentials themselves are significantly different from each other. For example, the depth of the attractive parts of them changes from -20 to -50 MeV. The effective ranges of these potentials are also listed, with all of them being close to the unitarity CDBonn's r_e of 2.54fm^{-1}. These potentials will be used to calculate the universal ratio $\xi \equiv E_0/E_0^{free}$ for neutron matter. As we shall soon discuss, the ratios ξ given by these three largely different potentials are in fact nearly identical to each other.

3.3 Model-space Hartree-Fock methods

We used the ring-diagram method [43, 44] to calculate the neutron matter EoS. As discussed in section 1.4, the ratio ξ is readily obtained, namely $\xi = 1 + \Delta E_0/E_0^{free}$. Since we include only the $^1S_0$ interaction, the quasi bosons in our present ring-diagram calculation are in fact all BCS-pairing bosons ($^1S_0$).

The ring-diagram method described in section 1.4 is a model-space formalism, where all nucleons are confined within a momentum model space P($k < \Lambda$), and the decimation scale for the V_{low-k} interaction is the same Λ. The Equation (1.6) for the energy shift ΔE_0 is rather complicated, and is not convenient for studying the properties of the underlying interaction at the unitary limit. To have a clearer way to study these properties, we have considered a simpler method to calculate ΔE_0, namely a model-space HF method (MSHF). In this method, we have

$$\Delta E_0 = \frac{1}{2}\Sigma_{k_1,k_2\leq k_F}\langle \boldsymbol{k}_1\boldsymbol{k}_2|V_{low-k}^{k_F}|\boldsymbol{k}_1\boldsymbol{k}_2\rangle. \tag{3.7}$$

This is also a model-space approach where all nucleons are confined within a model space P($k < k_F$), but the MSHF has a special feature in that the interaction used is renormalized according to the same P($k < k_F$), namely the V_{low-k} interaction is calculated with $\Lambda = k_F$ as denoted by $V_{low-k}^{k_F}$. A main difference between the MSHF and the usual HF calculations is that the interaction used in the latter is not required to be renormalized according to the above model space while it is so for the former. In fact the MSHF is

equivalent to the ring-diagram method when one chooses Λ to be its smallest value allowed by the Pauli-exclusion principle, namely k_F. When $\Lambda = k_F$, diagrams like (b) and (c) of Figure 1.5 no longer exist (since particles with $k > k_F$ are disallowed in the model space); only diagram (a) remains, which is just the MSHF. It may be mentioned that the MSHF is rather similar to the familiar BHF method [13, 31, 34]. They both employ the same model space P($k < k_F$) (all nucleons confined within the Fermi sea), but they employ different model-space effective interactions. In the BHF the energy-dependent G-matrix interaction is used while in the MSHF the energy-independent V_{low-k} interaction is employed; both include renormalization from all-order particle-particle correlations beyond k_F, but for G the renormalization is carried out using an energy-dependent method while an energy-independent one is applied for V_{low-k}. The MSHF ground-state energy is given by the sum of the kinetic energy and a simple integral, namely

$$\begin{aligned} \frac{E_0}{A} &= \frac{3}{5}\varepsilon_F + \frac{8}{\pi}\int_0^{k_F} k^2 dk[1 - \frac{3k}{2k_F} + \frac{k^3}{2k_F^3}] \\ &\quad \times \sum_\alpha (2J_\alpha + 1)\langle \alpha, k|V_{low-k}^{k_F}|\alpha, k\rangle, \end{aligned} \tag{3.8}$$

In this equation $\varepsilon_F = \frac{\hbar^2 k_F^2}{2m}$, k denotes the two-nucleon relative momentum and J_α is the total angular momentum for the partial wave α. (We consider neutrons with interactions only in the $^1S_0$ partial wave, and thus the above summation has only one term.) The above result may be useful for studying the properties of the V_{low-k} interaction at the unitary limit. If the ratio E_0/E_0^{free} is equal to a constant ξ at this limit, then the above equation implies that $V_{low-k}^{k_F}$ at this limit must satisfy

$$\begin{aligned} \frac{3\varepsilon_F}{5}(\xi - 1) &= \frac{8}{\pi}\int_0^{k_F} k^2 dk[1 - \frac{3k}{2k_F} + \frac{k^3}{2k_F^3}] \\ &\quad \times \langle {}^1S_0, k|V_{low-k}^{k_F}|{}^1S_0, k\rangle. \end{aligned} \tag{3.9}$$

This is a rather strong constraint for the interaction. Clearly there are many potentials which can satisfy the above constraint, allowing many potentials to

have the same ratio ξ. In the following section, we shall discuss and numerically check this constraint.

Within the above MSHF framework, the single-particle (s.p.) potential U is given [45] as

$$\begin{aligned} U(k_1) &= \sum_{\alpha}(2J_\alpha+1)\{\frac{16}{\pi}\int_0^{k_-} k^2dk\langle k\alpha|V_{low-k}^{k_F}|k\alpha\rangle, \\ &+\frac{2}{k_1\pi}\int_{k_-}^{k_+} kdk[k_F^2-k_1^2+4k(k_1-k)] \\ &\times\langle k\alpha|V_{low-k}^{k_F}|k\alpha\rangle\} \end{aligned} \tag{3.10}$$

with

$$k_- = (k_F-k_1)/2, \quad k_+ = (k_F+k_1)/2.$$

The MSHF s.p. spectrum is

$$\varepsilon(k_1) = \frac{\hbar^2k_1^2}{2m} + U(k_1), \tag{3.11}$$

which can be well approximated by

$$\varepsilon(k_1) = \frac{\hbar^2k_1^2}{2m^*} + \Delta, \tag{3.12}$$

where m^* is the effective neutron mass in medium and Δ is a constant related to the depth of the potential well. The MSHF ground-state energy can be expressed in terms of m^* and Δ. Then if this energy is equal to ξE_0^{free} at the unitary limit, the MSHF m^* and Δ should satisfy the linear constraint

$$\xi = \frac{1}{2} + \frac{m}{2m^*} + \frac{5\Delta}{6\varepsilon_F}. \tag{3.13}$$

In the following section, we shall also discuss and numerically check the above linear constraint concerning the MSHF sp potential.

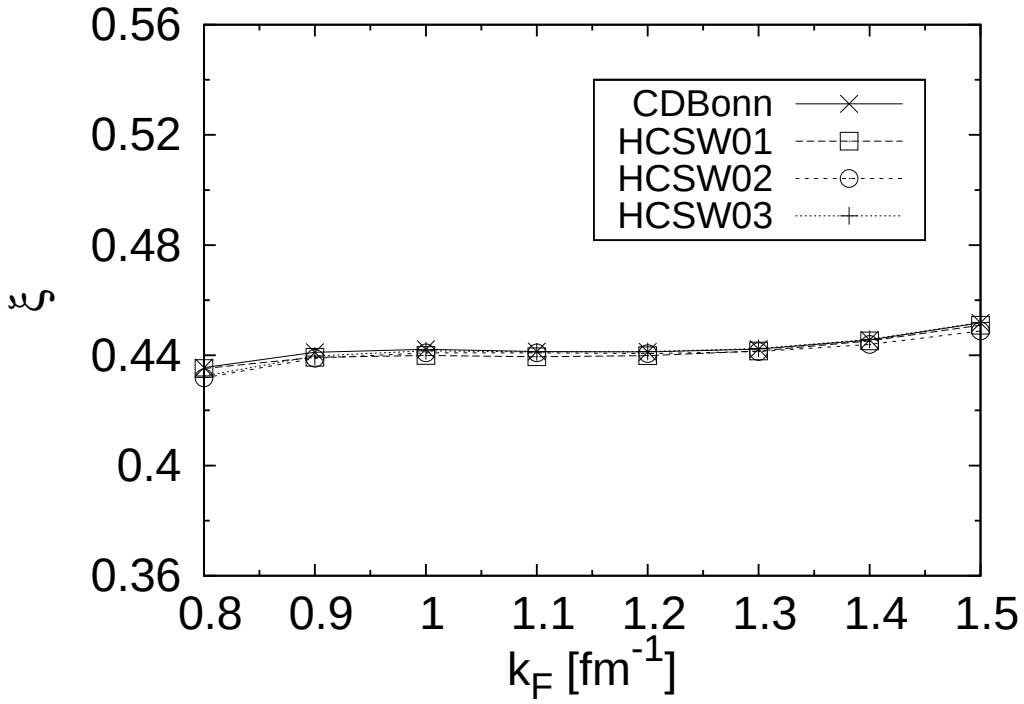

Figure 3.1: Universal ratio ξ for the cold neutron matter. Four unitarity potentials (three HCSW and one CDBonn) are used in the all-order ring diagrams summation scheme.

3.4 Results and Discussion

We first calculate the ratio ξ with the ring-diagram method using both the three HCSW unitarity potentials of Table 3.1 and the unitarity CDBonn potential ($a_s = -12070$fm) [43]. As shown in Figure 3.1, the results given by these four potentials are all quite close to 0.44. A common decimation scale of $\Lambda = 2.1$ fm^{-1} has been used for the results presented there. We have found that the ξ values given by the ring-diagram calculations using the HCSW potentials are rather stable (variation less than 0.002) with Λ in the range between 2.0 and 2.4 fm^{-1}. As found in [43], they are also quite stable for the unitarity CDBonn potential in the same range. Since these potentials have given nearly identical results for the ratio ξ, it is of interest to compare their $V_{NN}(k,k)$ matrix elements from which the ξ's are calculated. Such a

comparison is presented in Figure 3.2, and as seen they are actually quite different. It is indeed surprising that the ratios ξ given by these vastly different interactions are nearly the same. To illustrate the key role of the unitary limit, we further calculate the ratios ξ near the unitary limit as displayed in Figure 3.3. When a_s is away from the unitary limit, the ξ values given by these potentials are noticeably different, but they converge to a common value only as $1/a_s$ approaching zero. The above results strongly suggest that the ratio ξ is indifferent to the details of the underlying potentials, as long as they have infinite (or very large) scattering lengths, namely that they are all unitarity potentials.

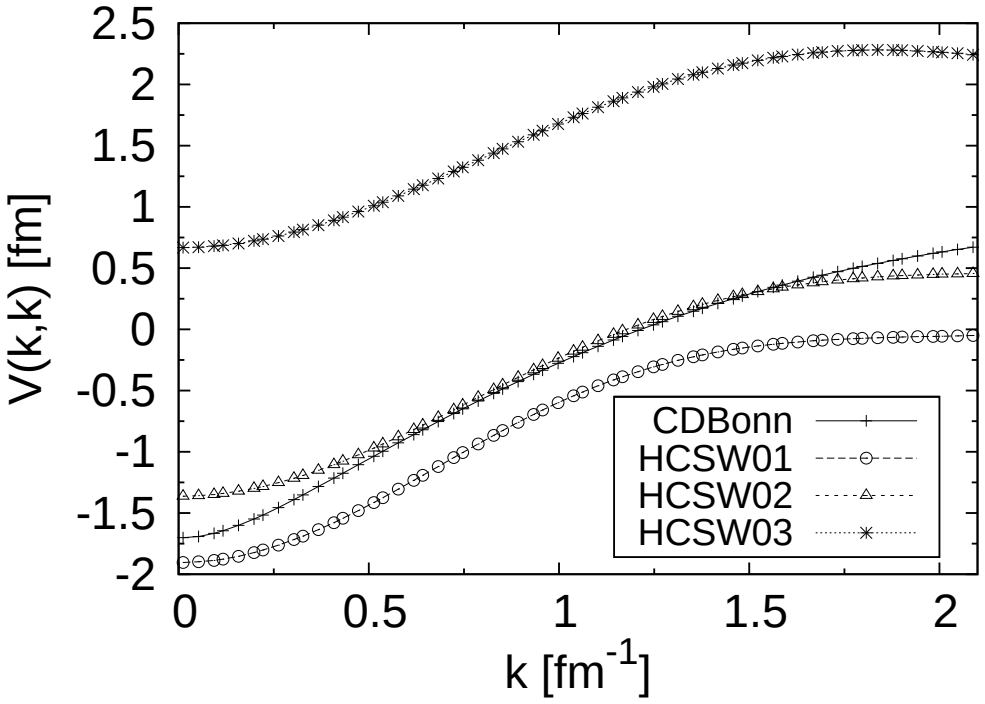

Figure 3.2: The diagonal matrix elements $V_{NN}(k,k)$ of the four original unitarity potentials (three HCSW and one CDBonn).

Using the above four unitarity potentials, we have also calculated the ratios ξ using the MSHF method (see Equation (3.9)). The results are presented in Figure 3.4, and as seen the results given by the four potentials are nearly identical and they are all quite close to 0.44 over a wide range of densities. It

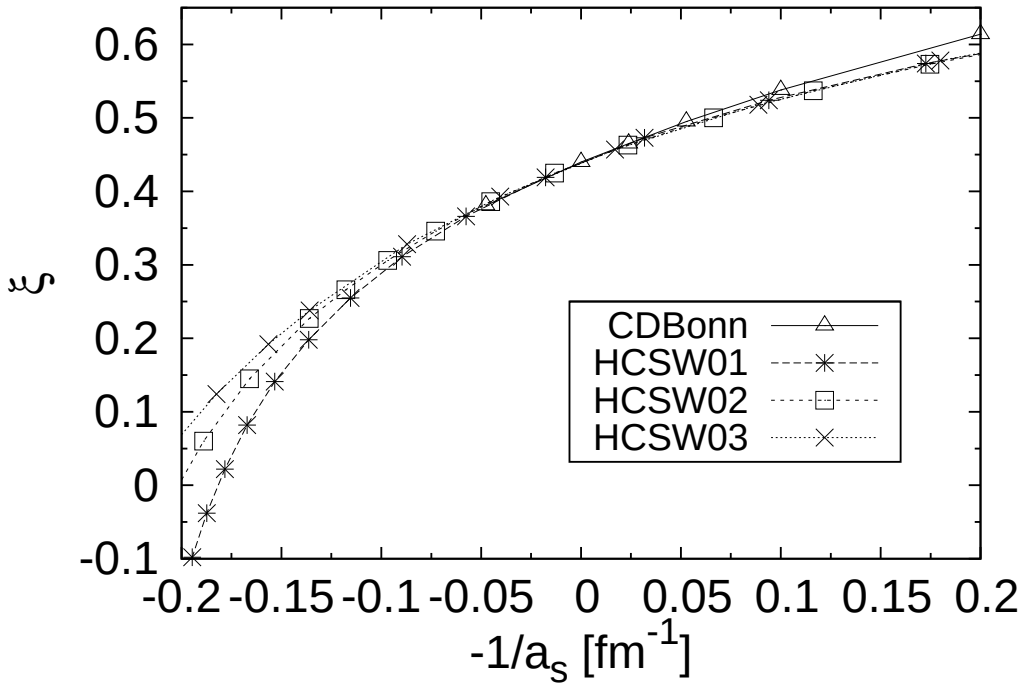

Figure 3.3: The ratio ξ obtained for potentials with different scattering lengths (including the infinity). The same nuclear medium density $k_F = 1.2$ fm^{-1} is applied.

is of interest to note that the MSHF results shown are remarkably close to the ring-diagram ones of Figure 3.1. This close agreement is an indication that the hole-hole correlation diagrams like diagram (c) of Figure 1.5 may not be important for pure neutron matter. The contribution from the particle-particle correlations like diagrams (a) and (b) are included in both ring diagram and MSHF calculations, but diagrams like (c) are included only in the former. It may be noted that in both Figure 3.1 and Figure 3.4 our results are nearly constant for k_F between 0.9 and 1.4 fm^{-1} (corresponding to density range 0.016 to 0.092 fm^{-3}). Outside this range, small variations of ξ start to appear. These variations are an indication that the methods we have employed for the calculation are not adequate for the high and very low density regions indicated above. So far we have employed only two-body interactions in the calculation. Three-body interactions have not been considered, and their effects may be

important.

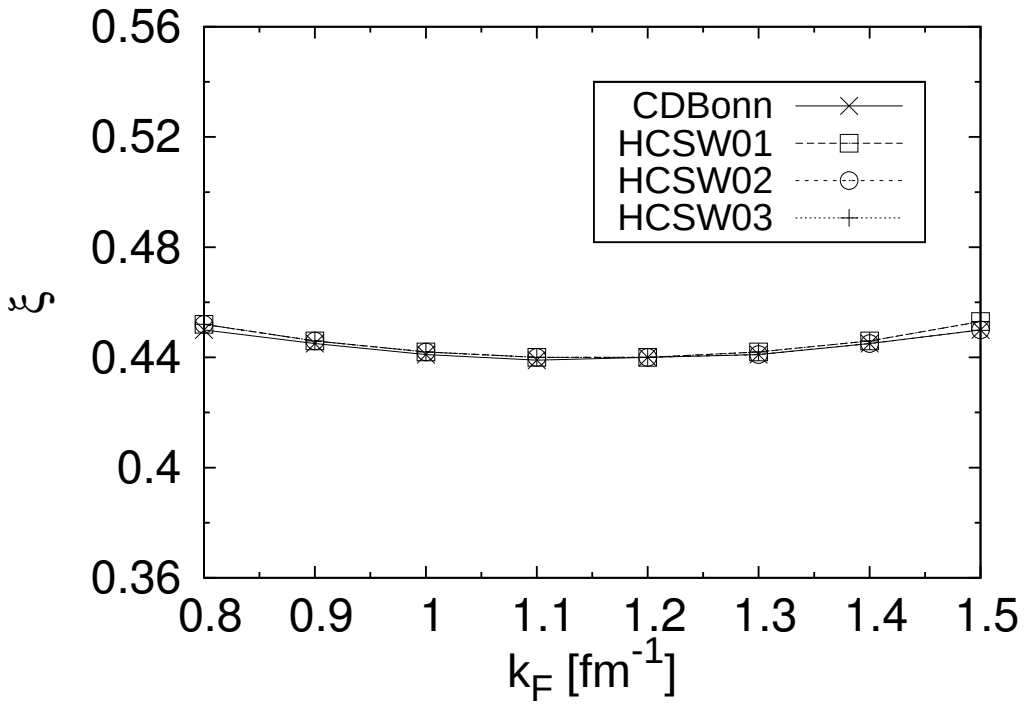

Figure 3.4: Universal ratio ξ for the cold neutron matter. Four unitarity potentials (three HCSW and one CDBonn) are used in the MSHF scheme.

In the MSHF method, the ratio ξ is calculated from the model-space effective interaction $V_{low-k}^{k_F}$. We have seen from Figure 3.4 that the ratios ξ given by the four different potentials are nearly the same. Does this mean that their $V_{low-k}^{k_F}$ are also nearly the same? In Figure 3.5 the matrix elements of this interaction for four different unitarity potentials are presented. As seen, they are clearly not identical to each other; there are significant differences among them. Equation (3.9) is in fact a strong constraint for the above interactions. To have ξ being a universal constant, the left-hand side of Equation (3.9) is proportional to k_F^2. Consequently the integral in the right-hand side must be equal to $C \times k_F^2$, C being a constant, noting that its integrand and integration limit are both dependent on k_F. This implies that at the unitary limit the $V_{low-k}^{k_F}$ interaction must satisfy certain stringent requirements so as to satisfy the above constraint.

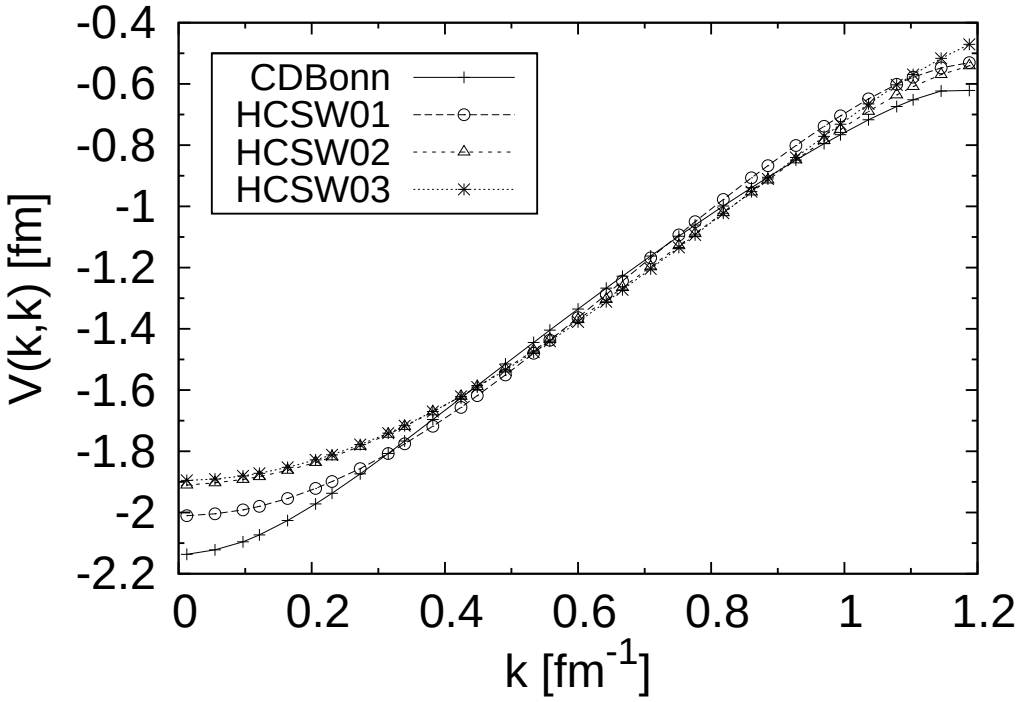

Figure 3.5: The diagonal matrix elements $V_{low-k}^{k_F}(k,k)$ of the four original unitarity potentials (three HCSW and one CDBonn). The same decimation cutoff $\Lambda = k_F = 1.2\text{fm}^{-1}$ is used.

Similar to the effective interactions commonly used in effective field theories [110, 111], we have found that our $V_{low-k}^{k_F}$ interactions can be highly accurately simulated by low-order momentum expansions of the form

$$\langle k|V_{low-k}^{k_F}|k\rangle = V_0 + V_2(\frac{k}{k_F})^2 + V_4(\frac{k}{k_F})^4, \tag{3.14}$$

where V_0, V_2 and V_4 are constants (independent of k but dependent on k_F). (The rms deviations for fitting the results of Figure 3.5 by the above expansion are 2×10^{-2} and 2×10^{-3} respectively for the CDBonn and HCSW cases, the fitting being very good.) In terms of these constants, Equation (3.9) assumes a rather simple form, namely

$$\frac{3\pi}{10}(\xi-1) = k_F(\frac{V_0}{3} + \frac{V_2}{10} + \frac{3V_4}{70}). \tag{3.15}$$

The above is an interesting sum-rule and scaling constraint, namely that at the unitary limit the strength sum $(V_0/3 + V_2/2 + 3V_4/70)$ is a constant for any k_F (density) and, in addition, it scales with $1/k_F$ (i.e. proportional to $1/k_F$). In Table 3.2 we present some sample results, to check how well they satisfy the above constraint. As seen our results satisfy this constraint very well. For each k_F, the values of the above sum given by the four different unitarity potentials are all quite close to each other. The values of this sum for different k_F are different but they are all giving ξ close to 0.44, in close agreement with the $1/k_F$ scaling.

Table 3.2: Low-order momentum expansion of $V_{low-k}^{k_F}$. Listed are the coefficients V_0, V_2 and V_4 of Equation (3.14), with the sum $(V_0/3 + V_2/10 + 3V_4/70)$ denoted as Sum. Four unitarity potentials are used.

V_{NN}	k_F [fm^{-1}]	V_0[fm]	V_2[fm]	V_4[fm]	Sum	ξ
CDBonn	1.2	-2.053	3.169	-1.801	-0.445	0.434
HCSW01		-2.001	2.865	-1.402	-0.441	0.439
HCSW02		-1.904	2.373	-0.999	-0.440	0.440
HCSW03		-1.893	2.261	-0.825	-0.440	0.439
HCSW01	1.0	-2.102	2.202	-1.070	-0.526	0.442
HCSW01	1.4	-1.945	3.584	-1.983	-0.375	0.443

The best numeric estimates of the ratio ξ by far have been obtained from the variational quantum-Monte-Carlo (QMC) calculations (see e.g. [106] and references quoted therein). It would be useful and of interest to compare our ring-diagram and MSHF calculations with the QMC ones. Let us first mention some differences between them. First, the method for 'taming' the strong short-range repulsion in V_{NN} used in our calculations is different from the one used in QMC. The superfluid-QMC calculation is based on the variation principle $\delta[\langle\Phi_{BCS}|\Psi_J^\dagger H\Psi_J|\Phi_{BCS}\rangle/\langle\Phi_{BCS}|\Psi_J^\dagger\Psi_J|\Phi_{BCS}\rangle] = 0$, where Φ_{BCS} is a BCS-paired trial wave function of definite number of particles and Ψ_J is a r-space Jastrow correlator for taming V_{NN} [106]. We do not use Ψ_J to tame the NN interaction; instead we employ a k-space RG method (see section 1.3) to renormalize V_{NN} into a smooth effective potential V_{low-k}. There is also the difference concerning the treatment of pairing in the two approaches. In superfluid-QMC, pairing is incorporated by using a BCS-paired trial wave

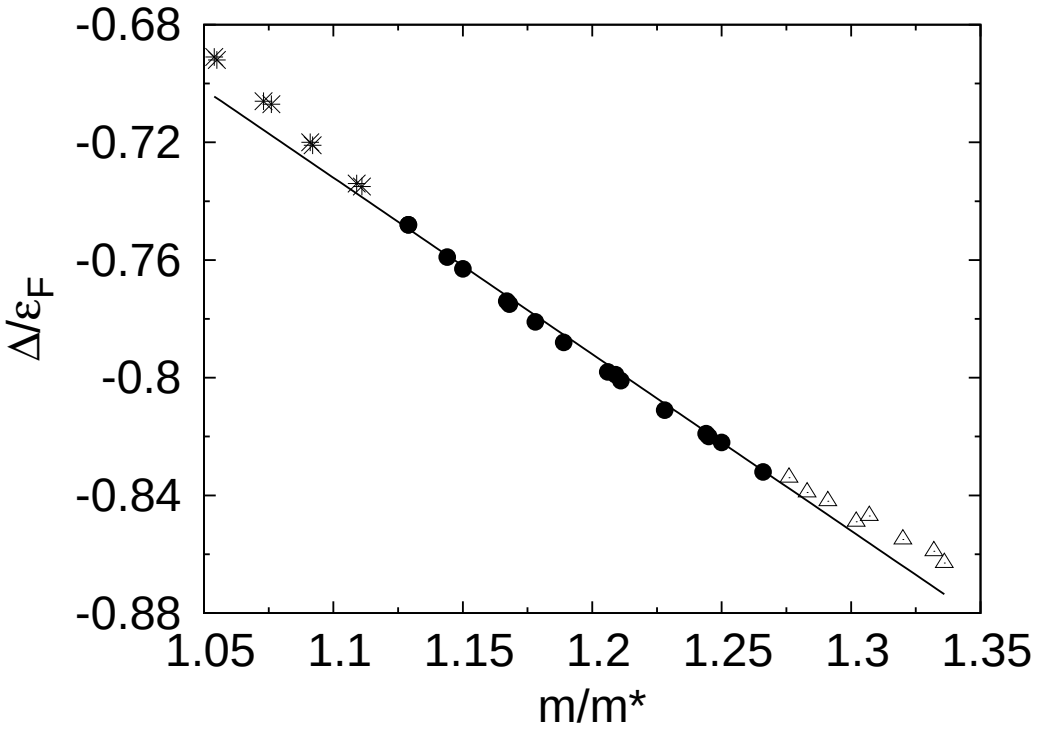

Figure 3.6: MSHF effective mass m^* and well depth Δ at the unitary limit. Results calculated from the unitarity potentials are denoted by 'star', 'dot' and 'triangle' respectively for k_F in the ranges (0.8-0.9), (0.9-1.4) and (1.4-1.5) fm^{-1}. The solid line represents the linear expression Equation (3.12) with ξ=0.44. See text for other explanations.

function. As discussed in section 1.4, we emphasize pairing by including only the boson-forming ring diagrams to all orders (both forward and backward ladder diagrams for a pair of fermions interacting any number of times), and in this way our all-order ring-diagram calculation treats the system as a collection of quasi bosons. Despite these differences, it is encouraging that our result of $\xi \simeq 0.44$ is satisfactorily close to the superfluid-QMC value of ~ 0.40 to ~ 0.44 [56, 106]. It may be pointed out that when we include only the first order ring diagram, our ring-diagram calculation reduces to the usual HF calculation. For $\Lambda = 2.1 fm^{-1}$ and $k_F = 0.8 fm^{-1}$ we have carried out HF calculations (i.e. including only the 1st-order ring diagram) and obtained $\xi_{HF} \simeq 0.55$, for all the four unitarity potentials mentioned earlier. This ξ_{HF} is significantly larger

than the corresponding all-order-ring result of 0.44. Normal-QMC calculations (where the trial wave function is a closed Fermi sea) have given $\xi \simeq 0.54$ [95, 106]. We believe that our 1st-order ring calculation is similar to that of the normal-QMC while our all-order ring-diagram one is similar to that of the superfluid-QMC (where the trial wave function is Φ_{BCS}).

We have discussed in section 3.3 that at the unitary limit the MSHF s.p. potential has a special property, namely its effective mass m^* and well depth Δ satisfy a linear constraint dependent on the unitary ratio ξ (see Equation (3.13)). Here this constraint is obeyed by our results. Similarly, we have calculated m/m^* and Δ/ε_F using the CDBonn and HCSW unitarity potentials using a wide range of k_F from 0.8 to 1.5 fm^{-1}. Our results are plotted in Figure 3.6, and as seen most of our data are located near the straight line corresponding to ξ=0.44. In the figure, the results for k_F in the range of (0.9-1.4)fm^{-1} are quite close to the ξ=0.44 straight line. For k_F outside this range, they are slightly off the line, which is consistent with the results of Figure 3.4.

It is promising that at the unitary limit the above MSHF framework has given rather satisfactory results for the ratio ξ ($\sim$ 0.44), in close agreement with both the superfluid-QMC results [56, 106] and those from our all-order ring diagram calculations. In addition, this method is fairly simple and transparent; as indicated by Equation (3.9), ξ is given by a simple integral and the HF potentials at the unitary limit satisfy the constraint of Equation (3.14). It may be mentioned, however, that this MSHF is only a limited effective theory; it is the $\Lambda = k_F$ limit of the ring-diagram formalism. In this limit the model space is one dimensional, and the model-space ground-state wave function is $|k_F\rangle$, the closed Fermi sea. The BCS pairing gap Δ_{BCS} is an important quantity, but this information is not contained in the MSHF effective theory. Δ_{BCS} is the lower bound for the lowest excitation energy of the many-body system. MSHF, however, is a one-dimensional effective theory which can describe only the ground state of the system; it provides no information about excited states. The effective MSHF theory is not capable to provide information about Δ_{BCS}, even though the MSHF wave function $|k_F\rangle$ is completely ($\boldsymbol{k}\uparrow, -\boldsymbol{k}\downarrow$) paired. To calculate Δ_{BCS}, one may need to employ the number-nonconserving Green's function framework [112, 113] which has been commonly used in supercon-

ductivity (superfluidity) calculations. (The Green's function method is based on a number-conserving formalism, and is not suitable for calculating Δ_{BCS}.) Using several Skyrme effective interactions, Su. *et al.* [113] have performed such number-nonconserving BCS calculations for nuclear matter.

3.5 Conclusion

Using several different unitarity potentials, defined as having infinite (very large) scattering length a_s, we have calculated the ground-state energy ratio $\xi \equiv E_0/E_0^{free}$ for neutron matter over a wide range of densities. A main purpose of our study was to check if the ratio so obtained is 'universal' in the sense that they have a common value (or nearly so), independent of the details of the potentials as long as they have $a_s \to \pm\infty$. We have used four unitarity potentials: One is the unitarity CDBonn potential whose meson exchange parameters are slightly tuned so that its a_s becomes very large (-12070 fm). The other three are square-well 'box' potentials with both hard-core repulsion and exterior attraction. The a_s of these box potentials can be obtained analytically, making it easy to construct many unitarity box potentials of different ranges and depths.

We have calculated ξ using two methods: a ring-diagram method and a model-space Hartree-Fock (MSHF) method. An important step in both methods is the transformation of the unitarity potentials, which have strong short-range repulsions, into low-momentum interactions V_{low-k} which are smooth potentials, convenient for many-body calculations. The transformation is carried out using a RG method which preserves low-energy phase shifts and the scattering length. We have found that the ratios ξ given by the ring-diagram and MSHF methods are practically identical over a wide range of densities (from ~ 0.02 to ~ 0.09 fm^{-3}). This is an indication that the *pphh* correlations (as shown by diagram (c) of Figure 1.5) are not important for neutron matter. Such correlations are included in the ring-diagram method but not in MSHF. The effect of the particle-particle ladder correlations (as shown by diagram (b) of Figure 1.5) are included in both. The MSHF method is considerably simpler than the ring-diagram one. It may provide a promising method for neutron

matter. Further study of this method for neutron matter may be useful and of interest.

The CDBonn and the three box unitarity potentials are very different from each other, but the ratios ξ predicted by them using either of the above methods are all remarkably close to 0.44, over a wide range of densities. This is indeed a rather interesting and surprising result, indicating that ξ may be perceived as a universal constant. For the MSHF case, this result is related to some special properties of the V_{low-k} interaction at the unitary limit. We have found that the V_{low-k} interaction for MSHF can be accurately simulated by a low-order momentum expansion of the form $[V_0 + V_2(k/k_F)^2 + V_4(k/k_F)^4]$, and at the unitary limit the strength sum $(V_0/3 + V_2/10 + 3V_4/70)$ calculated from the above potentials satisfies the constraint of Equation (3.14) very well, for a wide range of k_F. It is also found that at the unitary limit the parameters m^* and Δ of the MSHF mean field potentials given by the above potentials all obey a linear constraint satisfactorily. In conclusion, we believe that our results provide strong numerical support to the conjecture that the ratio ξ is universal.

Chapter 4

Nuclear Symmetry Energy

4.1 Introduction

The nuclear matter symmetry energy is an important as well as very interesting subject in nuclear and astro-nuclear physics. As reviewed extensively in the literature [5–9, 114–118], it plays a crucial role in determining many important nuclear properties, such as the neutron skin of nuclear systems, structure of nuclei near the drip line, and neutron stars' masses and radii. It is especially of importance that constraints on the nuclear matter equation of state (EoS) [6] and the density dependence of the symmetry energy $E_{sym}(n)$ [8, 9] up to $n \simeq 5n_0$ have been experimentally extracted from HIC experiments, n_0 being the saturation density of symmetric nuclear matter. There have been a large number of theoretical derivations of $E_{sym}(n)$ using, for example, the BHF [119–121], DBHF [117, 122–124], variational [125], relativistic mean field [126] and Skyrme HF [127] many-body methods. The results of these theoretical investigations have exhibited, however, large variations for $E_{sym}(n)$. Depending on the interactions and many-body methods used, they can give either a 'hard' $E_{sym}(n)$, in the sense that it increases monotonically with n, or a 'soft' one where $E_{sym}(n)$ arises to a maximum value at $n \simeq 1.5n_0$ and then descends to zero at $\sim 3n_0$ [7, 118]. It appears that the predicted behavior of $E_{sym}(n)$ may depend importantly on the NN interactions and the many-body methods employed.

In this chapter, we shall calculate the nuclear symmetry energy using the low-momentum interaction V_{low-k} derived from realistic NN interactions V_{NN} using a RG approach as discussed in section 1.3. To our knowledge, this method has not yet been applied to the study of E_{sym}.

We shall first calculate the EoS $E(n, \alpha)$ for asymmetric nuclear matter, from which $E_{sym}(n)$ can be obtained. Here E is the ground-state energy per nucleon and n is the total baryon density. α is the isospin asymmetry parameter defined as $\alpha = (n_n - n_p)/n$, where n_n and n_p denote, respectively, the neutron and proton density and $n = n_n + n_p$. Our EoS will be calculated using a ring-diagram many-body method [44, 45, 58]. As discussed in section 1.4, this method includes the *pphh* ring diagrams to all orders. In comparison, only the diagrams with two hole lines are included in the familiar HF, BHF and DBHF calculations. In other words, in these HF methods a closed Fermi sea is employed while in the ring-diagram framework the effects from the fluctuations of the Fermi sea are taken into account by including the *pphh* ring diagrams to all orders.

The nuclear symmetry energy $E_{sym}(n)$ is related to the asymmetric nuclear matter EoS by

$$E(n, \alpha) = E(n, \alpha = 0) + E_{sym}(n)\alpha^2 + O(\alpha^4), \tag{4.1}$$

The contributions from terms of higher order than α^2 are usually negligibly small, as illustrated by our following results. With such contributions neglected, we have

$$E_{sym}(n) = E(n, 1) - E(n, 0). \tag{4.2}$$

Then the nuclear symmetry energy is just given by the energy difference between neutron and symmetric nuclear matter. In calculating $E_{sym}(n)$, the above EoS clearly play an important role. In our calculation, we shall require that the NN interaction and many-body methods employed should give satisfactory results for $E(n, 1)$ and $E(n, 0)$ of, respectively, neutron and symmetric nuclear matter. The use of V_{low-k} alone, however, has not been able to reproduce the empirical nuclear saturation properties, the predicted saturation density and binding energy per particle being both too large compared to the

empirical values of $n_0 \simeq 0.16\text{fm}^{-3}$ and $E \simeq -16\text{MeV}$ for symmetric nuclear matter [44, 58]. To improve the situation, it may be necessary to include the effects from BR scaling [20, 67, 72] for the in-medium mesons, or three-body forces [71]. BR scaling is suitable only for the low density region; it suggests that the masses of light mesons in medium are reduced 'linearly' with the density. We consider here the EoS up to $\sim 5n_0$ and at such high density the linear BR scaling is clearly not applicable. In this chapter we shall adopt the nonlinear BRE scaling [129] for the in-medium mesons and apply it to our $E_{sym}(n)$ calculations. The effects from the linear BR and nonlinear BRE scalings on the nuclear EoS and symmetry energy will be studied.

The organization of this chapter is as follows. We shall first briefly describe details about the calculation of the EoS for asymmetric nuclear matter from low-momentum NN interactions with the *pphh* ring diagrams summed to all orders. The BRE scaling is a nonlinear extension of linear BR scaling. The difference between them will be addressed. Then the results will be presented and discussed. A summary and conclusion is contained at the end of this chapter.

4.2 Formalisms

We use a ring-diagram method [44, 58] to calculate the nuclear matter EoS. In this method, the ground-state energy is expressed as $E(n,\alpha) = E^{free}(n,\alpha) + \Delta E(n,\alpha)$ where E^{free} denotes the free (non-interacting) EoS and ΔE is the energy shift due to the NN interaction. In our ring-diagram approach, it is given by the all-order sum of the *pphh* ring diagrams as illustrated in Figure 4.1. Note that we include three types of ring diagrams, the proton-proton, neutron-neutron and proton-neutron ones. The proton and neutron Fermi momenta are, respectively, $k_{Fp} = (3\pi^2 n_p)^{1/3}$ and $k_{Fn} = (3\pi^2 n_n)^{1/3}$. With such ring diagrams summed to all orders, we can calculate $\Delta E(n,\alpha)$ with Equation (1.6) as discussed in section 1.4.

It is well known that the use of the free-space V_{NN} alone is not adequate for describing nuclear properties at high densities. To satisfactorily describe such properties, one may need to include the three-body forces [71] or the in-medium

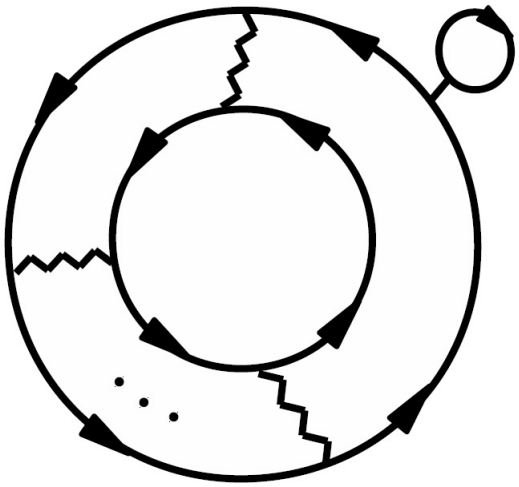

Figure 4.1: Sample ring diagram included in the equation of state $E(n, \alpha)$. Each wave line represents a V_{low-k} vertex. The HF one-bubble insertions to the Fermion lines are included to all orders.

modifications to the nuclear interaction. In this chapter, we shall employ in our EoS calculations nuclear interactions which contain the in-medium modifications suggested by the BR and BRE [129] scalings. These scalings are based on the relation [18, 20, 72] that hadron masses scale with the quark condensate $\langle \bar{q}q \rangle$ in medium as

$$\frac{m^*}{m} = \left(\frac{\langle \bar{q}q(n) \rangle}{\langle \bar{q}q(0) \rangle} \right)^{1/3}, \tag{4.3}$$

where m^* is the hadron mass in a medium of density n, and m is that in free space. The quark condensate $\langle \bar{q}q \rangle$ measures the chiral symmetry breaking, and its density dependence in the low-density limit is related [19, 130] to the free πN sigma term $\Sigma_{\pi N}$ by

$$\frac{\langle \bar{q}q(n) \rangle}{\langle \bar{q}q(0) \rangle} = 1 - \frac{n \Sigma_{\pi N}}{f_\pi^2 m_\pi^2}, \tag{4.4}$$

where $f_\pi = 93$MeV is the pion decay constant and $\Sigma_{\pi N} = 45 \pm 7$MeV [131]. Applying the above scaling to mesons in low-density nuclear medium, one has the linear scaling Equation (2.3), which will be referred to as the linear BR scaling.

In this chapter, we are interested in the EoS and E_{sym} up to densities as high as $n \simeq 5n_0$, and at such high densities the linear BR scaling is clearly not suitable. How to scale the mesons in such high density region is still by and large uncertain. We shall adopt here the BRE scaling which is an extension of the BR scaling. In this scaling, a new relation for the quark condensate $\langle \bar{q}q \rangle$ based on chiral symmetry breaking is employed [129], namely

$$\frac{\langle \bar{q}q(n) \rangle}{\langle \bar{q}q(0) \rangle} = \frac{1}{1 + \frac{n\Sigma_{\pi N}}{f_\pi^2 m_\pi^2}}. \tag{4.5}$$

Note that this relation agrees with the linear scaling relation of Equation (4.4) for small n. The above scaling suggests a non-linear scaling for meson mass

$$\frac{m^*}{m} = \left(\frac{1}{1 + D\frac{n}{n_0}} \right)^{1/3}. \tag{4.6}$$

with $D = \frac{n_0 \Sigma_{\pi N}}{f_\pi^2 m_\pi^2}$, and we shall refer to this scaling as the nonlinear BRE scaling. Using the empirical values for ($\Sigma_{\pi N}$, n_0, f_π, m_π), we have D= 0.35±0.06. We shall employ the one-boson exchange BonnA potential [13] with its mesons (ρ, ω, σ) scaled using both the linear (Equation (2.3)) and nonlinear (Equation (4.6)) scalings. This potential is chosen because it has a relatively simple structure which is convenient for scaling its meson parameters.

4.3 Results and Discussions

Using both the unscaled and scaled BonnA potentials, we first calculate the ring-diagram EoS for symmetric nuclear matter to investigate if they can give saturation properties in good agreement with the empirical values. We employ the low-momentum interactions V_{low-k} from these potentials using a decimation $\Lambda = 3.0\text{fm}^{-1}$, which is chosen because we are to study the EoS up to high densities of $\sim 5n_0$. As shown in Figure 4.2, the EoS (labelled 'V_{low-k} alone') calculated with the unscaled potential saturates at $k_F \simeq 1.8\text{fm}^{-1}$, which is too large compared with the empirical value, and it also overbinds nuclear matter. We then repeat the calculation including the medium modifications

from the BR scalings. For the linear BR scaling (Equation (2.3)), we have used $C_\rho = 0.113, C_\omega = 0.128$ and $C_\sigma = 0.102$. These parameters are chosen so as to have satisfactory saturation properties, namely they give $E_0/A \simeq$-15.3 MeV and $n_0 \simeq 0.16$ fm^{-3}. In Figure 4.2 we also present our results obtained with the nonlinear BRE scaling (Equation (4.6)) using parameters $D_\omega = D_\rho$=0.40 and D_σ=0.30. They were chosen to provide satisfactory results for E_0/A and n_0. It is of interest that for densities (n $\lesssim n_0$) the EoS given by the linear BR and nonlinear BRE scalings are practically equivalent to each other.

As also seen from Figure 4.2, the above equivalence begins to disappear for densities larger than n_0. There the EoS given by the linear scaling is much stiffer than that given by the nonlinear one; the difference between them becomes larger and larger as density increases. In addition to the above two EoS, we have also calculated an EoS using the interaction given by the sum of the unscaled V_{low-k} and the empirical Skyrme three-body forces. The well-known empirical Skyrme force [77] is the form of Equation (2.4) For nucleons in a nuclear medium of density n, this three-body force become a density-dependent two-body force commonly written as

$$V_n(i,j) = \frac{t_3}{6} n \delta(\boldsymbol{r}_i - \boldsymbol{r}_j). \tag{4.7}$$

In Figure 4.2 the EoS labeled 'V_{low-k} with TNF' is obtained using the combined interaction of V_{low-k} (unscaled) and V_n of Equation (4.2). The parameter t_3 is adjusted so that the resulting EoS gives satisfactory saturation properties for symmetric nuclear matter. The EoS shown has $t_3 = 2000\text{MeV} \cdot \text{fm}^6$.

It is of interest that the above three EoS (linear BR and nonlinear BRE, TNF) are nearly identical for densities (n $\lesssim n_0$), but they deviate from each other with increasing densities. Without experimental guidelines about the nuclear matter EoS above n_0, it would be difficult to determine which of these three EoS has the correct high density behavior. Fortunately, HIC experiments conducted during the last several years have provided us with constraints of the EoS at high densities. Danielewicz *et al.* [6] have obtained a constraint on the EoS for symmetric nuclear matter of densities between $2n_0$ and $4.5n_0$, as shown by the red solid-line box in Figure 4.3. Comparing our three EoSs with

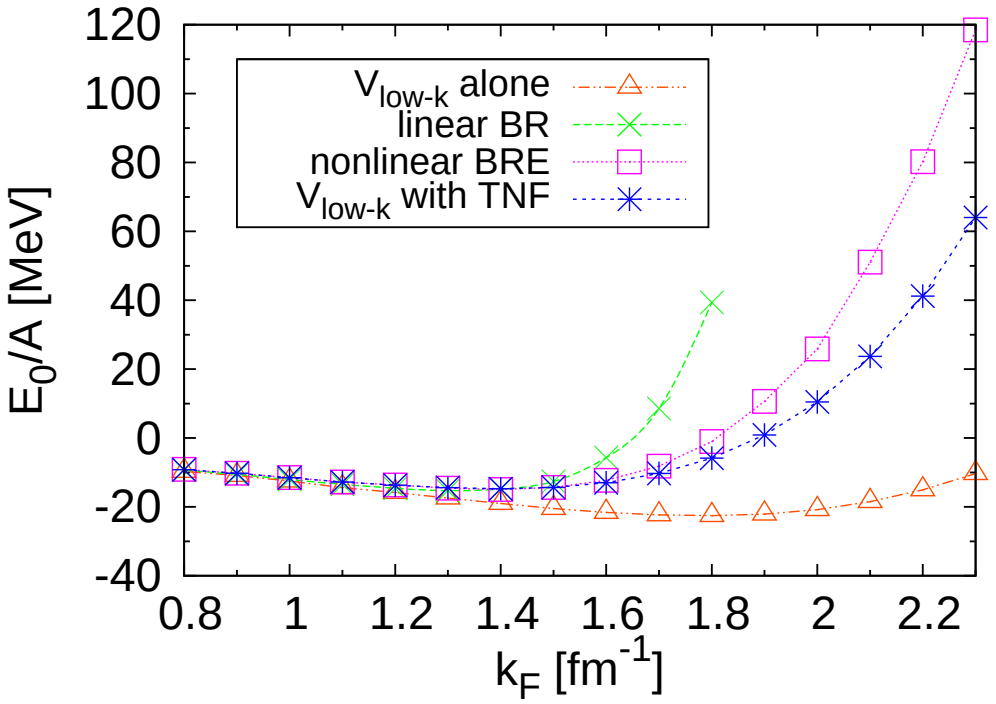

Figure 4.2: Ring-diagram EoSs calculated with the V_{low-k} interaction alone, with the linear BR scaling of Equation (2.3), with the nonlinear BRE scaling of Equation (4.6), and with the addition of a Skyrme-type three-body force (TNF).

their constraint, the linear BR EoS is clearly not consistent with the constraint and should be ruled out. This linear scaling is suitable for low densities, but definitely needs modification at high densities. It is primarily for this purpose that we have considered the nonlinear scaling. As displayed in Figure 4.3, the EoS with the nonlinear BRE scaling is in much better agreement with the constraint than the linear BR one. It satisfies the constraint well except being slightly above the constraint at densities near $4.5n_0$. It is of interest that the EoS using V_{low-k} with the Skyrme-type three-body forces exhibit even better agreement with the constraint.

So far we have studied the effects of the BR scalings and the three-body forces on the EoS for symmetric nuclear matter. The neutron matter EoS is also an interesting and important topic [78, 79]. It plays a crucial role in

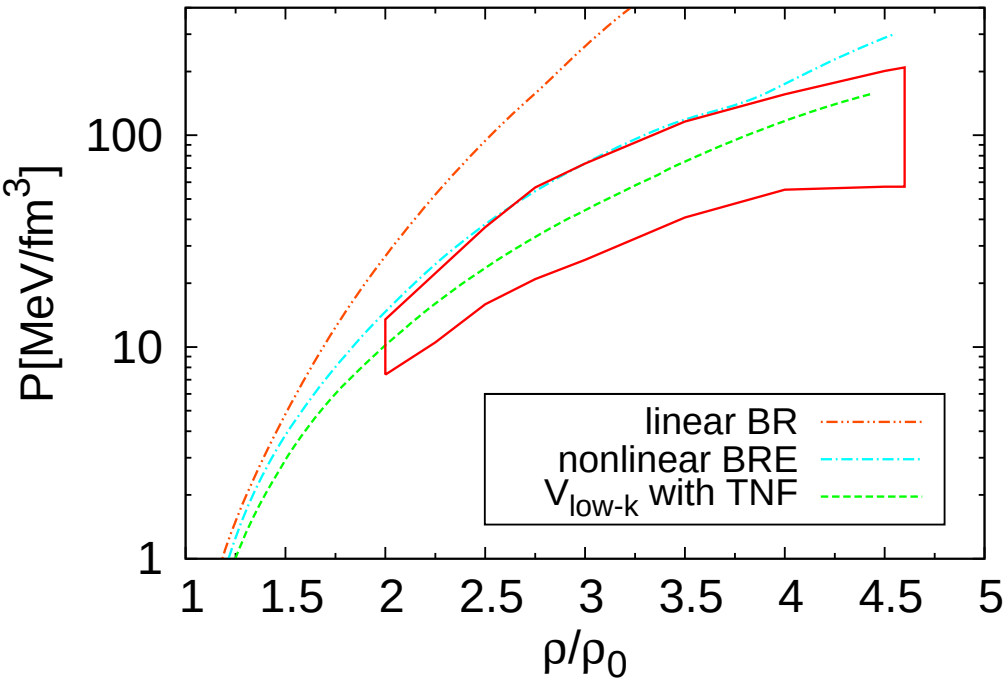

Figure 4.3: Comparison of the calculated equations of state for symmetric nuclear matter with the constraint (solid-line box) from HIC experiments.

determining the nuclear symmetry energies as well as the properties of neutron stars. It should be of interest to study also the effects of the above BR/BRE scalings and the three-body forces on the EoS of neutron matter. Using the same V_{low-k} ring-diagram framework employed for symmetric nuclear matter and the same parameters (C, D and t_3), we have calculated the neutron matter EoS up to $4.5n_0$. Our calculated neutron-matter EoS are displayed in Figure 4.4. Danielewicz *et al.* [6] have given two different constraints for the neutron matter EoS: a stiff one (upper black solid-line box) and a soft one (lower red solid-line box) which are both displayed in Figure 4.4. As we can see, the linear BR EoS is again producing too much pressure. The nonlinear BRE EoS agrees well with the stiff constraint (upper box) while the TNF EoS is fully within the soft constraint box. To further test these two EoS (nonlinear BRE and TNF), it would be very helpful to have narrower experimental constraints on the neutron matter EoS.

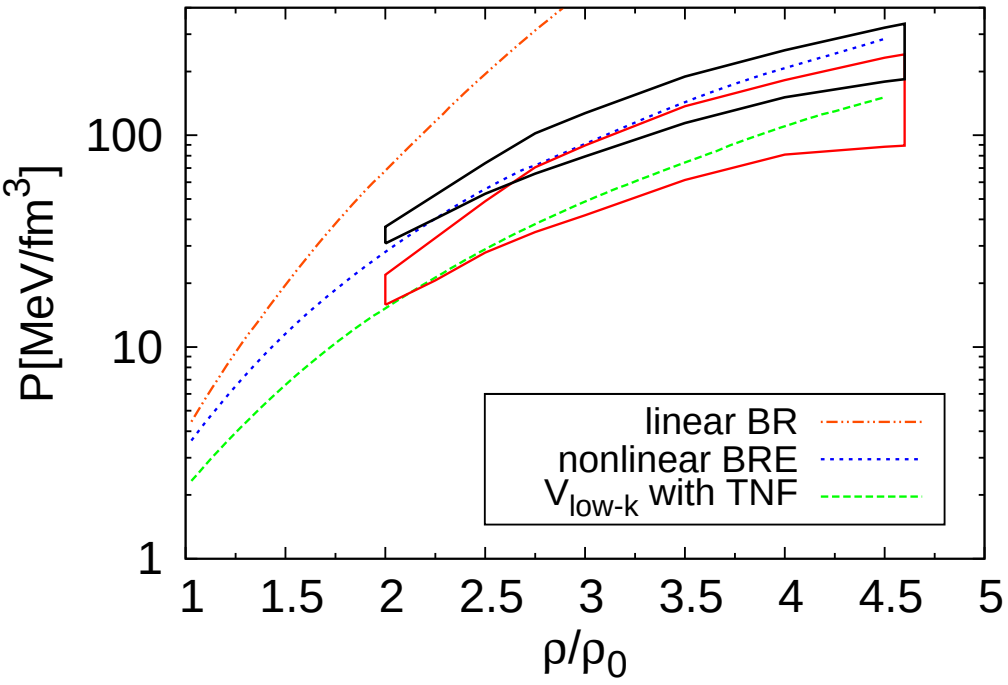

Figure 4.4: Comparison of the calculated equations of state for pure neutron-matter with the constraints from HIC experiments. See text for more explanations.

The symmetry energy E_{sym} is a topic of much current interest, and extensive studies have been carried out to extract its density dependence from heavy-ion collision experiments [8, 9]. Based on such experiments, Li *et al.* [8] suggested an empirical relation

$$E_{sym}(n) \approx 31.6(n/n_0)^{\gamma};\ \gamma = 0.69 - 1.1 \tag{4.8}$$

for constraining the density dependence of the symmetry energy. Also based on such experiments, Tsang *et al.* [9] recently proposed a new empirical relation for the symmetry energy, namely

$$E_{sym}(n) = \frac{C_{s,k}}{2}\left(\frac{n}{n_0}\right)^{2/3} + \frac{C_{s,p}}{2}\left(\frac{n}{n_0}\right)^{\gamma_i}, \tag{4.9}$$

where $C_{s,k} = 25\text{MeV}$, $C_{s,p} = 35.2\text{MeV}$ and $\gamma_i \approx 0.7$. It should be useful and of interest to check if our calculated $E_{sym}(n)$ is consistent with the above relations.

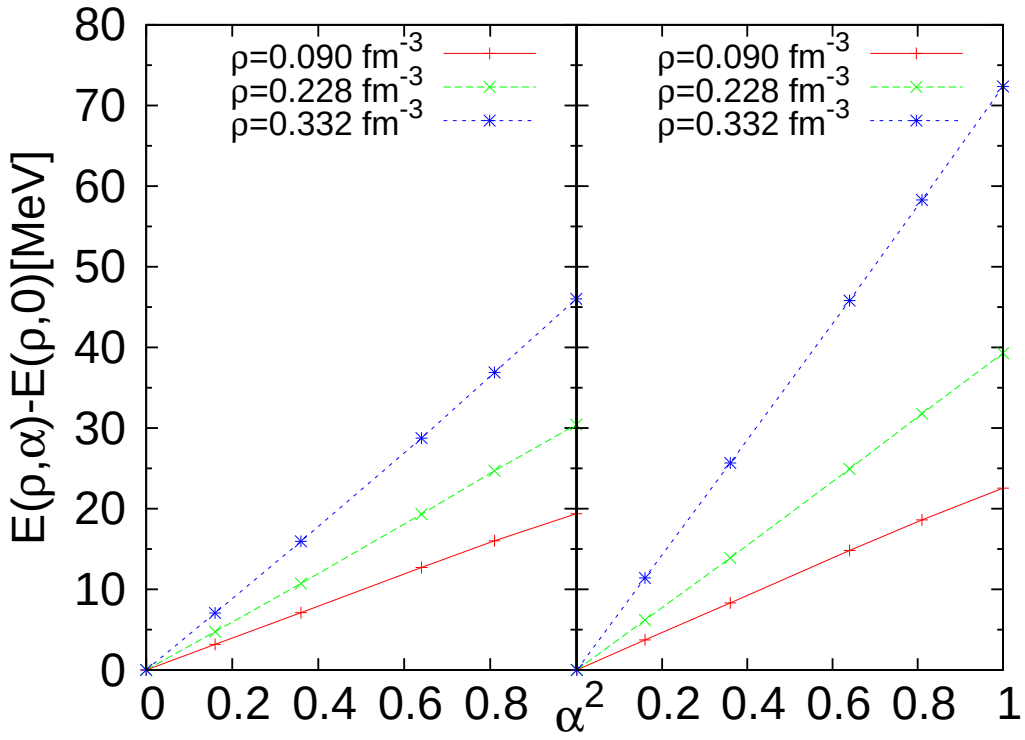

Figure 4.5: Ring-diagram equations of state for asymmetric nuclear matter. See text for more explanations.

Using the ring-diagram framework described earlier, we have calculated the ground-state energy $E(n, \alpha)$ for asymmetric nuclear matter. Some representative results are shown in Figure 4.5. The results in the left panel are obtained with the 'V_{low-k} with TNF' interaction while for the right panel the 'nonlinear BRE' interaction is used. As seen, $E(n, \alpha)$ varies with α^2 almost perfectly linearly, for a wide range of n. (Note that in Figure 4.5 we plot the energy difference $E_{sym}(n, \alpha) - E_{sym}(n, 0)$.) This is a desirable and remarkable result, indicating that our ring-diagram symmetry energy can be accurately obtained from the simple relation given by Equation (4.2), namely the energy difference between neutron and symmetric nuclear matter.

In Figure 4.6, the 'shaded area' represents the empirical constraint, Equa-

tion (4.8). As can be seen, there are large uncertainties in the high-density region. The empirical relation Equation (4.9) is given by the 'second curve from bottom' in the figure. As also seen in Figure 4.6, the density dependence of this relation is slightly below the softest limit (lower boundary of the shaded area) of Equation (4.8). Our 'nonlinear BRE' results are in the middle of the shaded area, in good agreement with the empirical constraint of [8]. Our results with the TNF force are below both empirical ones, giving a softer density dependence. It may be noticed that for densities ($n \lesssim n_0$), the calculated and empirical results are all in good agreement with each other. The symmetry energies given by them at n_0 are all close to ~ 30MeV, which is also the only well determined empirical value. Furthermore, our calculated symmetry energies all increase monotonically with density. We have required our nuclear matter EoS to satisfy certain empirical constraints, and with such requirements it may be difficult for our present calculations to have a soft $E_{sym}(n)$ as the supersoft one of [118] which saturates at density near $1.5n_0$.

We have found that our symmetry energies can be well fitted by expressions of the same forms as Equations (4.8 - 4.9), with the exponents γ and γ_i treated as parameters. In Table 4.1, we compare the exponents determined from our results with the empirical ones of [8, 9]. The γ exponent given by the nonlinear BRE scaling is in good agreement with the empirical values of [8]. The empirical γ_i of [9] is, however, about half-way between the γ_i obtained with 'nonlinear BRE' and that with 'TNF'.

Table 4.1: Comparison of the density exponents for the nuclear symmetry energy $E_{sym}(n)$. The exponents γ and γ_i are defined respectively in Equations (4.8- 4.9).

	γ	γ_i
Li *et al.*	0.69-1.1	
Tsang *et al.*		0.7
non-linear BRS	0.82	1.04
TNF	0.53	0.43

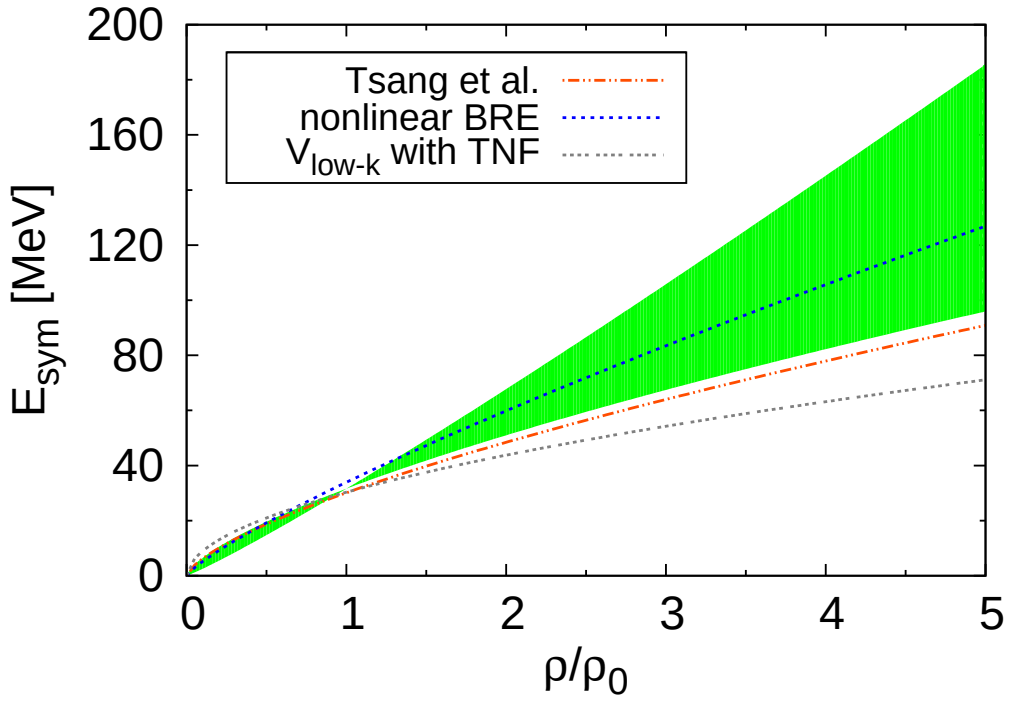

Figure 4.6: Comparison of the density dependence of our calculated nuclear symmetry energies with the empirical results of Tsang *el at.* (dot-dash line) and Li *el at.* (shaded area).

4.4 Conclusion

Employing the V_{low-k} low-momentum interactions, we have calculated the nuclear symmetry energy $E_{sym}(n)$ up to a density of $\sim 5n_0$ using a ring-diagram framework where *pphh* ring diagrams are summed to all orders. We first calculate the EoS for symmetric nuclear matter and neutron matter and compare our results with the corresponding empirical constraints of Danielewicz *et al.* [6]. To have satisfactory agreements with such constraints, we have found it necessary to include certain medium corrections to the free-space NN interations. In other words, the effective NN interactions in the medium are different from those in free space, and when using them in nuclear many-body problems it may be necessary to include the renormalization effects due to the presence of other nucleons. We have considered several methods to in-

corporate such medium corrections. Although the nuclear matter saturation properties can satisfactorily be reproduced by including the medium corrections from the well-known linear BR scaling for the in-medium mesons, this scaling produces an EoS which is too stiff compared with the experiment constraints. We have found that the EoS obtained with the nonlinear BRE scaling are in good agreement with the experiment constraints. We have considered another method to render the effective interaction density dependent, namely adding a Skyrme-type three-body forces to the unscaled V_{low-k} interaction. The EoS so obtained are also in good agreement with the experiment constraints, but the resulting neutron matter EoS is significantly softer than that with the nonlinear scaling. The three methods (linear and nonlinear scalings, and TNF) all have reproduced well the empirical saturation properties of nuclear matter ($n_0 \simeq 0.16\text{fm}^{-3}$ and $E_0/A \simeq -15\text{MeV}$), but their results at high densities are different. We have determined the scaling parameters C (linear BR scaling) and D (nonlinear BRE scaling) by fitting the above saturation properties. It is encouraging that the results, $(0.102 \lesssim C \lesssim 0.128)$ and $(0.30 \lesssim D \lesssim 0.40)$, so obtained are actually in good agreement with the theoretical result $D \simeq 0.35 \pm 0.06 \simeq 3C$ given by Equations (4.3 - 4.6).

Including the above medium modifications, we proceed to calculate the nuclear symmetry energies. We have found that the $E_{sym}(n, \alpha)$ given by our asymmetric ring-diagram calculations depends on α^2 almost perfectly linearly. This is a rather surprising and useful result, suggesting that the symmetry energy can be reliably obtained from the simple energy difference between symmetric nuclear matter and neutron matter. Our symmetry energies obtained with the nonlinear BRE scaling agree well with the empirical constraints of [8], and are slightly above the empirical values of [9]. Our results with the TNF force is slightly below the empirical results of both [8] and [9]. The nonlinear BRE scaling has given satisfactory results for the EoS of nuclear matter and nuclear symmetry energies up to a density of $5n_0$. We believe this scaling provides a suitable extension of the linear BR scaling to moderately high densities of $5n_0$. Our calculated $E_{sym}(n)$ all increase monotonically with n up to $\sim 5n_0$. It may be of interest to carry out further studies about the possibility of obtaining a supersoft symmetry energy which may saturate at

some low density of $\sim 1.5n_0$ [118].

Chapter 5

Shell Model Effective Interactions

5.1 Introduction

The nuclear shell model has provided a very successful framework for describing the properties of a wide range of nuclei. This framework is basically an effective theory [133–135], corresponding to reducing the full-space nuclear many-body problem to a model-space one with effective Hamiltonian $PH_{\rm eff}P{=}PH_0P + PV_{\rm eff}P$ where H_0 is the single-particle (s.p.) Hamiltonian and P represents the projection operator for the model space which is usually chosen to be a small shell-model space such as the *sd* shell outside an ^{16}O closed core. The effective interaction $V_{\rm eff}$ plays a central role in this nuclear shell model approach, and its choice and/or determination have been extensively studied, see e.g. [134–137]. As discussed in these references, $V_{\rm eff}$ may be determined using either an empirical approach where it is required to reproduce selected experimental data or a microscopic one where $V_{\rm eff}$ is derived from realistic NN interactions using many-body methods. The folded-diagram theory [133–135] is a commonly used such method for the latter. Briefly speaking, in this theory $V_{\rm eff}$ is given as a folded-diagram series [133–135, 138]

$$V_{\rm eff} = \hat{Q} - \hat{Q}' \int \hat{Q} + \hat{Q}' \int \hat{Q} \int \hat{Q} - \hat{Q}' \int \hat{Q} \int \hat{Q} \int \hat{Q} \cdots , \qquad (5.1)$$

where $\hat{Q}$ represents a so-called $\hat{Q}$-box, which may be written as

$$\hat{Q}(\omega) = [PVP + PVQ\frac{1}{\omega - QHQ}QVP]_L. \tag{5.2}$$

Here V represents the NN interaction and ω is the so-called starting energy which will be explained later. Thus from the NN interaction V we can in principle calculate the $\hat{Q}$-box and thereby the effective interaction V_{eff}. Note that we use Q, without hat, to denote the Q-space projection operator. ($P + Q = 1$) Note also that the $\hat{Q}$-box is an irreducible vertex function where the intermediate states between any two vertices must belong to the Q space. As indicated by the subscript L in Equation (5.2), $\hat{Q}$-box contains valence linked diagrams only, such as the 1st- and 2nd-order $\hat{Q}$-box diagrams for ^{18}O and ^{18}F shown in Figure 5.1. The $\hat{Q}'$-box of Equation (5.1) is defined as $(\hat{Q} - PVP)$, namely $\hat{Q}'$ begins with diagrams 2nd-order in V. The above folded-diagram formalism has been employed in microscopic derivations of shell model effective interactions for a wide range of nuclei [134, 135].

In the chapter we would like to consider two extensions for the above formalism and carry out calculations to study the effects of them. Our first extension concerns the methods employed for the calculation of the folded-diagram series as indicated by Equation (5.1). The well-known Lee-Suzuki (LS) [139–141] iteration has been commonly used in previous microscopic calculations of shell model effective interactions [134, 135]. Here we would like to employ two different methods, the Krenciglowa-Kuo (KK) iteration method [142, 143] and the newly developed extended Krenciglowa-Kuo iteration method of Okamoto, Suzuki, Kumagai and Fujii (EKKO)[57], for this calculation. As we shall discuss later, it is not convenient to use the LS method for calculating the effective interactions for non-degenerate large model spaces such as the *sdpf* two-shell one, while both the EKKO and the KK methods can be conveniently applied in this situation. The EKKO method has an additional advantage. When the P- and Q-space are not adequately separated from each other, the $\hat{Q}$-box employed in the KK method may have singularities, causing difficulty for its iterative solution. An essential and interesting difference between the EKKO and KK methods is that the EKKO method employs the vertex function $\hat{Z}$-box

while in the latter the vertex function $\hat{Q}$-box is used. This simple replacement (of $\hat{Q}$ by $\hat{Z}$) has an important advantage in circumventing the singularities mentioned above. We believe that both the EKKO and KK methods may provide a promising framework for calculating shell-model effective interactions for large model spaces (such as *sdpf* one) which may be needed for describing exotic nuclei with large neutron excess.

Another extension considered in this chapter is about the inclusion of the three-body force V_{3N} in microscopic calculations of the shell-model effective interactions. Up to now most microscopic effective interaction calculations have been based on the two-body interaction V_{2N} alone [134, 135]. The need of V_{3N} in nuclear many-body problems has long been recognized. The use of V_{2N} alone has been inadequate in reproducing the empirical nuclear matter saturation properties (see e.g. [44, 58] and references quoted therein). The inclusion of V_{3N} has been of essential importance in describing the binding energies and low-lying spectra of light nuclei [23, 144, 145] and in explaining the long half-life of the $^{14}C-^{14}N$ β-decay [146]. Otsuka *et al.* [147] have shown that the inclusion of V_{3N} plays a crucial role in describing the oxygen isotopes near the drip line. In this chapter we shall calculate both the degenerate *sd* and the non-degenerate *sdpf* shell-model $V_{\rm eff}$ using the chiral N^{3}LO two-body interaction [148] together with the lowest-order density dependent chiral three-body force of Holt, Kaiser and Weise [146, 149]. The LS, KK and EKKO iteration methods will all be employed for the degenerate case, while using only the latter two for the non-degenerate situation.

The organization of the chapter is as follows. At the beginning we shall describe a non-degenerate version of the EKKO method [57] and how we apply it and the KK method [142, 143] to shell-model effective interactions. A comparison of these two methods with the LS one [139, 140] will be made. In addition to the two-body force V_{2N}, we shall include also in our calculations an effective density dependent force which is extracted from the lowest-order chiral three-body force [146, 149, 150], and this inclusion will also be briefly described there. Our results will be presented and discussed. We shall first perform a sequence of model calculations comparing the EKKO, KK and LS iteration methods for both degenerate and non-degenerate model spaces. Be-

fore presenting our results of shell model calculations, we shall first carry out ring-diagram calculations for symmetric nuclear matter including both V_{2N} and V_{3N}, with the parameters c_D and c_E of the three-body force V_{3N} [146, 149] determined by requiring that such nuclear matter calculations reproduce satisfactorily empirical nuclear matter saturation properties. Using the V_{3N} so determined, we shall then calculate shell-model effective interactions with the NN interaction given by (V_{2N}+V_{3N}) and study the effects of V_{3N}. The LS, KK and EKKO methods will all be used to calculate the degenerate *sd* effective interactions, to check if the results given by the commonly used LS method agree with the KK and EKKO ones. The KK and EKKO methods will be employed to calculate the non-degenerate *sdpf* effective interactions. The influence of V_{3N} on the low-lying states of ^{18}O and ^{18}F will be discussed. A summary and conclusion will be presented at the end.

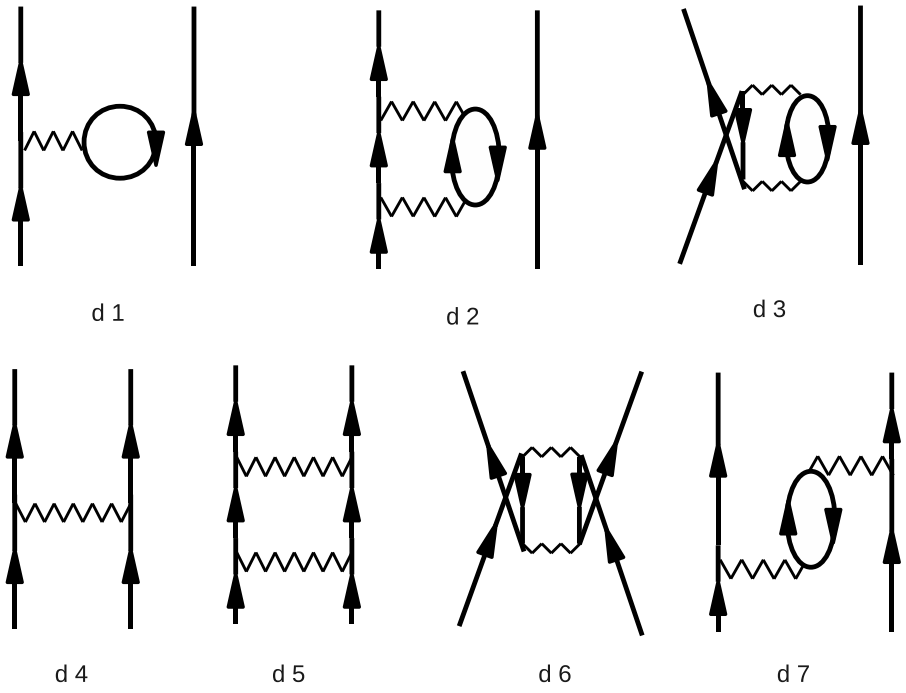

Figure 5.1: Low-order diagrams constituting the $\hat{Q}$-box.

5.2 Formalisms

In this section, we shall describe and discuss the KK [142, 143] and the EKKO [57] iteration methods and their application to microscopic calculations of shell-model effective interactions. These methods, to our knowledge, have not yet been employed in such calculations. Let us begin with a brief review of the LS [139, 140] and KK iteration methods. Consider first the degenerate LS method where the model space is degenerate, namely $PH_0P = W_0$, W_0 being a constant. In terms of the $\hat{Q}$-box of Equation (5.2), the effective interactions R_n are calculated iteratively by [139, 140]

$$R_1 = \hat{Q}(W_0), \tag{5.3}$$

$$R_2 = \frac{1}{1 - \frac{d\hat{Q}}{d\omega} \mid_{\omega=W_0}} \hat{Q}(W_0), \tag{5.4}$$

and

$$R_n = \frac{1}{1 - \hat{Q}_1 - \sum_{m=2}^{n-1} \hat{Q}_m \prod_{k=n-m+1}^{n-1} R_k} \hat{Q}(W_0) \tag{5.5}$$

where the derivatives are

$$\hat{Q}_m = \frac{1}{m!} \frac{d^m \hat{Q}}{d\omega^m} \mid_{\omega=W_0} . \tag{5.6}$$

The effective interaction is given by the converged R_n, namely

$$V_{\text{eff}} = R_{n+1} = R_n. \tag{5.7}$$

There is a practical difficulty for the above iteration method. In actual shell-model calculations, it is usually not possible to calculate the vertex function $\hat{Q}$-box exactly; thus it is a common practice to evaluate it with some low-order approximations and calculate the derivatives $\hat{Q}_m$ by numerical differentiation, which is often a delicate undertaking and not accurate when m is large, say $m > 5$. As a result, the above iteration is in practice limited to low orders where numerical differentiations are reliable.

The above degenerate LS iteration method can be generalized to a non-

degenerate one [141], namely PH_0P being non-degenerate. In this situation, in addition to the $\hat{Q}$-box of Equation (5.2), we now also need the generalized $\hat{Q}$-box defined as

$$\hat{Q}_n(12\cdots(n+1)) = (-1)^n[PVQg_1^Qg_2^Q\cdots g_{n+1}^QQVP]_L. \tag{5.8}$$

with

$$g_\alpha^Q \equiv \frac{1}{\epsilon_\alpha - QHQ}. \tag{5.9}$$

In the above $\hat{Q}_n(1,2,\cdots,(n+1))$ is for $n \geq 1$, ϵ_α is defined by $PH_0P\phi_\alpha = \epsilon_\alpha\phi_\alpha$, and $P = \Sigma_{m\leq d}P_m$ and $P_m = |\phi_m\rangle\langle\phi_m|$. d is the dimension of the P-space. Note that only valence-linked diagrams are retained in $\hat{Q}_n(\epsilon_1,\cdots,\epsilon_{n+1})$, as indicated by the subscript L.

With the above definitions, the effective interaction given by the degenerate LS iteration method is given as [141]

$$\begin{aligned}
R_1 &= \sum_\alpha \hat{Q}(\epsilon_\alpha)P_\alpha, \\
R_2 &= \sum_\alpha \left[1 - \sum_\beta \hat{Q}_1(\alpha\beta)P_\beta\right]^{-1} \hat{Q}(\epsilon_\alpha)P_\alpha, \\
R_3 &= \sum_\alpha \left[1 - \sum_\beta \hat{Q}_1(\alpha\beta)P_\beta - \sum_{\beta\gamma}\hat{Q}_2(\alpha\beta\gamma)P_\beta R_2 P_\gamma\right]^{-1} \\
&\quad \times\hat{Q}(\epsilon_\alpha)P_\alpha, \\
&\quad \cdots \\
&\quad \cdots
\end{aligned} \tag{5.10}$$

When convergent, we have $V_{\text{eff}} = R_{n+1} = R_n$. The above non-degenerate LS method can be used to calculate the effective interactions for non-degenerate model spaces such as the two-shell space $sdpf$. But this method is rather complicated for computations, and this has hindered its application to microscopic calculations of shell-model effective interactions. To our knowledge, the above non-degenerate LS method has only been applied to the effective interactions for the $0p$ shell [151].

We now describe some details of the non-degenerate KK and EKKO methods which are both suitable for the non-degenerate situation. The KK iteration method was originally developed for model spaces which are degenerate [142]. A non-degenerate KK iteration method was later formulated [143], with the effective interaction given by the following iteration methods. Let the effective interaction for the ith iteration be $V_{\rm eff}^{(i)}$ and the corresponding eigenvalues E and eigenfunctions χ be given by

$$[PH_0P + V_{\rm eff}^{(i)}]\chi_m^{(i)} = E_m^{(i)}\chi_m^{(i)}. \tag{5.11}$$

Here χ_m is the P-space projection of full-space eigenfunction Ψ_m, namely $\chi_m = {\rm P}\Psi_m$. The effective interaction for the next iteration is then

$$V_{\rm eff}^{(i+1)} = \Sigma_m[PH_0P + \hat{Q}(E_m^{(i)})]|\chi_m^{(i)}\rangle\langle\tilde{\chi}_m^{(i)}| - PH_0P, \tag{5.12}$$

where the bi-orthogonal states are defined by

$$\langle\chi_m|\chi_{m'}\rangle = \delta_{m,m'}. \tag{5.13}$$

Note that in the above PH_0P is non-degenerate. The converged eigenvalue E_m and eigenfunction χ_m satisfy the P-space self-consistent condition

$$(E_m(\omega) - H_0)\chi_m = \hat{Q}(\omega)\chi_m,\ \omega = E_m(\omega). \tag{5.14}$$

To start the iteration, we use

$$V_{\rm eff}^{(1)} = \hat{Q}(\omega_0) \tag{5.15}$$

where ω_0 is a starting energy chosen to be close to PH_0P. The converged KK effective interaction is given by $V_{\rm eff} = V_{\rm eff}^{(n+1)} = V_{\rm eff}^{(n)}$. When convergent, the resultant $V_{\rm eff}$ is independent of ω_0, as it is the states with maximum P-space overlaps which are selected by the KK method [142]. We shall discuss this feature later in section 5.3.1 using a solvable model. The above non-degenerate KK method is numerically more convenient than the non-degenerate LS method.

The diagrams of Figure 5.1 have both one-body (d1,d2,d3) and two-body (d4,d5,d6,d7) diagrams. When we calculate nuclei with two valence nucleons such as ^{18}O and ^{18}F, all these seven diagrams are included for the$\hat{Q}$-box. However, for nuclei with one valence nucleon such as ^{17}O, we deal with the 1-body $\hat{S}$-box such as the sum of diagrams d1, d2 and d3. The 1-body effective interaction is given by a similar KK iteration

$$S_{\rm eff}^{(i+1)} = \Sigma_m [PH_0P + \hat{S}(E_m^{(i)})]|\chi_m^{(i)}\rangle\langle\tilde{\chi}_m^{(i)}| - PH_0P. \tag{5.16}$$

Denoting its converged value as $S_{\rm eff}$, the model-space s.p. energy $\epsilon_m^{\rm eff}$ is given by $P_m(H_0 + S_{\rm eff})P_m$. By adding and then subtracting $S_{\rm eff}$, we can rewrite Equation (5.14) as

$$(E_m(\omega) - H_0^{\rm eff})\chi_m = [\hat{Q}(\omega) - S_{\rm eff}]\chi_m,\ \omega = E_m(\omega), \tag{5.17}$$

with $H_0^{\rm eff} = H_0 + S_{\rm eff}$. In most shell model calculations [136, 137], one often uses the experimental s.p. energies. This treatment for the s.p. energies is in line with the above subtraction procedure, as $P(H_0 + S_{\rm eff})P$ represents the physical s.p. energy which in principle can be extracted from experiments. In this chapter we shall use the experimental s.p. energies for the model-space orbits together with the $V_{\rm eff}$ derived from $(\hat{Q} - S_{\rm eff})$. A similar subtraction procedure has also been employed in the LS calculations [134, 135] where the all-order sum of the one-body diagrams were subtracted from the calculation of the effective interaction.

In several aspects, the above KK method provides a more desirable framework for effective interaction calculations than the commonly used LS method. The KK method can be more conveniently applied to non-degenerate model spaces than the LS method. In addition, high-order LS calculations requires high-order derivatives of the $\hat{Q}$-box which are often difficult to calculate, while in the KK method we do not need any $\hat{Q}$-box derivatives. But the KK method still has a shortcoming when applied to calculations with extended model space such as as the two-shell $sdfp$ one. For example, certain 2nd-order diagrams for this case may become divergent, making the $\hat{Q}$-box divergent and disrupting

the iteration method. It is remarkable that this singularity difficulty can be circumvented by the recently proposed EKKO method of Okamoto *et al.* [57]. In this method, the vertex function $\hat{Z}$-box is employed. It is related to the $\hat{Q}$-box by

$$\hat{Z}(\omega) = \frac{1}{1-\hat{Q}_1(\omega)}[\hat{Q}(\omega) - \hat{Q}_1(\omega)P(\omega - H_0)P], \tag{5.18}$$

where $\hat{Q}_1$ is the first-order derivative of the $\hat{Q}$-box. The $\hat{Z}$-box considered by Okamoto *et al.* [57] is for degenerate model spaces ($PH_0P = W_0$), while we consider here a more general case with non-degenerate PH_0P. An important property of the above $\hat{Z}$-box is that it is finite when $\hat{Q}$-box is singular (has poles). Note that $Z(\omega)$ satisfies

$$\hat{Z}(\omega)\chi_m = \hat{Q}(\omega)\chi_m \; at \; \omega = E_m(\omega). \tag{5.19}$$

The iteration method for determining the effective interaction for the $\hat{Z}$-box case is quite similar to that for the $\hat{Q}$-box. Suppose the effective interaction for the ith iteration is $V^{(i)}_{\text{eff}-\text{Z}}$. The corresponding eigenfunction χ and eigenvalues E^Z are determined by

$$[PH_0P + V^{(i)}_{\text{eff}-\text{Z}}]\chi^{(i)}_m = E^{Z(i)}_m \chi^{(i)}_m. \tag{5.20}$$

The effective interaction for the next iteration is

$$V^{(i+1)}_{\text{eff}-\text{Z}} = \Sigma_m[PH_0P + \hat{Z}(E^{Z(i)}_m)]|\chi^{(i)}_m\rangle\langle\tilde{\chi}^{(i)}_m| - PH_0P, \tag{5.21}$$

where the χ's are biorthogonal vectors ($\langle\chi_m|\chi_n\rangle = \delta_{mn}$). Although $\hat{Q}(\omega)$ and $\hat{Z}(\omega)$ are generally different, it is interesting that the converged eigenvalues E_m of $P(H_0 + V_{\text{eff}})P$ and the corresponding ones E^Z_m of $P(H_0 + V_{\text{eff}-\text{Z}})P$ are both exact eigenvalue of the full-space Hamiltonian $H = H_0 + V$. Note, however, that the KK and EKKO methods may reproduce different eigenvalues of the full-space Hamiltonian H. This aspect together with with some other comparisons of these methods will be discussed in section 5.3.1, using a simple solvable model.

For the degenerate case, Okamoto *et al.* [57] have shown that $\frac{dE^Z_m(\omega)}{d\omega}$ =0

at the self-consistent point $\omega = E_m^Z(\omega)$. As outlined below, we have found that this result also holds the case of non-degenerate PH_0P. From Equation (5.18), we have

$$\frac{dZ}{d\omega} = \frac{2}{1-\hat{Q}_1}\hat{Q}_2\frac{1}{1-\hat{Q}_1}[\hat{Q}-\hat{Q}_1(\omega-H_0)] - \frac{1}{1-\hat{Q}_1}\hat{Q}_2(\omega-H_0). \tag{5.22}$$

Then from Equations (5.14 - 5.19) we have

$$[\frac{dZ(\omega)}{d\omega}]_{\omega=E_m^Z}|\chi_m\rangle = 0, \tag{5.23}$$

and

$$[\frac{dE_m^Z(\omega)}{d\omega}]_{\omega=E_m^Z} = 0. \tag{5.24}$$

This is a useful result; it states that at any self-consistent point the eigenvalues $E_m^Z(\omega)$ varies 'flatly' with ω, a feature certainly helpful to iterative calculations. In section 5.3, we shall check this feature numerically.

We now describe how to include the effects of the leading-order chiral three-body interaction, V_{3N}, in our calculations. We consider the NN interaction as given by $V = (V_{2N} + V_{3N}^{\rm med})$, where V_{2N} is the NN interaction obtained from the N^{3}LO two-body potential [148] and $V_{3N}^{\rm med}$ is a density-dependent two-body interaction obtained from the chiral three-body forces (NNN) by closing one pair of external lines and summing over the filled Fermi sea of nucleons. The leading contribution to V_{3N} occurs at N^{2}LO in the chiral power counting and is composed of a long-range two-pion exchange component $V_{3N}^{2\pi}$, a medium-range one-pion exchange term $V_{3N}^{1\pi}$, and a pure contact interaction V_{3N}^{ct}:

$$V_{3N}^{(2\pi)} = \sum_{i\neq j\neq k}\frac{g_A^2}{8f_\pi^4}\frac{\boldsymbol{\sigma}_i\cdot\boldsymbol{q}_i\,\boldsymbol{\sigma}_j\cdot\boldsymbol{q}_j}{(\boldsymbol{q_i}^2+m_\pi^2)(\boldsymbol{q_j}^2+m_\pi^2)}F_{ijk}^{\alpha\beta}\tau_i^\alpha\tau_j^\beta, \tag{5.25}$$

$$V_{3N}^{(1\pi)} = -\sum_{i\neq j\neq k}\frac{g_A c_D}{8f_\pi^4\Lambda_\chi}\frac{\boldsymbol{\sigma}_j\cdot\boldsymbol{q}_j}{\boldsymbol{q_j}^2+m_\pi^2}\boldsymbol{\sigma}_i\cdot\boldsymbol{q}_j\,\boldsymbol{\tau}_i\cdot\boldsymbol{\tau}_j, \tag{5.26}$$

$$V_{3N}^{(\rm ct)} = \sum_{i\neq j\neq k}\frac{c_E}{2f_\pi^4\Lambda_\chi}\boldsymbol{\tau}_i\cdot\boldsymbol{\tau}_j, \tag{5.27}$$

where $g_A = 1.29$, $f_\pi = 92.4$ MeV, $\Lambda_\chi = 700$ MeV, $m_\pi = 138.04$ MeV/c^2 is the

average pion mass, $\boldsymbol{q}_i = \boldsymbol{p_i}' - \boldsymbol{p}_i$ is the difference between the final and initial momentum of nucleon i and

$$\begin{aligned} F_{ijk}^{\alpha\beta} &= \delta^{\alpha\beta}\left(-4c_1 m_\pi^2 + 2c_3 \boldsymbol{q}_i \cdot \boldsymbol{q}_j\right) \\ &+ c_4 \epsilon^{\alpha\beta\gamma}\tau_k^\gamma \boldsymbol{\sigma}_k \cdot \left(\boldsymbol{q}_i \times \boldsymbol{q}_j\right). \end{aligned} \tag{5.28}$$

The low-energy constants $c_1 = -0.76\,\mathrm{GeV}^{-1}$, $c_3 = -4.78\,\mathrm{GeV}^{-1}$, and $c_4 = 3.96\,\mathrm{GeV}^{-1}$ appear already in the N^{2}LO two-body potential and are therefore constrained by low-energy NN phase shifts [152]. The low-energy constants c_D and c_E are typically fit to reproduce the properties of light nuclei [23, 144, 145].

A general three-body force may be written in second quantization as

$$\hat{V}_{3N} = \frac{1}{36}\sum_{123456} V([123],[456]) b_1^\dagger b_2^\dagger b_3^\dagger b_6 b_5 b_4, \tag{5.29}$$

where the antisymmetrized matrix element is

$$V([123],[456]) \equiv \langle 123|V_{3N}|456 + 645 + 564 - 654 - 546 - 465\rangle. \tag{5.30}$$

Here $\langle 123|V_{3N}|456\rangle$ is a simple product matrix element, and $b^\dagger$ and b are creation and destruction operators defined with respect to the particle-hole vacuum $|C\rangle$ with $b_k|C\rangle = 0$ for all k. From Equations (5.25-5.28) we can write $V_{3N} = V_{3N}^{(1)} + V_{3N}^{(2)} + V_{3N}^{(3)}$, where $V_{3N}^{(i)}$ is the component of V_{3N} that is symmetric with respect to the interchange $j \leftrightarrow k$. Now we contract one pair of the $b^\dagger$ and b operators of the above $\hat{V}_{3N}$ (both operators must be holes), and this leads to an effective two-body force

$$\hat{V}_{3N}^{\mathrm{med}} = \frac{1}{4}\sum_{1245} D([12],[45]) b_1^\dagger b_2^\dagger b_5 b_4, \tag{5.31}$$

with

$$
\begin{aligned}
D([12],[45]) &= \sum_{i\le k_F} \Big[\langle i12|V_{3N}^{(2)}|i45\rangle + \langle 1i2|V_{3N}^{(2)}|4i5\rangle \\
&+ \langle 12i|V_{3N}^{(2)}|45i\rangle - \langle 1i2|V_{3N}^{(2)}|i45\rangle \\
&- \langle i12|V_{3N}^{(2)}|4i5\rangle - \langle 12i|V_{3N}^{(2)}|4i5\rangle \\
&- \langle 1i2|V_{3N}^{(2)}|45i\rangle + \langle i12|V_{3N}^{(2)}|45i\rangle \\
&+ \langle 12i|V_{3N}^{(2)}|i45\rangle - (4 \leftrightarrow 5) \Big] , \qquad (5.32)
\end{aligned}
$$

where $4 \leftrightarrow 5$ denotes the nine exchange terms. The above result is unchanged when $V_{3N}^{(2)}$ is replaced by either $V_{3N}^{(1)}$ or $V_{3N}^{(3)}$. In other words, we may use any of these three to calculate the density-dependent two-body force. In our calculations we consider a background medium of symmetric nuclear matter at constant density characterized by a Fermi momentum k_F. In this way analytic expressions can be obtained for $V_{3N}^{\rm med}$, as shown in refs. [146, 149]. The above is a density dependent effective 'two-body' interaction which, unlike its underlying three-body force, can be readily used in many-body problems.

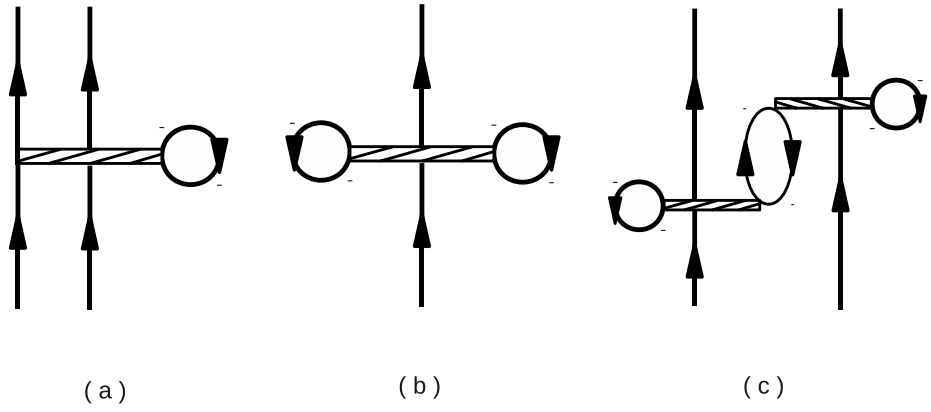

Figure 5.2: $\hat{Q}$-box diagrams with three-body forces. Each V_{3N}^{med} interaction is represented by a 'narrow band with hole-line-loop' vertex.

As detailed in [149], the partial-wave potentials of the above V_{3N}^{med} have been derived from the lowest-order three-body force. We shall use them in our calculations, namely we shall consider the nucleon interaction as given

by $(V_{2N} + V_{3N}^{med})$. In so doing, the $\hat{Q}$-box diagrams for effective interactions will have a specific type of V_{3N} vertices as illustrated in Figure 5.2. Recall that diagram d4 of Figure 5.1 represents the interaction between two valence nucleons via V_{2N}. This diagram becomes diagram (a) of Figure 5.2 if its V_{2N} is replaced by V_{3N}^{med}. Here the two valence nucleons have to have the participation of a sea-body (below Fermi sea) in order to activate V_{3N}, as indicated by the hole-line loop in the diagram. Similarly diagram d1 of Figure 5.1 represents the interaction of a valence nucleon with a sea-body via the two-body interaction V_{2N}. If this interaction is replaced by V_{3N}^{med}, this diagram becomes diagram (b) of Figure 5.2. V_{3N} must involve three nucleons, and hence here the valence nucleon interacts with 'two' sea-bodies as indicated by the two hole-line loops attached to V_{3N}. Diagram (c) is the V_{3N} core polarization diagram corresponding to diagram d7 of Figure 5.1. Again here one hole-line loop is needed for each vertex to activate V_{3N}. As seen from Equations (5.30 - 5.32), V_{3N}^{med} requires the involvement of at least one sea-body, and it is this requirement which is reflected by the hole-line loops attached to the V_{3N} vertices in Figure 5.2.

5.3 Results and Discussion

5.3.1 Model calculations using LS, KK and EKKO methods

In this section we shall study the above iteration methods by way of a simple matrix model, similar to the one employed in [57]. We consider a 4-dimensional matrix Hamiltonian $H = H_0 + H_1$ where

$$H_0 = \begin{bmatrix} PH_0P & 0 \\ 0 & QH_0Q \end{bmatrix} \tag{5.33}$$

and

$$PH_0P = \begin{bmatrix} \varepsilon_{p1} & 0 \\ 0 & \varepsilon_{p2} \end{bmatrix};\ QH_0Q = \begin{bmatrix} \varepsilon_{q1} & 0 \\ 0 & \varepsilon_{q2} \end{bmatrix}. \tag{5.34}$$

The interaction Hamiltonian has a strength parameter x, namely

$$H_1 = \begin{bmatrix} PH_1P & PH_1Q \\ QH_1P & QH_1Q \end{bmatrix}, \tag{5.35}$$

with

$$\begin{aligned} PH_1P &= \begin{bmatrix} 0 & 5x \\ 5x & 10x \end{bmatrix}; \\ PH_1Q &= QH_1P = \begin{bmatrix} 0 & 8x \\ 8x & 0 \end{bmatrix}; \\ QH_1Q &= \begin{bmatrix} -5x & x \\ x & -5x \end{bmatrix}. \end{aligned} \tag{5.36}$$

As discussed before, both the KK and EKKO iteration methods are rather convenient for non-degenerate model spaces. We would like to check this feature by carrying out some calculations using the above model. We consider two unperturbed Hamiltonians, given by (ε_{p1}, ε_{p2}, ε_{q1}, ε_{q2})=(0,6,4,9) and (0,0,4,9). The PH_0P parts of them are, respectively, non-degenerate and degenerate.

In the first three paragraphs of Table 5.1, some results for the PH_0P=(0,6) case are presented. Here E_n are the exact eigenvalues of the full Hamiltonian, with their model-space overlaps denoted by $(n|P|n)$. $E_{\rm KK}$ and $E_{\rm EKKO}$ are the eigenvalues generated respectively by the KK and EKKO iterations methods. The above PH_0P not only is non-degenerate but also has its spectrum intersecting with that of QH_0Q. One would expect that this PH_0P may cause difficulty to the above iteration methods. But as indicated there, both the non-degenerate KK and the non-degenerate EKKO iteration methods work remarkably well. Note that the interaction used here is rather strong (x=0.6), and both methods still work well, converging to E_ns which are quite far from PH_0P.

Some results for the degenerate case of PH_0P=(0,0) are listed in the last two paragraphs of Table 5.1. Here we have performed calculations using the degenerate LS method through 5th order iteration (i.e. in Equation (5.7) we

Table 5.1: Results of model calculations using the LS, KK and EKKO iteration methods. See text for other explanations.

H_0= (0,6,4,9)	x=0.10			
E_n	-0.110705	3.328164	7.203243	8.579299
$(n\|P\|n)$	0.991108	0.044558	0.953368	0.010966
E_{KK}	-0.110705	7.203243		
E_{EKKO}	-0.110705	7.203242		
	x =0.30			
E_n	-0.974184	1.808716	8.080888	10.084581
$(n\|P\|n)$	0.906155	0.111257	0.113523	0.869066
E_{KK}	-0.974185	10.084580		
E_{EKKO}	-0.974185	10.084581		
	x =0.60			
E_n	-3.510377	-0.286183	8.265089	14.531471
$(n\|P\|n)$	0.709531	0.189318	0.232422	0.868729
E_{KK}	-3.510377	14.531472		
E_{EKKO}	-3.510363	14.531472		
H_0=(0,0,4,9)	x= 0.10			
E_n	-0.296201	0.982861	3.736229	8.577111
$(n\|P\|n)$	0.985416	0.922993	0.082811	0.008780
E_{LS}	-0.314591	0.872176		
E_{KK}	-0.296201	0.982860		
E_{EKKO}	-0.296201	0.982860		
	x= 0.30			
E_n	-1.448782	0.906504	5.254129	8.288149
$(n\|P\|n)$	0.868986	0.460296	0.566014	0.104704
E_{LS}	-1.620734	0.339561		
E_{KK}	-1.125579	5.515468		
E_{EKKO}	-1.448782	0.906504		

use $V_{\rm eff} = R_5$). As shown, the results so obtained are not in good agreement with the exact results. This suggests that low-order LS iteration method may often be inadequate, and one needs higher-order iterations to obtain accurate results.

It has been known that the KK iteration method converges to the states with maximum P-space overlaps [142], while the LS method converges to the states of lowest energies [139, 140]. We have found that for many cases the EKKO method also converges to states of maximum P-space overlaps. As listed in the third paragraph of the Table, both the KK and EKKO methods converge to states of energies E_n= -3.51 and 14.53 whose P-space probabilities are relatively 0.70 an 0.86. We have also found that the EKKO and KK iteration methods can converge to different states. An example is the results shown in the last part of the Table, where the EKKO method converges to states of energy (P-space probability) -1.448 (0.868) and 0.906 (0.460) while the states of maximum probability are the first one and the third state with 5.254 (0.566). Note that for this case the EKKO method is clearly more accurate than the KK one.

We have noticed that for a number of cases the EKKO method converges well but not so for the KK method. This is largely because these two methods treat the singularities of the $\hat{Q}$-box differently. To see this, let us perform a graphical solution for the x=0.60 case of the Table. Using the parameters of this case, we calculate and plot in Figure 5.3 $E^Q_m(\omega)$ and $E^Z_m(\omega)$ which are respectively the eigenvalues of $P[H_0 + \hat{Q}(\omega)]P$ and $P[H_0 + \hat{Z}(\omega)]P$. As discussed in section II, they have identical self-consistent solutions, namely $\omega = E^Q_m(\omega) = E^Z_m(\omega) \equiv E_m$ where E_m is the eigenvalue of the full-space Hamiltonian. Recall that $\hat{Q}$ and $\hat{Z}$ are given respectively by Equations (5.2 and 5.18). As shown in the figure, the curves of E^Q and E^Z do have identical self-consistent solutions as marked by the common intersection points E_1, E_2, E_3 and E_4. Note that the above two curves are distinctively different from each other, particularly in the vicinity of the poles (marked by the vertical lines through F_1 and F_2) of the $\hat{Q}$-box. There $E^Q(\omega)$ is discontinuous, diverging oppositely before and after the pole, while $E^Z(\omega)$ remains continuous throughout. This clearly helps the convergence of the $\hat{Z}$-box iteration method:

The $\hat{Z}$-box iteration proceeds along a continuous $E^Z(\omega)$ curve, while the $\hat{Q}$-box iteration often does not converge as it may bounce back and forth across the discontinuity.

As seen from Equation (5.18), the $\hat{Z}$-box method has 'false' solutions at $E_q^Z(\omega) = \omega = \mu_q \equiv F_q$. These solutions are marked in Figure 5.3 as F_1 and F_2. These false solutions can be readily recognized and discarded. As given in Equation (5.24), we have at self-consistent points $\frac{dE_m^Z}{d\omega} = 0$. As shown in Figure 5.3, the slopes of E^Z do satisfy the above condition at the self-consistent points E_1 to E_4, but not so at the false points F_1 and F_2.

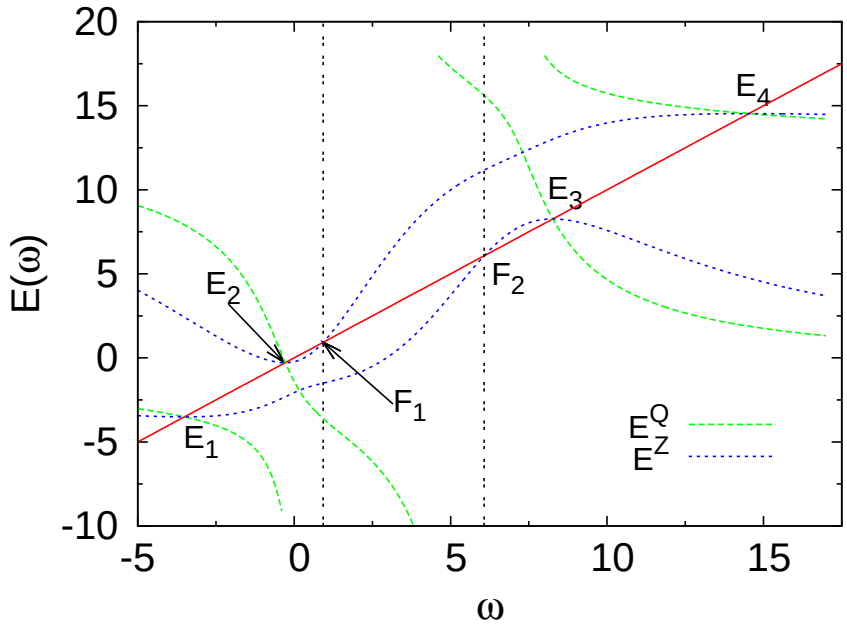

Figure 5.3: Graphical solutions for the $\hat{Q}$- and $\hat{Z}$-box self-consistent equations. See text for other explanations.

5.3.2 Nuclear matter and chiral three-body forces

As described before, we shall calculate the shell-model effective interactions with the inclusion of the medium-dependent three-body force V_{3N}^{med} which is obtained from a chiral three-body forces by integrating one participating sea-body over the Fermi sea. Before doing so, we need to choose or decide the

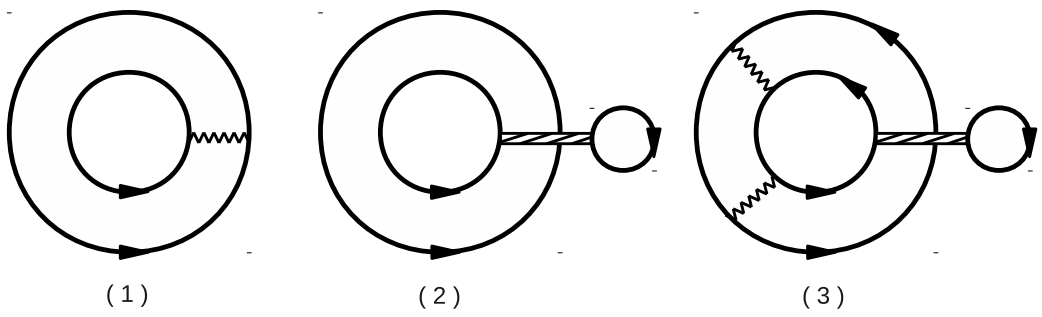

Figure 5.4: Nuclear matter ring diagrams with vertices from V_{2N} (wavy line) and V_{3N}^{med} (narrow band with hole-line-loop).

low-energy constants of V_{3N} (see Equations (5.25 - 5.27)) to be used in our calculations. The low-energy constants c_1, c_3 and c_4 of $V_{3N}^{(2\pi)}$ are well determined; they are constrained by low-energy NN scattering data [152]. Their values so determined will be used in the present work. But the low-energy constants c_D and c_E, of $V_{3N}^{(1\pi)}$ and $V_{3N}^{(ct)}$ respectively, are less well known; their values determined from properties of light nuclei exhibit considerable variations [23, 144–146]. The V_{3N}^{med} interaction depends explicitly on the Fermi momentum k_F which is well defined for nuclear matter. But k_F is not well defined for finite nuclei, causing an uncertainty in determining the low-energy constants of V_{3N}^{med} from properties of finite nuclei. To circumvent this uncertainty, we have thus chosen to fix these constants by way of nuclear matter calculations with V_{3N}^{med} included. We fit the constants c_D and c_E by requiring them to reproduce satisfactorily the saturation density n_0 and energy per particle E_0/A of symmetric nuclear matter. It is convenient that k_F is well determined for nuclear matter. (It is not so for finite nuclei, for which we shall use a local density approximation for determining k_F as we shall discuss later.)

We calculate the EoS for symmetric nuclear matter using a ring-digram formalism [44, 45, 58]. A brief description of this formalism is presented below, to outline how we include V_{3N}^{med} in our calculations. Discussed in section 1.4, the low-momentum interaction $V_{low-k}(\Lambda)$ derived from the realistic NN interactions was employed, Λ being the decimation scale. Our present ring-

diagram calculations include in addition the interaction V_{3N}^{med}. Using familiar renormalization procedures [36–38] , we first obtain the low-momentum interaction $V_{low-k}^{3N}(\Lambda)$ from V_{3N}^{med}. Using the above ring-diagram framework, the ground-state energy shift ΔE is given by the all-order sum of the *pphh* ring diagrams as illustrated in Figure 5.4. These ring diagrams contains vertices from both V_{low-k}^{2N} which is calculated from the N^{3}LO chiral NN potential [148] and V_{low-k}^{3N} obtained from the lowest order chiral V_{3N} as described before. Similar to Figure 5.2, to have the pair of nucleons in the ring diagrams interact with V_{3N} there must be the participation of a third nucleon. Thus the V_{3N} vertices in Figure 5.4 all have a one-hole-line loop attached to them.

With these ring diagram summed to all orders, the ground-state energy shift for nuclear matter is given by Equation (1.6) in section 1.4.

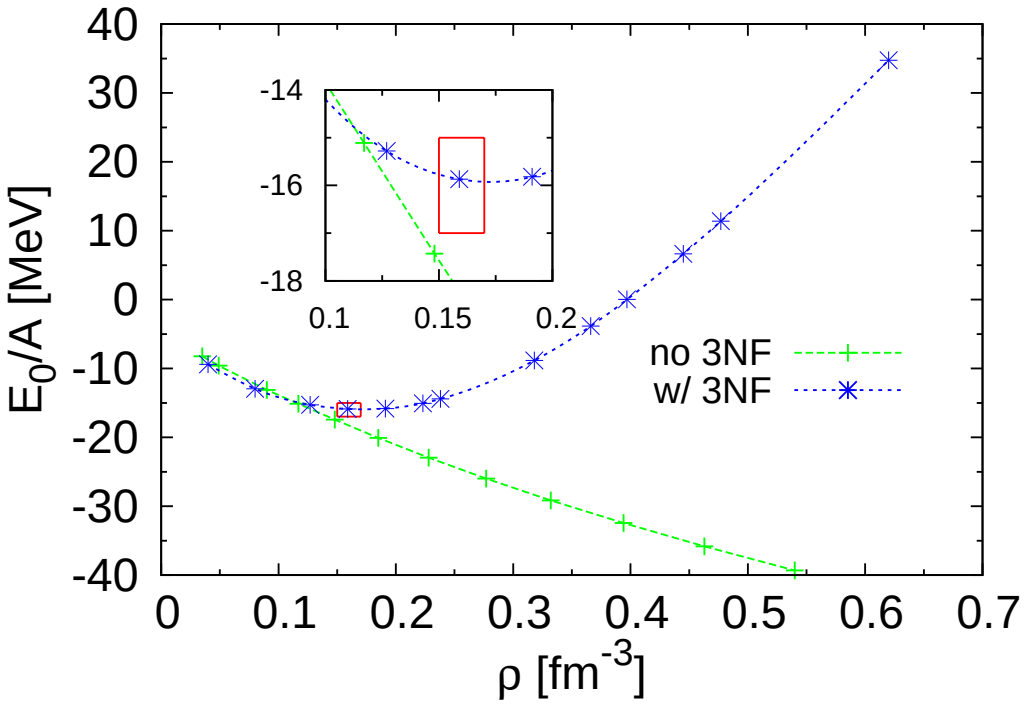

Figure 5.5: Ring-diagram equation of state for symmetric nuclear matter calculated with and without V_{3N}.

We have carried out ring-diagram calculations for symmetric nuclear matter using a wide range values for c_D and c_E. Our results with $c_D = -2.8$ and

$c_E = 0.8$ are displayed in Figure 5.5; they give $E_0/A \simeq -16$ MeV and $\rho_0 \simeq 0.16$ fm^{-3}, both in satisfactory agreement with the empirical values. Two curves are shown in the figure, one with V_{2N} alone and the other with the addition of V_{3N}^{med}. Comparing with the V_{2N} curve, it is of interest that the effect of V_{3N}^{med} is slightly attractive for low densities ($\lesssim 2\rho_0/3$) while becomes strongly repulsive at high densities. A common decimation scale of $\Lambda = 2.1$ fm^{-1} is used for both V_{low-k}^{2N} and V_{low-k}^{3N}. It may be mentioned that in the ring-diagram calculations with BR scaling [44, 58] a larger Λ of ~ 3.0fm^{-1} is needed for obtaining satisfactory nuclear matter saturation properties. Further comparison of the BR scaling with V_{3N} should be of interest. The above c_D and c_E values will be employed in our shell model calculations.

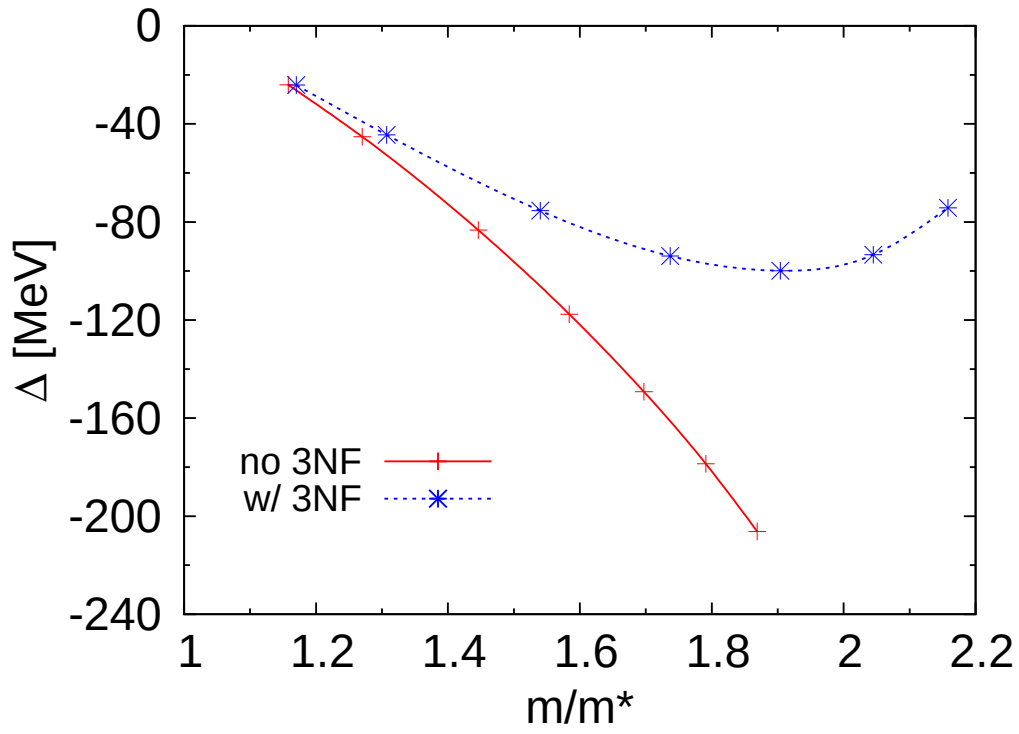

Figure 5.6: Comparison of m^* and Δ for the in-medium s.p. spectrum calculated with and without V_{3N}^{med}. See text for other explanations.

We have calculated the HF s.p. spectrum ϵ_k in nuclear matter with the inclusion of both V_{2N} and three-body force V_{3N}^{med}. The inclusion of the latter has been found to have significant effect to the spectrum. ϵ_k can be well

fitted by the quadratic expression $(k^2\hbar^2/(2m^*) + \Delta)$ where m^* is the effective mass and Δ is a well-depth parameter representing the s.p. energy at zero momentum. In Figure 5.6 we present our results for Δ and m/m^* for various densities. Two curves are shown: the lower one without and the top one with the inclusion of V_{3N}^{med}. The densities for the 7 data points of each curve are, from left to right, (0.25, 0.5, 1.0, 1.5, 2.0, 2.5, 3.0 n_0) respectively. As shown by the lower curve of the figure, Δ and m/m^* both vary monotonically with the density when only V_{2N} is employed. With increasing density, Δ becomes increasingly more negative and m/m^* increasingly larger, exhibiting no saturation. The trend is quite different for the upper curve where the three-body force is included. Here m/m^* still monotonically increases with density, but Δ arises after saturation, approaching zero at some high density. It is of interest that V_{3N}^{med} has a large effect in raising the chemical potential of nucleons in high density nuclear matter; this increase of the chemical potential may play an important role in enabling such nucleons decaying into other baryons such as hyperons.

5.3.3 The *sdpf* shell model effective interactions

In this subsection, we shall calculate the effective interactions for both the degenerate *sd* one-shell and the non-degenerate *sdpf* two-shell cases. Before presenting our results, let us first describe some details of our calculations. The LS, KK and EKKO methods as described in section 5.2 will be employed. As also discussed in section 5.2, we first calculate the low-momentum interactions V_{2N}^{low-k} and V_{3N}^{low-k} from, respectively, the chiral V_{2N} and V_{3N}^{med} potentials, using a common decimation scale of $\Lambda = 2.1\text{fm}^{-1}$ for both. This value was chosen because at this scale the low-momentum interactions derived from different NN potentials [10–12, 148] are remarkably close to each other, leading to a nearly unique low-momentum interaction. The above V_{2N}^{low-k} and V_{3N}^{low-k} interactions are then used in calculating the $\hat{Q}$-box diagrams as shown in Figures 5.1 and 5.2. In calculating these diagrams, the hole orbits are summed over the $0s0p$ shells and particle orbits over the $0d1s1p0f$ shells. The active spaces (P-space) used for the one-shell and two-shell calculations are respectively the three

orbits in the *sd* shell and the seven orbits in the *sdpf* shells. The experimental s.p. energies of (0.0, 5.08, 0.87) MeV have been used, respectively, for the $(0d_{5/2}, 0d_{3/2}, 1s_{1/2})$ orbits [153]. The harmonic oscillator constant of $\hbar\omega$=14 MeV has been employed in our calculations.

In Figures 5.7 and 5.8 we compare our *sd* one-shell calculations using V_{2N} only. Here our purpose is mainly to compare the results given by the KK and EKKO method with those given by the commonly used degenerate LS method [134, 135]. To our knowledge, the KK and EKKO methods have not yet been applied to calculations of shell-model effective interactions. It should be useful and of interest to compare the results given by the LS, KK and EKKO methods. Our LS calculations are carried out using a low-order approximation, namely we take $V_{\rm eff} = R_5$ (see Equation (5.7)). For simplicity, we shall just use in our present and subsequent calculations a low-order $\hat{Q}$-box as indicated by the 1st- and 2nd-order diagrams of Figures 5.1 and 5.2. As shown in Figures 5.7 and 5.8, the KK and EKKO results for both ^{18}O and ^{18}F are in fact identical to each other, in consistence with our model calculations displayed in Table 5.1 and Figure 5.3. For these two methods, we have used both iteration and graphical methods, to ensure the convergence of the iterative results.

As displayed in Figures 5.7 and 5.8, it is encouraging that the low-order ($V_{\rm eff} = R_5$) LS method has given results in very good agreement with the KK and EKKO ones. This is possibly because the P- and Q-space employed in the present calculation are not strongly coupled; they have a separation of $2\hbar\omega$. (The model calculations considered in Table 5.1 have much stronger P- and Q-space couplings.) A comparison of our results with experiments [153] is also presented in Figures 5.7 and 5.8. The agreement between our calculated energy levels with experiments is moderately satisfactory for ^{18}O, but for ^{18}F the calculated lowest $(1^+, 3^+, 5^+)$ states, though of correct ordering, are all significantly higher than the experimental values. As discussed in section 5.3.1, the LS method is known to converge to the states of the lowest energies, while the KK method to the states of maximum P-space overlaps. Thus the good agreement between LS and KK in Figures 5.7 and 5.8 is an important indication that the states reproduced by the model-space effective interaction are

likely those of the lowest energies as well as maximum model-space overlaps. It is certainly physically desirable to have the effective interaction reproducing the states of the full Hamiltonian which have the largest model-space overlaps.

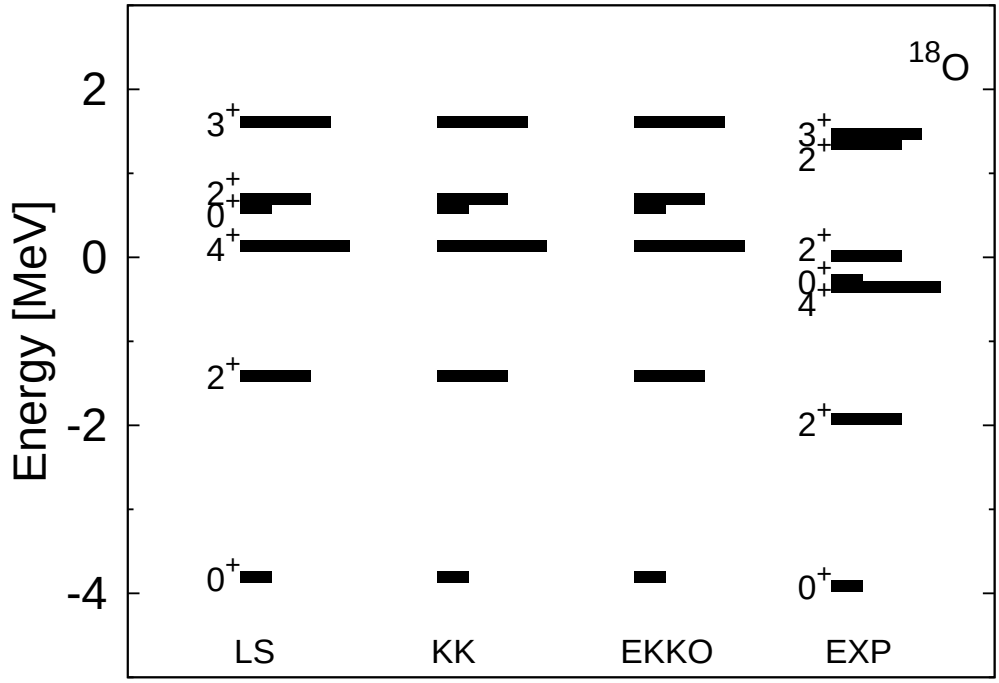

Figure 5.7: *sd*-shell calculations for ^{18}O with the LS, KK and EKKO methods, all employing only V_{2N}.

We now turn to the effect of the three-body potential V_{3N}^{med} on the shell-model effective interactions. As an initial study, we repeat the one-shell calculations of Figures 5.7 and 5.8 with the interaction V_{2N} used there replaced by $(V_{2N}+V_{3N}^{med})$. The results so obtained clearly depends on what V_{3N} we employ. As discussed in section 5.3.2 the low-energy constants c_1, c_3 and c_4 are well constrained by NN scattering data, and for the constants c_D and c_E we have chosen to use their values determined by nuclear matter properties. To carry on the calculations with V_{3N}^{med} we still need to know the 'local density' n_v for the two valence nucleons in the *sd* shell. It should be small, but its precise value is rather uncertain. In the present work, we shall estimate n_v by comparing the density profile of ^{16}O and that for the valence nucleons. In Figure

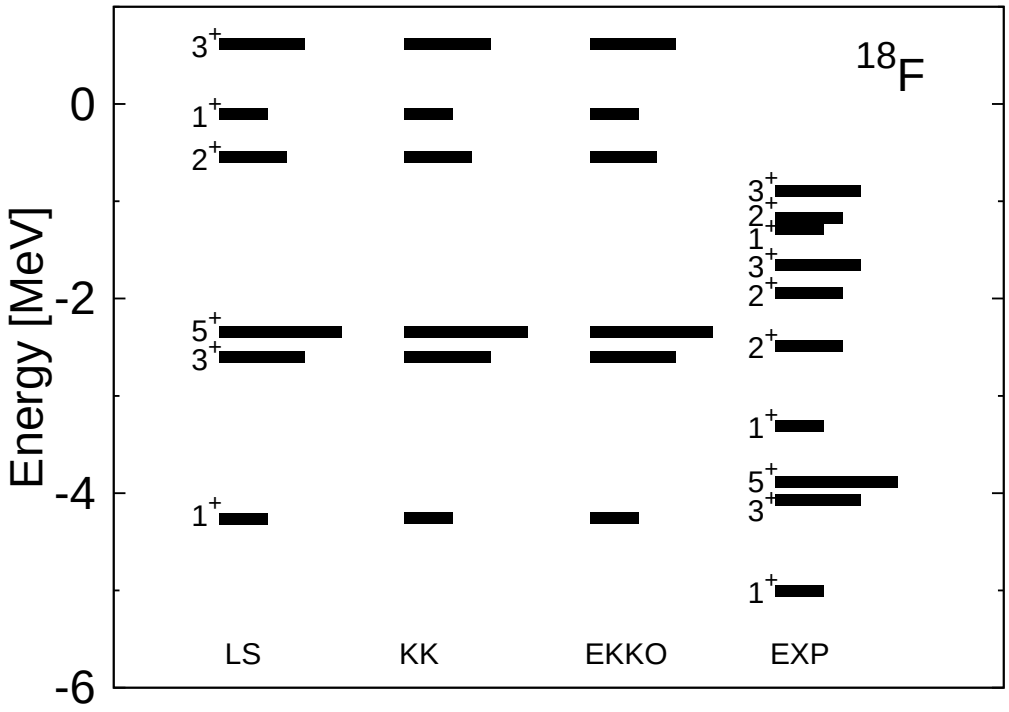

Figure 5.8: Same as Figure 5.7 except for ^{18}F.

5.9 we plot the density profile $n_{\rm core}(r)$ of ^{16}O obtained with its wave function assumed to be a closed shell-model s^4p^{12} core. We also plot the distribution $\Phi(r) = \xi\phi(r)^4$ where $\phi(r)$ is the radial harmonic oscillator wave function for $d_{5/2}$, with the scaling parameter ξ=0.1. As seen from the plots, the pair of $d_{5/2}$ nucleons reside primarily in the low-density region of $n_{\rm core}$. Depending on the averaging procedure employed, we have estimated n_v from $\rho_{\rm core}(r)$ and $\phi(r)$, obtaining values ranging from ~ 0.015 to ~ 0.030fm^{-3}. We have considered another scheme to estimate n_v. The rms radius r_{rms} for the shell-model $d_{5/2}$ orbit is indicated by an arrow in the figure. A simple scheme to estimate n_v is to let it be equal to $n_{\rm core}(r_{\rm rms})$, the value obtained in this way being ~ 0.025fm^{-3}. This value may be reduced if realistic s.p. wave functions are employed. The $d_{3/2}$ orbit is nearly unbounded, and its $r_{\rm rms}$ should be considerably larger than that for $d_{5/2}$. Assuming $\hbar\omega$ =10 MeV for the $d_{3/2}$ orbit, its $r_{\rm rms}$ would be ~ 3.8fm giving $n_v \simeq 0.01$fm^{-3} for this orbit. We believe that a suitable range for n_v is from ~ 0.1 to $\sim 0.2n_0$ ($n_0 \equiv 0.16$fm^{-3}).

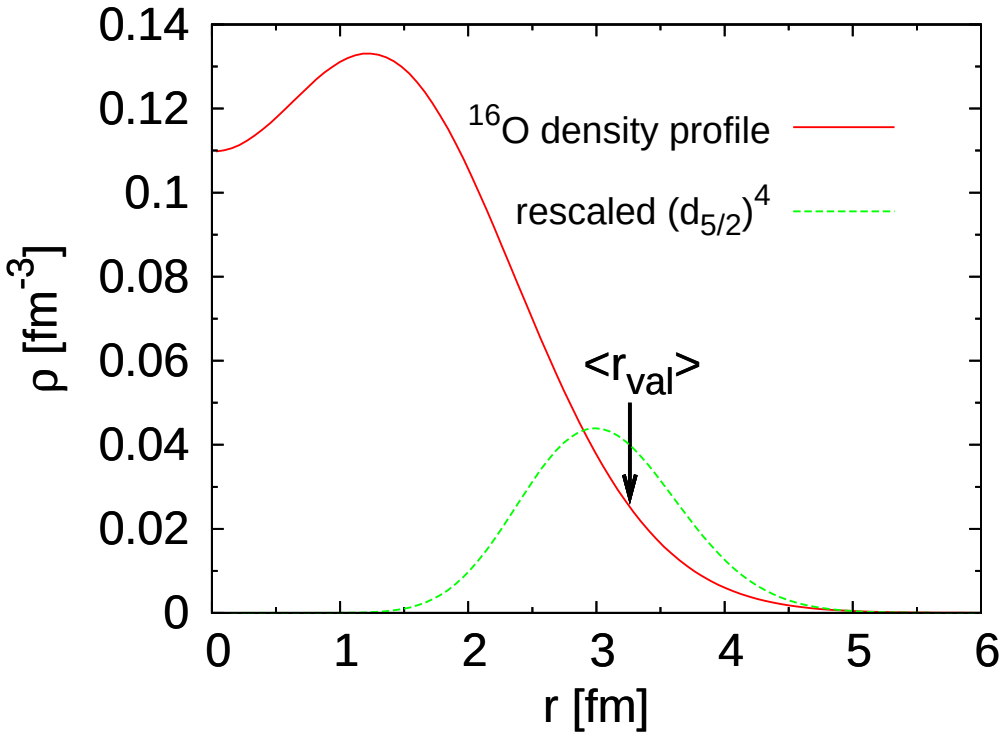

Figure 5.9: Density profile of ^{16}O (solid line) and the radial distribution of the fourth power of the $0d$ shell-model wave function (dashed line). See text for other explanations.

In Figures 5.10 and 5.11, we present our results for ^{18}O and ^{18}F calculated with and without V_{3N}^{med} ($n_v = 0.1n_0$). Comparing with the 'NN' results, the main effect of the 'NNN' force is a small downward shift for the ground states of ^{18}O and ^{18}F, while leaving the other states largely unchanged. This trend is consistent with what we have observed for nuclear matter calculations (see Figure 5.5), namely the effect of V_{3N}^{med} is slightly attractive at low densities. It may be mentioned that we have employed a low-order approximation for the $\hat{Q}$-box, including only 1st- and 2nd-order diagrams. The inclusion of higher-order diagrams may alter our results. As carried by by Holt *et al.* [132], certain classes of planar diagrams of the $\hat{Q}$-box can be summed up to all orders using the Kirson-Babu-Brown induced interaction method. We plan to extend our present calculations by including these planar diagrams in the $\hat{Q}$-box.

Let us now describe our calculations for the non-degenerate *sdpf* effective

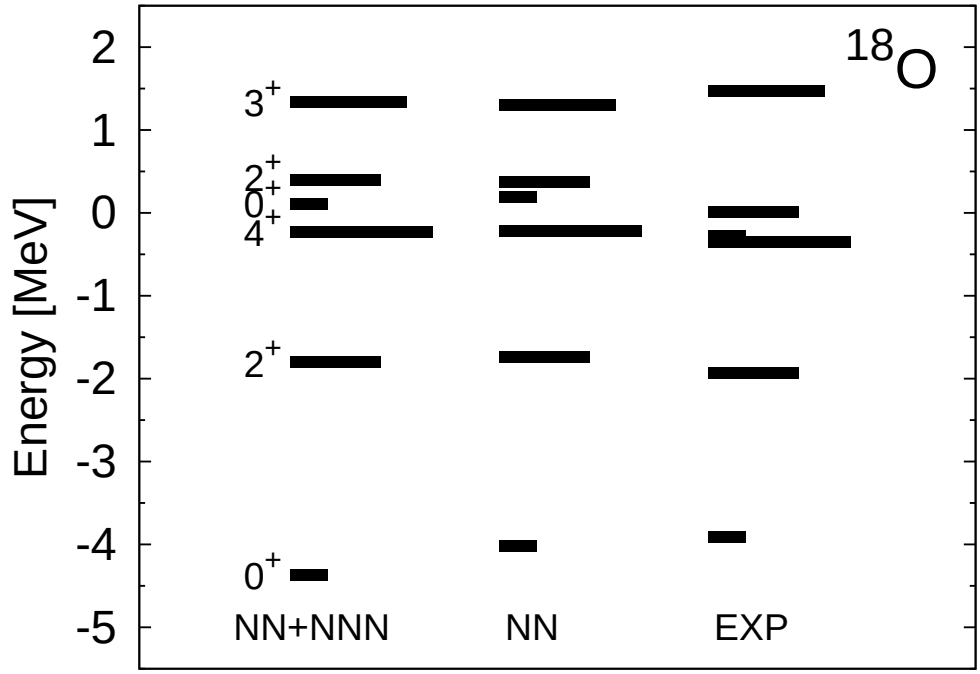

Figure 5.10: Energy spectra of ^{18}O calculated with the *sd* one-shell effective interactions. 'NN' and 'NNN' denote respectively V_{2N} and V_{3N}^{med}.

interactions. The shell-model calculations of Figures 5.7, 5.8, 5.10 and 5.11 have all been carried out using the *sd* one-shell model space. For certain nuclei such as those with a large neutron excess, a larger model space such as the *sdpf* one may be needed and the above effective interactions will be needed. It may be convenient to describe our *sdpf* calculations by way of an example, namely ^{18}O. Consider the $(T = 1, J = 0)$ states of this nucleus. In the *sd* one-shell case, the model space is spanned by three basis states $|j^2, T = 1, J = 0\rangle$, j=$(d_{5/2}, d_{3/2}, s_{1/2})$. For the *sdpf* case, the model space is enlarged, having four additional basis states of the same type with j=$(p_{3/2}, p_{1/2}, f_{7/2}, f_{5/2})$. The whole model space is now non-degenerate as the *pf* orbits are one shell above the *sd* ones. We shall employ the non-degenerate KK and EKKO methods to calculate the effective interactions for this two-shell space. As illustrated in section 5.3.1, both of these methods have been applied to non-degenerate model calculations. Here we would like to study if they are also suitable for

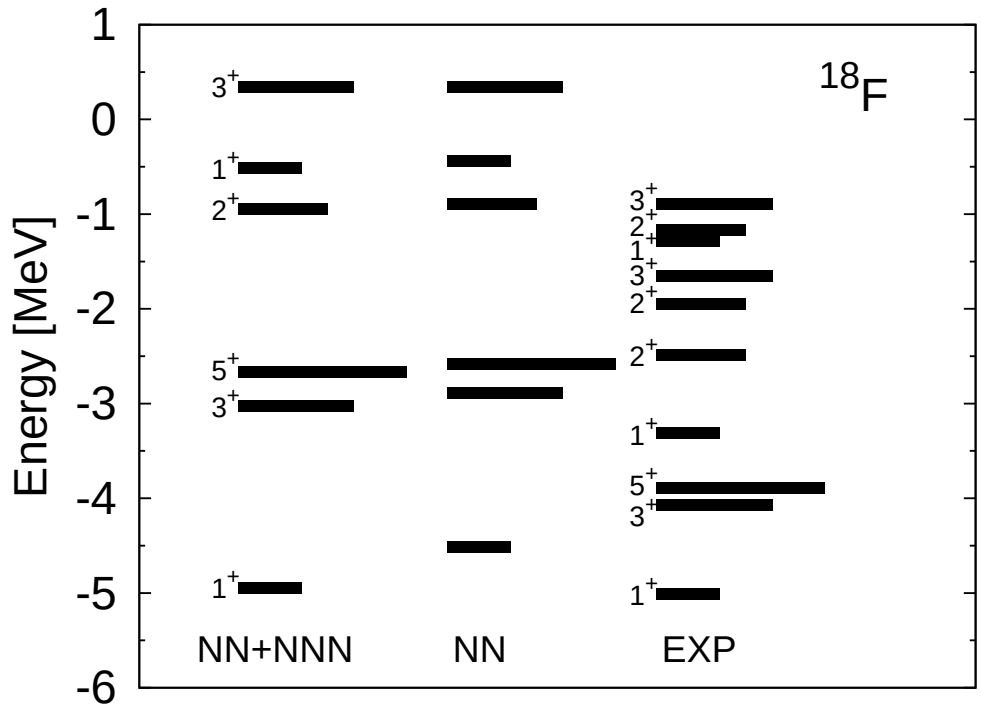

Figure 5.11: Same as Figure 5.10 except for ^{18}F.

calculating non-degenerate shell model effective interactions.

Our results for the *sdfp* calculations for ^{18}O are presented in Figure 5.12. The effective interaction used here is calculated in the same way as those used in the 'NN+NNN' columns of Figures 5.10 and 5.11 except for the few differences related to the use of the larger model space. With the *sdpf* space, the second-order $\hat{Q}$-box diagrams d5 of Figure 5.1 and similar ones with the V_{3N}^{med} vertices are no longer needed as their intermediate states are already within the model space. For the *sd* one-shell case, we have employed the experimental s.p. energies for the three *sd*-shell orbits. For the *sdpf* situation, we need in addition the experimental s.p. energies for the four *fp* orbits. Their values are, however, not well known. In the present calculation we have placed them all at one $\hbar\omega$ (14 MeV) above the $d_{5/2}$ level. (In the preceding *sd* calculation the same separation is used between the unperturbed *pf* and *sd* orbits.) As shown in Figure 5.12, we compare our 'One Shell' (*sd*) and 'Two Shells' (*sdpf*) results; it is of interest that they agree with each other rather

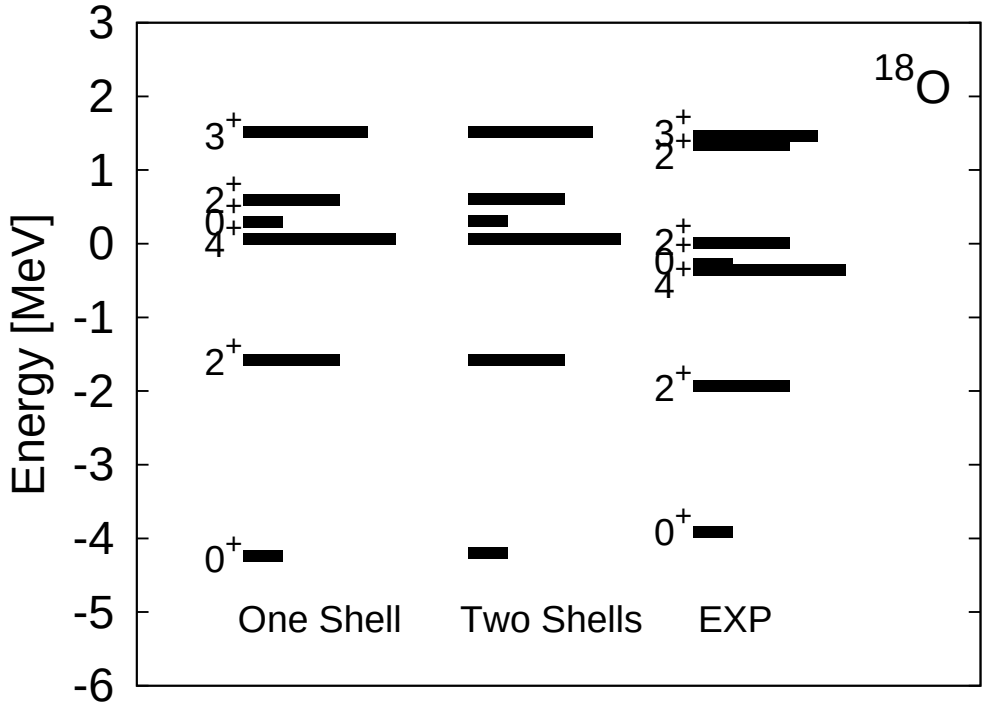

Figure 5.12: Comparison of the ^{18}O spectra calculated from the *sd* one-shell and *sdfp* two-shell effective interactions. Both with V_{3N}.

well. Similarly good agreement has also been observed for the corresponding ^{18}F calculations. We have found that this good agreement is largely due to the core polarization effects included in the $\hat{Q}$-box. The above comparisons provide in fact a test of our calculations. The renormalized *sd* and *sdpf* effective interactions are different, but in principle some of the eigenvalues given by the *sdpf* interactions should also be the eigenvalues given by the *sd* interactions. We have found in our calculations that the energies for the states with maximum *sd* overlaps given by the *sdpf* effective interactions are all in close agreement with the corresponding ones given by the *sd* effective interactions. Our *sdpf* effective interactions have been calculated using both the KK and EKKO methods, obtaining practically identical results. In short, we believe that these two methods are both well suited for calculating the shell-model effective interactions for non-degenerate model spaces. In this chapter we have only made an initial application, in calculating the low-lying states of

^{18}O and ^{18}F. Further applications of these methods should be of interest.

5.4 Conclusion and Outlooks

The iteration method of Krenciglowa and Kuo (KK) and that recently developed by Okamoto *et al.* (EKKO) are applied to the microscopic derivations of the *sd* and *sdpf* shell-model effective interactions using the chiral two-body (V_{2N}) and three-body (V_{3N}) potentials. We first study these two methods using a solvable model, and find that they are both suitable and efficient for deriving the effective interactions for non-degenerate model spaces, including the situation where the P-space and Q-space unperturbed Hamiltonians have spectrum overlaps. The Lee-Suzuki (LS) iteration method, which has been widely used for deriving degenerate shell-model effective interaction, is not as convenient as the KK and EKKO methods for the non-degenerate situation. The EKKO method has a special advantage that its vertex function $\hat{Z}$-box is, by construction, a continuous function while the $\hat{Q}$-box function used in LS and KK may have singularities. This is helpful to the convergence of the EKKO iteration method.

Using V_{2N} alone, we first calculate the degenerate *sd*-shell effective interactions using all LS, KK and EKKO methods. The results given by KK and EKKO are identical. It is noteworthy that the LS results, calculated with a low-order (5th order) iteration, are in very good agreement with the KK and EKKO ones, supporting the accuracy of the low-order LS method for calculating the degenerate shell-model effective interactions. We have calculated the non-degenerate *sdpf* effective interactions using V_{2N} with and without the inclusion of V_{3N} using both KK and EKKO methods. We believe that these methods are both suitable for microscopic calculations of non-degenerate effective interactions. Our results for the *sdpf* effective interactions given by the KK and EKKO methods are practically equivalent to each other. The low-lying states of ^{18}O and ^{18}F given by the *sdpf* effective interactions are nearly the same as those by the *sd* ones.

In our calculations we have employed the three-body force V_{3N}^{med} which is obtained from V_{3N} by integrating one of its participating nucleons over the

Fermi sea, as indicated by the 'hole-line' loops in Figures 5.2 and 5.4. We have carried out calculations for symmetric nuclear matter with the inclusion of this interaction and determine its low-energy constants c_D and c_E by requiring them to give satisfactory nuclear matter saturation properties. V_{3N}^{med} is explicitly dependent of the density n of the nuclear medium, and there is uncertainty in determining its value appropriate for the effective interactions among valence nucleons. In this chapter we have estimated this value by comparing the density profile of ^{16}O with the radial distribution of valence nucleons. This is an approximation which should be further investigated and improved upon. We have carried out calculations for ^{18}O and ^{18}F using V_{2N} with and without the above V_{3N}^{med}, the main effect of the latter being a small downward shift for the ground states of these nuclei while leaving the other states essentially unchanged.

Chapter 6

Summary

The nuclear matter equation of state (EoS) plays an important role in both nuclear physics and astrophysics, and its determination has been extensively pursued, both theoretically and experimentally. In this dissertation, we have derived a nuclear matter EoS microscopically and applied it to different fields, such as the neutron stars and nuclear symmetry energy.

We have demonstrated how the medium-modified nucleon-nucleon (NN) interaction inspired by the Brown-Rho scaling can give satisfactory results to both empirical saturation binding energy ($E_0/A = -16$MeV) and density ($n_0 = 0.16\text{fm}^{-3}$). In addition, the resulting EoS is consistent with the constraints deduced from heavy-ion collision experiments up to $4 \sim 5n_0$. This EoS is employed in the calculations of neutron stars and we have found that the effects from the BR scaling are important in reproducing their empirical properties. Calculated with (without) the BR scaling, the maximum mass of neutron stars, their radius and their moment of inertia are respectively $1.8(1.2)\text{M}_\odot$, 9(7)km and $60(24)\text{M}_\odot\text{km}^2$. Meanwhile, we have found that the effects from the BR scaling can be simulated by the well-known empirical Skyrme three-body forces.

We have studied the cold neutron matter at the unitary limit where the ${}^1S_0$ scattering length is infinite. Such strong interacting systems are believed to have a universal EoS, namely $E_0 = \xi E_0^{free}$ (E_0 and E_0^{free} are respectively the ground-state energy of interacting and non-interacting system). To study this

universal property, we have calculated ξ with a family of hard-core square-well unitarity potentials, all with infinite scattering lengths. Our results confirm the expected universality property and our derived value of $\xi \approx 0.44$ is in excellent agreement with the results given by accurate quantum Monte Carlo calculations.

The density dependence of the nuclear symmetry energy E_{sym} is studied with the Brown-Rho (BR) and Brown-Rho-Ericson (BRE) scalings. These two scalings can both reproduce the nuclear matter saturation properties well, and they give nearly identical EoSs for low densities ($n \leq n_0$). However, at higher densities, the EoS given by the linear BR scaling is too stiff and the resulting E_{sym} deviates largely from its empirical values deduced from heavy-ion collision experiments. In contrast the results obtained with the BRE scaling are satisfactory and in good agreement the empirical values.

The shell-model effective NN interactions are studied with the Krenciglowa-Kuo (KK) and the extended Krenciglowa-Kuo (EKKO) methods. Both methods have been employed to calculate the shell-model effective interactions for the degenerate *sd* and non-degenerate *sdpf* model spaces. A special feature of the EKKO iteration method is that its vertex function $\hat{Z}$-box is by construction a well behaved function of its energy variable (it is without singularity), while the $\hat{Q}$-box vertex function used in the KK iteration method may become singular for certain model-space partitions. Our calculations have indicated that the above feature of the EKKO method is particularly desirable for calculating the shell-model effective interactions for non-degenerate model spaces. We have also studied the effects of three-body forces in shell-model calculations. Our preliminary calculations have indicated that the effects of three-body forces are not important for the A = 18 valence nuclei, the spectra given by two-body and three-body forces being nearly the same as those by two-body forces alone.

Bibliography

[1] M. Prakash, *et al.*, "Physics of Neutron Star Interiors", D. Blaschke, N. K. Glendenning, A. Sedrakian (Eds.), Lecture Notes in Physics, Vol.**578**, Springer-Verlag p. 364, (2001).

[2] A. Sedrakian, Prog. Part. Nucl. Phys. **58**, 168 (2007).

[3] F. Weber, *Pulsars as astrophysical laboratories for nuclear and particle physics*, Bristol, U.K., Institute of Physics (1999).

[4] S. L. Shapiro and S. A. Teukolsky, *White dwarfs, black holes and neutron stars: The physics of compact objects*, Wiley (1983).

[5] J. M. Lattimer and M. Prakash, Phys. Rep. **442**, 109 (2007).

[6] P. Danielewicz, R. Lacey and W. A. Lynch, Science **298**, 1592 (2002).

[7] Bao-An Li, Lie-Wen Chen, Che Ming Ko, Phys. Rep. **464**, 113 (2008).

[8] B. A. Li and L. W. Chen, Phys. Rev. **C72**, 064611 (2005).

[9] M. B. Tsang, *et al.*, Phys. Rev. Lett. **102**, 122701 (2009).

[10] R. Machleidt, Phys. Rev. **C63**, 024001 (2001).

[11] V. G. J. Stoks, R. A. M. Klomp, C. P. F. Terheggen and J. J. de Swart, Phys. Rev. **C49**, 2950 (1994).

[12] R. B. Wiringa, V. G. J. Stoks and R. Schiavilla, Phys. Rev. **C51**, 38 (1995).

[13] R. Machleidt, Adv. Nucl. Phys. **19**, 189 (1989).

[14] J. J. Aubert *et al.*, Phys. Lett. **B123**, 275 (1983).

[15] S. Strauch *et al.*, Phys. Rev. Lett. **91**, 052301 (2003).

[16] H. Stocker and W. Greiner, Phys. Rep. **137**, 277 (1986).

[17] W. Cassing, V. Metag, U. Mosel and K. Niita, Phys. Rep. **188**, 363 (1990).

[18] Y. Nambu and G. Jona-Lasinio, Phys. Rev. **122**, 345-358 (1961).

[19] M. Lutz, S. Klimt and W. Weise, Nucl. Phys. **A 542**, 521 (1992).

[20] G. E. Brown, M. Rho, Phys. Rev. Lett. **66**, 2720 (1991).

[21] H. Primakoff and T. Holstein, Phys. Rev. **55**, 1218 (1939).

[22] J. Fujita and H. Miyazawa, Prog. Theor. Phys. **17**, 360 (1957).

[23] P. Navratil, V. G. Gueorguiev, J. P. Vary, W. E. Ormand and A. Nogga, Phys. Rev. Lett. **99**, 042501 (2007).

[24] B. S. Pudliner, V. R. Pandharipande, J. Carlson and R. B. Wiringa, Phys. Rev. Lett. **74**, 047304 (2006).

[25] M. Baldo and L. S. Ferreira, Phys. Rev. **C59**, 682 (1999).

[26] S. A. Coon *et al.*, Nucl. Phys. **A317**, 242 (1979).

[27] P. Grange, A. Lejeune, M. Martzolff and J.-F. Mathiot, Phys. Rev. **C40**, 1040 (1989).

[28] P. Navratil and W. E. Ormand, Phys. Rev. Lett. **88**, 152502 (2002).

[29] K. Hebeler, S. K. Bogner, R. J. Furnstahl, A. Nogga and A. Schwenk, Phys. Rev. **C83**, 031301(R) (2011).

[30] E. Epelbaum, A. Nogga, W. Glockle, H. Kamada, Ulf-G. Meißner and H. Witala, Phys. Rev. **C66**, 064001 (2002).

[31] H. A. Bethe, Annu. Rev. Nucl. Sci. **21**, 93 (1971).

[32] H. Q. Song, M. Baldo, G. Giansiracusa and U. Lombardo, Phys. Lett. **B411**, 237 (1997).

[33] H. Q. Song, M. Baldo, G. Giansiracusa and U. Lombardo, Phys. Rev. Lett. **81**, 1584 (1998).

[34] J. W. Holt and G. E. Brown, "Hans Bethe and the Nuclear Many-Body Problem" in *Hans Bethe and His Physics* (World Scientific, 2006, edited by G.E. Brown and C.-H. Lee).

[35] R. Brockmann and R. Machleidt, Phys. Rev. **C42**, 1965 (1990).

[36] S. K. Bogner, T. T. S. Kuo and A. Schwenk, Phys. Rep. **386**, 1 (2003).

[37] S. K. Bogner, T. T. S. Kuo and L. Coraggio, Nucl. Phys. **A684**, 432 (2001).

[38] S. K. Bogner, T. T. S. Kuo, L. Coraggio A. Covello and N. Itaco, Phys. Rev. **C65**, 051301(R) (2002).

[39] S. K. Bogner, T. T. S. Kuo, A. Schwenk, D. R. Entem and R. Machleidt, Phys. Lett. **B576**, 265 (2003).

[40] J. D. Holt, T. T. S. Kuo and G. E. Brown, Phys. Rev. **C69**, 034329 (2004).

[41] L. Coraggio, A. Covello, A. Gargano, N. Itako, T. T. S. Kuo, D. R. Entem and R. Machleidt, Phys. Rev. **C66**, 021303(R) (2002).

[42] A. Schwenk, G. E. Brown and B. Friman, Nucl. Phys. **A703**, 745 (2002).

[43] L. W. Siu, T. T. S. Kuo and R. Machleidt, Phys. Rev. **C77**, 034001 (2008).

[44] L. W. Siu, J. W. Holt, T.T.S. Kuo and G.E. Brown, Phys. Rev. **C79**, 054004 (2009).

[45] H. Q. Song, S. D. Yang and T.T.S. Kuo, Nucl. Phys. **A462**, 491 (1987).

[46] D. J. Rowe, *Nuclear Collective Motion* (Methuen and Co. Ltd., London, 1970).

[47] T. T. S. Kuo and Y. Tzeng, Int. Jour. Mod. Phys. **E**, Vol. 3, No. 2. 523 (1994).

[48] P. B. Demorest, T. Pennucci, S. M. Ransom, M. S. E. Roberts and J. W. T. Hessels, Nature **467**, 1081-1083 (2010).

[49] C. J. Pethick and H. Smith, Bose-Einstein Condensation in Dilute Gases, Cambridge, 2002.

[50] C. A. Regal and D. S. Jin, Phys. Rev. Lett. **90**, 230404 (2003); S. Jochim, M. Bartenstein, G. Hendl, J.H. Denschlag, R. Grimm, A. Mosk and M. Weidemüller, *ibid.* **89**, 273202 (2002); C. H. Schunck, M. W. Zwierlein, C. A. Stan, S. M. F. Raupach, W. Ketterle, A. Simoni, E. Tiesinga, C. J. Williams and P. S. Julienne, Phys. Rev. **A71**, 045601 (2005).

[51] G. B. Patridge, Wenhui Li, R. I. Kamar, Yean-an Liao, R. G. Hulet, Science **311**, 503 (2006).

[52] J. T. Stewart, J. P. Gaebler, C. A. Regal and D. S. Jin, Phys. Rev. Lett **97**, 220406 (2006).

[53] Le Luo, J.E. Thomas, J. Low. Temp. Phys. 154: 1-29 (2009).

[54] J. Carlson, S.-Y. Chang, V. R. Pandharipande and K. E. Schmidt, Phys. Rev. Lett, **91**, 050401 (2003).

[55] G. E. Astrakharchik, J. Boronat, J. Casulleras and S. Giorgini, Phys. Rev. Lett. **93**, 200404 (2004).

[56] A. Gezerlis and J. Carlson, Phys. Rev. **C77**, 032801(R) (2008).

[57] R. Okamoto, K. Suzuki, H. Kumagai and S. Fujii, to be published in 'Proceedings of the 10th International Spring Seminar on Nuclear Physics (May 21-25, Sur Mare Vietri, Italy, ed. by A. Covello)'; arXiv:1011.1994v1.

[58] H. Dong, T. T. S. Kuo and R. Machleidt, Phys. Rev. **C80**, 065803 (2009).

[59] H. Dong, L.-W. Siu, T. T. S. Kuo and R. Machleidt, Phys. Rev. **C81**, 034003 (2010).

[60] H. Dong, T. T. S. Kuo and R. Machleidt, Phys. Rev. **C83**, 054002 (2011).

[61] H. Heiselberg and M. Hjorth-Jensen, Phys. Rep. **328**, 237 (2000).

[62] F. Sammarruca and P. Liu, arXiv:0906.0320.

[63] R. R. Silbar and S. Reddy, Am. J. Phys. **72**(7), 892 (2004).

[64] G. E. Brown, M. Rho, Phys. Rep. **269**, 333 (1996).

[65] G. E. Brown, M. Rho, Phys. Rep. **363**, 85 (2002).

[66] G. E. Brown, M. Rho, Phys. Rep. **396**, 1 (2004).

[67] R. Rapp, R. Machleidt, J. W. Durso and G. E. Brown, Phys. Rev. Lett. **82**, 1827 (1999).

[68] D. Alonso and F. Sammarruca, Phys. Rev. **C68**, 054305 (2003).

[69] G. E. Brown, W. Weise, G. Baym and J. Speth, Comments Nucl. Part. Phys. **17**, 39 (1987).

[70] J. W. Holt, G. E. Brown, T. T. S. Kuo, J. D. Holt and R. Machleidt, Phys. Rev. Lett. **100**, 062501(2008).

[71] S. K. Bogner, A. Schwenk, R. J. Furnstahl and A. Nogga, Nucl. Phys. **A763**, 59 (2005).

[72] T. Hatsuda and S. H. Lee, Phys. Rev. **C46** R34 (1992).

[73] M. Harada and K. Yamawaki, Phys. Rep. **381**, 1 (2003).

[74] F. Klingl, N. Kaiser and W. Weise, Nucl. Phys. **A624**, 527 (1997).

[75] D. Trnka *et al.*, Phys. Rev. Lett. **94**, 192303 (2005).

[76] M. Naruki *et al.* Phys. Rev. Lett. **96**, 092301 (2006).

[77] P. Ring and P. Schuck, *The Nuclear Many-Body Problem* (Springer-Verlag, New York, 1980), and references quoted therein.

[78] B. Friedman and V. R. Pandaripande, Nucl. Phys. **A361**, 502 (1981).

[79] B. A. Brown, Phys. Rev. Lett. **85**, 5296 (2000).

[80] J. Cooperstein, Phys. Rev. **C37**, 786 (1988).

[81] J. M. Lattimer and B. F. Schutz, Astrophys. J. **629**, 979 (2005).

[82] A. Worley, P. G. Krastev and B.-A. Li, Astrophys. J. **685**, 390 (2008).

[83] M. Bejger, P. Haensel, Astrophys. J. **405**, 747 (2003).

[84] G. Baym, C. Pethick and P. Sutherland, Astrophy. J. **170**, 299 (1971).

[85] J. Xu, L.-W. Chen, B.-A. Li and H.-R. Ma, Phys. Rev. **C79**, 035802 (2009).

[86] A. W. Steiner, Phys. Rev. **C77**, 035805 (2008).

[87] S. B. Ruster, M. Hempel and J. Schaffner-Bielich, Phys. Rev. **C73**, 035804 (2006).

[88] J. Carriere, C. J. Horowitz and J. Piekarewicz, Astrophys. J. **593**, 463 (2003).

[89] A. Szmagliński, W. Wójcik, M. Kutschera, Acta Phys. Pol. **B37**, 1 (2006).

[90] R. F. Bishop, Int. J. Mod. Phys. **B15**, III (2001), "Many-Body Challenge Problem by G. F. Bertsch".

[91] K. M. O'Hara, S. L. Hemmer, M. E. Gehm, S. R. Granade, J. E. Thomas, Science **298**, 2179 (2002).

[92] M. E. Gehm, S. L. Hemmer, S. R. Granade, K. M. O'Hara, J. E. Thomas, Phys. Rev. **A68**, 011401(R) (2003).

[93] G. A. Baker, Jr., Phys. Rev. **C60**, 054311 (1999).

[94] H. Heiselberg, Phys. Rev. **A63**, 043606 (2001).

[95] J. Carlson, J. Morales, Jr., V. R. Pandharipande and D. G. Ravenhall, Phys. Rev. **C68**, 025802 (2003).

[96] S. Y. Chang and V. R. Pandharipande, J. Carlson, K. E. Schmidt, Phys. Rev. **A70**, 043602 (2004).

[97] A. Perali, P. Pieri and G. C. Strinati, Phys. Rev. Lett. **93**, 100404 (2004).

[98] J. Carlson and S. Reddy, Phys. Rev. Lett. **95**, 060401 (2005).

[99] A. Bulgac and G. F. Bertsch, Phys. Rev. Lett. **94**, 070401 (2005).

[100] A. Schwenk and C. J. Pethick, Phys. Rev. Lett. **95**, 160401 (2005).

[101] Y. Nishida and D. T. Son, Phys. Rev. Lett. **97**, 050403 (2006).

[102] D. Lee and T. Schäfer, Phys. Rev. **C73**, 015202 (2006).

[103] R. Haussmann, W. Rantner, S. Cerrito and W. Zwerger, Phys. Rev. **A75**, 023610 (2007).

[104] J.-W. Chen and E. Nakano, Phys. Rev. **A75**, 043620 (2007).

[105] B. Borasoy, E. Epelbaum, H. Krebs, D. Lee and U.-G. Meißner, Eur. Phys. J. **A35**, 357 (2008).

[106] S. Giorgini, L. P. Pitaevskii and S. Stringari, Rev. Mod. Phys. **80**, 1215 (2008).

[107] E. Epelbaum, H. Krebs, D. Lee and U.-G. Meißner, Eur. Phys. J. **A40**, 199 (2009).

[108] T. Abe and R. Seki, Phys. Rev. **C79**, 054003 (2009).

[109] T. Schaefer and D. Teany, Rep. Prog. Phys. **72**, 126001 (2009).

[110] E. Epelbaum, W. Gloeckle, A. Krueger and U. Meißner, Nucl. Phys. **A465**, 413 (1999).

[111] J. D. Holt, T. T. S. Kuo, G. E. Brown and S. K. Bogner, Nucl. Phys. **A733**, 152 (2004).

[112] A. Fetter and J. D. Walecka, 'Quantum Theory of Many-Particle Systems' (MacGraw Hill Book Co. 1971).

[113] R. K. Su, S. D. Yang and T. T. S. Kuo, Phys. Rev. **C35**, 1539 (1987).

[114] V. Baran *et al.*, Phys. Rep. **410**, 335 (2005).

[115] A. W. Steiner, M. Prakash, J. Lattimer and P. J. Ellis, Phys. Rep. **411**, 325 (2005).

[116] M. Di Toro *et al.*, Prog. Part. Nucl. Phys. **62**, 383 (2008).

[117] F. Sammarruca, Int. J. Mod. Phys. **E19**, 1259 (2010); arXiv:1002.0146.

[118] Xiao *et al.*, Phy. Rev. Lett. **102**, 062502 (2009).

[119] I. Bombaci and U. Lombardo, Phys. Rev. **C44**, 1892 (1991).

[120] W. Zuo, A. Leguene, U. Lombardo and J. F. Mathiot, Eur. Phys. J. **A14**, 469 (2002).

[121] Z. H. Li *et al.*, Phys. Rev. **C74**, 047304 (2006).

[122] D. Alonso and F. Sammarruca, Phys. Rev. **C67**, 054301 (2003).

[123] P. Krastev and F. Sammarruca, Phys. Rev. **C74**, 025808 (2006).

[124] E. N. E. van Dalen, C. Fuchs and A. Faessler, Eur. Phys. J. **A31**, 29 (2007).

[125] R. B. Wiringa *et al.*, Phys. Rev. **C38**, 1010 (1988).

[126] L. W. Chen *et al.*, Phys. Rev. **C76**, 054316 (2007).

[127] L. W. Chen, C. M. Ko and B. A. Li, Phys. Rev. Lett. **94**, 032701 (2005).

[128] T. T. S. Kuo, Z. Y. Ma and R. Vinh Mau, Phys. Rev. **33**, 717 (1986).

[129] M. Ericson, Phys. Lett. **B301**,11 (1993).

[130] T. D. Cohen, R. J. Furnstahl, D. K. Griegel, Phys. Rev. **C45**,1881 (1992).

[131] J. Gasser, H. Leutwyler and M. E. Sainio, Phys. Lett. **B253**,252 (1991).

[132] J. W. Holt, G. E. Brown, Jason D. Holt and T. T. S. Kuo, Nucl. Phys. **A785**, 322 (2007).

[133] T. T. S. Kuo and E. Osnes, *Lecture Notes in Physics* (Springer-Verlag, New York, 1990), Vol. 364.

[134] M. Hjorth-Jensen, T. T. S. Kuo and E. Osnes, Phys. Rep. **261**, 126 (1995), and references therein.

[135] L. Coraggio, A. Covello, A. Gargano, N. Itaco and T. T. S. Kuo, Prog. Part. Nucl. Phys. **62**, 135 (2009) and references quoted therein.

[136] B. A. Brown and B. H. Wildenthal, Ann. Rev. Nucl. Part. Sci. **38**, 29 (1988).

[137] B. A. Brown, W. A. Richter, Phys. Rev. **C74**, 0343150 (2006).

[138] T. T. S. Kuo, S. Y. Lee and K. F. Ratcliff, Nucl. Phys. **A176** 172 (1971).

[139] S. Y. Lee and K. Suzuki, Phys. lett. **B91**, 173 (1980).

[140] K. Suzuki and S. Y. Lee, Prog. Theor. Phys. **64**, 2091 (1980).

[141] K. Suzuki, R. Okamoto, P. J. Ellis and T. T. S. Kuo, Nucl. Phys. **A567**, 576 (1994).

[142] E. M. Krenciglowa and T. T. S. Kuo, Nucl. Phys. **A235**, 171 (1974).

[143] T. T. S. Kuo, F. Krmpotic, K. Suzuki and R. Okamoto, Nucl. Phys. **A582**, 205 (1995).

[144] A. Nogga, H. Kamada and W. Glockle, Phys. Rev. Lett. **94**, 944 (2000).

[145] S. C. Peiper, K. Varga and R. B. Waringa, Phys. Rev. **C66**, 044310 (2002).

[146] J. W. Holt, N. Kaiser and W. Weise, Phys. Rev. **C79**, 054331 (2009).

[147] T. Otsuka, T. Sizuki, J. D. Holt, A. Schwenk and Y. Akaishi, Phys. Rev. Lett. **105**, 032501 (2010).

[148] D. R. Entem, R. Machleidt and H. Witala, Phys. Rev. **C65**, 064005 (2002).

[149] J. W. Holt, N. Kaiser and W. Weise, Phys. Rev. **C81**, 024002 (2010).

[150] E. Epelbaum, Prog. Part. Nucl. Phys. **57**, 654 (2006).

[151] L. Coraggio and N. Itaco, Phys. Lett. **B616**, 43 (2005).

[152] M. C. M. Rentmeester, R. G. E. Timmermans and J. J. de Swart, Phys. Rev. **C67** 044001 (2003).

[153] http://www.nndc.bnl.gov/chart/.